

FMH606 Master's Thesis 2022

Process Technology

Development of a CPFD model-based technique to optimize feed pellets transfer systems in fish farms



John Ikechukwu Okoro

Faculty of Technology, Natural sciences and Maritime Sciences
Campus Porsgrunn

Course: FMH606 Master's Thesis, 2022

Title: Development of a CPFED model-based technique to optimize feed pellets transfer systems in fish farms

Number of pages: 91

Keywords: Pneumatic systems, CPFED, pressure drop, erosion, pipe bend, drag models, transport velocity, fish feed pellet, hydrodynamics, modeling, optimization.

Student: John Ikechukwu Okoro

Supervisor: Prof Chandana Ratnayake

External partner: Jana Chladek, Chameera Jayarathna

Summary:

Erosion impact and pellet breakage predictions due to high velocities during pneumatic transport is a cause of concern in the fish farming industry, as it poses a threat to the pipe integrity; leading to increased cost of maintenance due to pipe wear, and environmental pollution resulting from the deposits of microplastics and broken pellets on the seabed.

This study developed a CFPD model using the Barracuda VR[®] commercial software to optimize the pneumatic transport of 1cm fish feed pellets in an HDPE (High-density polyethylene) pipe using different conveying velocities. Different drag models were tested to establish a base model to observe the pressure drop prediction along the pipe. Using the Wen-Yu and Ergun drag model for the high-velocity tests and the Ergun drag model for the lower velocity tests gave results that are close to the experimental data with acceptable deviations. This model was also used to predict the erosion-prone zones along the pipe and the effect of pipe bends on the hydrodynamics of the transport process.

Results from this study show that an increase in conveying velocity has a direct impact on pipe wear and pellet breakage, simulation results predicted that the highest impact on the pipe wall was at the bend entry position where particles change flow direction, while conducted experiments showed an increase in pellet attrition (breakage). Pressure test and simulation results showed a consistent pressure drop along the conveying pipe accounting for the particle transport through the pipe. The model predicted the hydrodynamics of the gas-solid conveying system, and transport phenomena such as particle roping and vortex formation were observed around the bend region. With a pellet size change from 1cm to 0.5 cm, there was a 27.4% reduction in maximum erosion impact intensity on the pipe wall at a velocity of 32 m/s and a solid loading ratio of 3.24, similarly, increasing the pipe diameter from 7.4cm to 14.8cm for the 1cm pellet resulted in a 94.6% decrease in maximum erosion impact at the same velocity and solid loading ratio.

Acknowledgments

My appreciation goes especially to my supervisor prof. Chandana Ratnayake for the support and guidance offered to me in the course of carrying out this study. His meticulous explanations aided me in grasping the fundamentals of the topic within a short period of time.

I also want to appreciate my co-supervisor Jana Chladek for her consistent follow-up on my work and for teaching me to develop an inquisitive mind during this study. This will be very helpful to me as I further in life.

Many thanks to Chameera Jayarathna my co-supervisor for designing modules that got me through the basics of Barracuda. This gave me a quick knowledge of how to use the software within a short span of time. His suggestions and gentle push were very helpful during this study.

Thanks to Franz Otto von Hafenbradl for making the laboratory work fun and facilities in the pilot rig easy to operate.

I would like to thank Zahir Barahmand for his advice and quick response to my mails whenever I was stuck with my simulations.

To the management and administration of USN (Porsgrunn), I appreciate the privilege granted me to start and complete my master's program in an environment that made provisions for all facilities needed to achieve success.

Finally, thanks to my wife, Udeme James for the encouragement and emotional support she gave me during the course of my studies.

Porsgrunn, 18/05/2022

John

Abstract

Erosion impact and pellet breakage predictions due to high velocities during pneumatic transport is a cause of concern in the fish farming industry, as it poses a threat to the pipe integrity; leading to increased cost of maintenance due to pipe wear, and environmental pollution resulting from the deposits of microplastics and broken pellets on the seabed.

This study developed a CPFD model using the Barracuda VR[®] commercial software to optimize the pneumatic transport of 1cm fish feed pellets in an HDPE (High-density polyethylene) pipe at different conveying velocities. Different drag models were tested to establish a base model to observe the pressure drop prediction along the pipe. Using the Wen-Yu and Ergun drag model for the high-velocity tests and the Ergun drag model for the lower velocity tests gave results that are close to the experimental data with acceptable deviations. This model was also used to predict the erosion-prone zones along the pipe and the effect of pipe bends on the hydrodynamics of the transport process.

Results from this study show that an increase in conveying velocity has a direct impact on pipe wear and pellet breakage, simulation results predicted that the highest impact on the pipe wall was at the bend entry position where particles change flow direction, while conducted experiments showed an increase in pellet attrition (breakage) and the formation of oily deposits in the pipe walls at high transport velocities. Pressure test and simulation results showed a consistent pressure drop along the conveying pipe accounting for the particle transport through the pipe. The model predicted the hydrodynamics of the gas-solid conveying system, and transport phenomena such as particle roping and vortex formation were observed around the bend region.

With pellet size change from 1cm to 0.5 cm, there was a 27.4% reduction in maximum erosion impact intensity on the pipe walls around the bend when compared to the 1cm pellet at a velocity of 32 m/s and a solid loading ratio of 3.24, similarly, increasing the pipe diameter from 7.4cm to 14.8cm for the 1cm pellet resulted in a 94.6% decrease in maximum erosion impact at the same velocity and solid loading ratio.

Contents

1	Introduction	14
1.1	Background	14
1.2	Task description	17
1.3	Task objective	17
1.4	Report structure	18
2	Literature review	19
2.1	Conveying systems	19
2.1.1	<i>Mechanical conveying</i>	19
2.1.2	<i>Pneumatic conveying</i>	19
2.2	Pneumatic transport challenges	25
2.2.1	<i>Erosion</i>	26
2.2.2	<i>Attrition</i>	26
2.3	Modelling of pneumatic conveying systems	27
2.3.1	<i>CFD modelling</i>	27
2.3.2	<i>MP-PIC modelling – CPF</i> scheme	28
2.3.3	<i>Governing equations</i>	29
2.3.4	<i>Drag models</i>	30
2.3.5	<i>Erosion model</i>	34
2.4	Previous studies	35
3	Materials and methods	37
3.1	Experimental setup	37
3.2	Instrumentation	38
3.2.1	<i>Feeding tank</i>	38
3.2.2	<i>Receiving tank</i>	39
3.2.3	<i>Conveying pipes</i>	40
3.2.4	<i>Gas-solid separator</i>	41
3.2.5	<i>Pressure transducers</i>	41
3.2.6	<i>Control Panel</i>	42
3.2.7	<i>Data visualization and storage</i>	42
3.2.8	<i>The weighing scale</i>	43
3.2.9	<i>The thickness gauge</i>	44
3.3	Operations	44
3.3.1	<i>Pre-test operations</i>	45
3.3.2	<i>Post-test operations</i>	45
3.4	Test procedure	45
4	Simulation setup	47
4.1	Geometry	47
4.2	Model setup flow chart	48
4.2.1	<i>Grid setup and grid check</i>	48
4.2.2	<i>Global settings</i>	49
4.2.3	<i>Base material definition</i>	50
4.2.4	<i>Particle species and drag model</i>	51
4.2.5	<i>Initial conditions</i>	51
4.2.6	<i>Pressure and flow boundary conditions</i>	52
4.2.7	<i>Simulation time, data output, and post-processing</i>	53
4.3	Model parameters	53
4.4	Model validation using drag models	53

5 Results and discussions56

5.1 Experimental results.....56

5.2 Pressure drop analysis57

 5.2.1 Erosion test - experiment57

 5.2.2 Erosion test – simulation.58

 5.2.3 Pressure tests – High and low-velocity cases.59

5.3 Particle volume fraction61

5.4 Particle roping effect and fluid velocity distribution.....63

5.5 Wall erosion impact analysis.....65

5.6 Pipe weight analysis.....68

5.7 Pipe thickness analysis69

5.8 Optimization analysis72

 5.8.1 Effect of pellet size on maximum erosion intensity72

 5.8.2 Effect of geometry change on maximum erosion intensity.....73

6 Challenges75

7 Conclusion76

8 Further work.....77

8 Reference78

9 Appendices85

Nomenclature

Symbol	Description	SI units
A	Particle acceleration	m/s^2
C_d	Drag coefficient	—
D	Drag function	—
F_p	Drag force acting on a particle	kgm/s^2
ρ_b, ρ_f	Bulk density, fluid density	kg/m^3
g	Acceleration due to gravity	m/s^2
I_p	Impact magnitude	$kg^{1.5} (m/s)^{2.5} / m^2 / year$
m_p	Particle mass	kg
M	Molecular weight	kg/mol
θ_p	Particle volume fraction	—
θ_{cp}	Particle volume fraction at close pack	—
P, P_f	Absolute pressure, fluid pressure	N/m^2
Q	Mass flow rate of gas	kg/s
R	Universal gas constant	$J/K.mol$
r_p	Particle radius	m
Re	Reynolds number	—
t	Time	s
μ_f	Fluid viscosity	$N.s/m^2$

Nomenclature

u_f, u_p, v	Fluid velocity, particle velocity, mean gas velocity	m/s
$w(\theta_p)$	Weighting factor	—
ψ	Sphericity of particle	—

List of figures

Figure 1.1: Fish feed pellet	15
Figure 1.2 : Typical fish cage.	15
Figure 1.3: Central feeding system	16
Figure 1.4: Fish feed carrier ship.	16
Figure 1.5: Report structure.	18
Figure 2.1: Basic components of a pneumatic conveying system.	20
Figure 2.2: Schematic representation of the basic components of a pneumatic system.	20
Figure 2.3: Schematic diagram of a dilute phase conveying system	22
Figure 2.4: Schematic diagram of a dense phase conveying system	22
Figure 2.5: Positive pressure configuration for pneumatic transport.	23
Figure 2.6: Negative pressure setup for Pneumatic conveying.	24
Figure 2.7: Combined negative-positive pressure pneumatic systems.	24
Figure 2.8 : Typical conveying characteristic curve - horizontal flow.	25
Figure 2.9: CFPD simulation of erosion impact.	26
Figure 2.10: A schematic view of an experimental setup for monitoring pellet attrition in a small bend	27
Figure 2.11: Model approach for gas-solid multiphase flow modelling.	28
Figure 2.12: Geldart classification of particles for air at ambient conditions.	31
Figure 3.1: Project process flow diagram.	37
Figure 3.2: Pictorial view of the pilot test rig.	38
Figure 3.3: Picture of the pellet feeding tank.	39
Figure 3.4: View of the receiving tank.	39
Figure 3.5: Determination of the bend radius.	40
Figure 3.6: Pictorial display of the horizontal pipe layout in the pilot rig.	40
Figure 3.7: Gas-solid separator - A 28 filter cartridge system.	41
Figure 3.8: Pressure transducer along the pipeline	42
Figure 3.9: Pneumatic control panel.	42
Figure 3.10: LabVIEW signal monitoring mode	43
Figure 3.11: The measuring scale	43
Figure 3.12: A pictorial view of the pipe bend during measurement using the Ohaus scale.	44
Figure 3.13: Thickness gauge	44

Figure 3.14: Rotary feeder meter as captured in the pilot rig	45
Figure 4.1: Geometry Plan view	47
Figure 4.2: Simulation setup flow chart.....	48
Figure 4.3: Setting and checking the grid.	49
Figure 4.4: 3D side view of the gridded geometry (computational domain) along the x-axis (left) and pipe cross section (right).	49
Figure 4.5: Global conditions	50
Figure 4.6: Screenshot of base material definition	50
Figure 4.7: Defining pellet properties and drag model	51
Figure 4.8: Initial condition	52
Figure 4.9: A view of the boundary conditions while looking at the geometry from the side along the x-axis	52
Figure 4.10: Pictorial view of the transducer locations along the pipe.....	54
Figure 4.11 Pressure comparison using different drag models at pressure transducer 2 at 23m/s.....	55
Figure 5.1: Pressure plot at 32m/s (top left), volume flow rate at 32m/s (bottom left), pressure plot at 15.3m/s (top right) and volume flow at 15.3m/s (bottom right).	58
Figure 5.2: Pressure drop for high-velocity erosion tests.	59
Figure 5.3: Plan view of geometry showing pressure points 20 and 25.	59
Figure 5.4: Pressure drop for high-velocity pressure test using the WenYun-Ergun model. ...	60
Figure 5.5: Pressure drop for low-velocity pressure tests using the Ergun model.	60
Figure 5.6: Pressure variation at Transducer 2 for low-velocity tests using the Ergun model.	61
Figure 5.7: View of geometry from the top (A), cross-section at 1.2m from the inlet (B), and 0.2m (C).	62
Figure 5.8: View of geometry from the top (A), cross-section around the bend at 0.22m along the y axis (B), and 2.3m from the inlet (C), and). This cross-sectional view is looking into the pipe from the inlet with particles and air going into the page.....	62
Figure 5.9: View of geometry from the top (A), cross-section at 1.85m (B), and 2.1m (C) along the y-axis.	63
Figure 5.10: Particle roping effect due to bend at 23m/s.	64
Figure 5.11: View of fluid velocity distribution and vortices formation along bend entrance. Plan view of geometry (A), vortices formation at bend entrance (B) and zoomed view of vortices region at bend entrance (C)	64
Figure 5.12: Zoomed geometry showing erosion tracking points along the pipe bend (A) and Pipe geometry showing the region of interest (B).	65

Figure 5.13: Graphical representation of impact intensity along the bend at different velocities.	66
Figure 5.14: Isovolum view showing impact intensity on pipe wall along the bend at a velocity of 32m/s.....	66
Figure 5.15: Isovolum view showing impact intensity on pipe wall along the bend at a velocity of 14.7m/s.....	67
Figure 5.16: Wall erosion over time at the bend entrance at a velocity of 32m/s.	68
Figure 5.17: Difference in bend weight before and after the erosion tests.	69
Figure 5.18: Thickness measurement points along the pipe bend.	69
Figure 5.19: Pipe thickness comparison at the right locations along the bend.	70
Figure 5.20: Pipe thickness comparison at the left locations along the bend.	71
Figure 5.21: Pipe thickness comparison at the top locations along the bend.	71
Figure 5.22: Pipe thickness comparison at the bottom locations along the bend.	72
Figure 5.23: Internal view of the cleaned bend cross-section after erosion test.	72
Figure 5.24: Maximum erosion intensity at different pellet diameters at a velocity of 32m/s.	73
Figure 5.25: Schematic view of the modified geometry.	74
Figure 5.26: Maximum erosion intensity at different pipe diameters at a velocity of 32m/s. .	74

List of tables

Table 2.1: Angular weights for a ductile material property.....	35
Table 4.1: Model parameters.....	54
Table 5.1: Experimental results for the different tests done in the pilot rig.....	57
Table 5.2: Experimental results used for analysis.....	57
Table 5.3: Pipe thickness measurement before and after erosion test.....	71

1 Introduction

The act of seafood farming also referred to as aquaculture is no doubt the most looked into food alternative for humans. 71% of the earth's surface is water-dominated, showing the importance of aquaculture in human survival and sustenance, this is quite crucial for the world's increasing growth rate[1]. It is extremely vital to state that over the years, there has been a geometric increase in the exploration of this industry[2] but this has notwithstanding left quite a sad trail of environmental and economic consequences in its wake[3]. Many research and developments have been carried out which are geared toward the adoption of state-of-the-art technologies as means to not only mitigate these negative consequences but also increase seafood harvesting and yield. A typical example is an introduction of the Precision Fish Farming (PFF) concept centered on making provisions for fish farmers to better manage fish production processes through the adoption of control-engineering principles[4].

1.1 Background

Fish farming is the most prominent in the aquaculture industry occupying a significant 50% of world seafood consumption in the hierarchy of seafood supply and consumption[5], [6]. Norway is the second second-largest harvester and exporter of farmed fish in the world trailing only behind china[7]. Statistics and research show that Norway is the world's largest producer of salmon fish with over 55.3% production share. The reports[8] from the Norwegian Seafood Council show a volume of 3.1 million tons of seafood valued at NOK 120.8 billion in 2021. It is an approximate 50% volume increase over a decade with salmon fish contributing to 42% of the export volume at NOK 81.4 billion in 2021. However, the in-land and close-to-shore methods of fish farming pose some challenges such as space limitations and environmental pollution [9]. This has resulted in innovations geared at expanding the offshore open system of fish farming with a projected production capacity of over 100,000 metric ton (MT) of the salmon fish by 2030[7], [10]. The above statistics portray the significant economic contributions of fish farming to the revenue increase of the country, the more reason attention is keenly paid to this sector.

In fish farming, the fish needs to be fed some nutrients to enable healthy growth, these nutrients traditionally come in the form of granules or pellets as shown in figure 1.1. The pellets guarantee a stable and concentrated state of the fish nutrients but are frail, demanding meticulous handling during transport to the fish beds. Attention is given to the feeding system of the pellets as they are transported over long distances from the storage silos in the carrier ship to the fish cage. This can impact the pellet's physical properties, leading to wastage and subsequent sea pollution as a result of the sensitive feeding nature of the fish[11]. The basic offshore open system is represented by figures 1.2 (fish cage), 1.3 (the central feeding system), and 1.4 (fish feed carrier ship) for large-scale fish farming.



Figure 1.1: Fish feed pellet [12].



Figure 1.2 : Typical fish cage[13].



Figure 1.3: Central feeding system [13].



Figure 1.4: Fish feed carrier ship[14].

According to Lekang[15], a feeding system is in simple terms one that follows a sequential pattern of picking the pellets from the storage vessels, moving them through the pipes, and distributing the pellets to the fish in the cage. This can be an automatic or semi-automatic process comprising feed silos, energy units for power delivery, air blowers and generators, distribution systems, feed delivery pipes, and feeder control systems. The feed delivery pipe amongst other components listed is of special interest in this work. The delivery pipe connects the storage tanks to the fish cage. High-density polyethylene (HDPE) pipes have found great acceptance and use in the fish farming industry in recent years. They exhibit ductile and flexible behavior allowing for compatibility with diverse kinds of ocean currents. They also have good marine properties which include the ability to resist galvanic corrosion and seaweed accumulation. HDPE pipes are easy to maintain due to their ability to stay above water, a

resultant effect of their lower density which is approximately 95% the density of saltwater and 96% that of freshwater [2], [16].

1.2 Task description

As stated above, the pipes play a key role in the transport system and can be used to transfer the pellets to far distances. This is a pneumatic transport process that could result in blockage of the pipes, especially in areas where a change in the direction of the pellet flow may occur due to necessary bends. Fish farmers in a bid to prevent this issue have adopted the use of very high transport air velocities which have led to negative environmental and economic consequences. These challenges include the cost associated with frequent pipe maintenance and damage due to increased wear on pipes, microplastic emissions into the sea, pellet breakage, local pollution, and loss of valuable yet expensive feed with high energy consumption in the process. In recent years, solutions to some of these challenges have been provided through physical experiments carried out on different pilot platforms but this comes at a heavy cost. It is therefore important to develop models capable of simulating the fish feed transport system effectively and subsequently adopt these models to optimize the overall system thereby saving cost and increasing process efficiency. This has necessitated the below objectives around which the study is focused.

1.3 Task objective

The objective of this work is to develop a computational particle-fluid dynamic (CPFD) model using Barracuda VR[®] 21.0.1, to simulate the pneumatic transport of fish feed pellets through a high-density polyethylene (HDPE) pipe. This model will be used to determine pressure drop along the pipe at different velocities and erosion impact on the pipe wall, especially at the bend region. The hydrodynamics of the flow under different conveying conditions will be investigated using the model. The CPFD model will be validated against experimental data collated from a pilot-rig test by using the results from simulations. It is important to note that models can be used to optimize the fish feed pellet conveying system. Pipe modifications can be done by changing the diameter and bend radius to investigate and reduce the effect of erosion impact on the walls. Pellet size can be varied using models to monitor the effect of pellet breakage (attrition). Changes in flow conditions can first be simulated before they are applied in the real systems, the same also applies to changes in the dimensions of operational units associated with any pellet conveying system. Furthermore, all of these can be achieved at a minimum cost rather than in a full-scale laboratory which will require a lot of resources and time. The advantages of simulation models in conveying systems especially as it relates to fish farming cannot be overemphasized. This study was carried out in parallel with the MICRORED project, titled “Reduction of Microplastic Emission through System Optimization of Feed Pellet Conveying Pipelines” funded by the Norwegian Seafood Research Fund (FHF) and coordinated by SINTEF Tel-Tek. A link to the detailed description of the project 901658 background, objectives, and implementation has been provided in the reference section.

1.4 Report structure

Figure 1.5 displays the report structure adopted in the course of this work. Chapter 1 briefly introduces the aquaculture industry, its importance, and economic impact with a focus on large-scale open sea fish farming. This was followed by the task description and objectives around which the study was carried out. A description of pneumatic transport systems, challenges, and principles was discussed in chapter 2, and a brief background on CPFV modeling was also captured with a review of previous works. Chapter 3 detailed the materials and methods adopted while chapter 4 focused on the CPFV model development and description. Experimental and simulation results were presented and discussed in chapter 5 while optimization analysis was made in section 5.8. Challenges were discussed in chapter 6 with conclusions on the study drawn in chapter 7. Chapter 8 focused on recommendations for further work and this brought the report to an end.

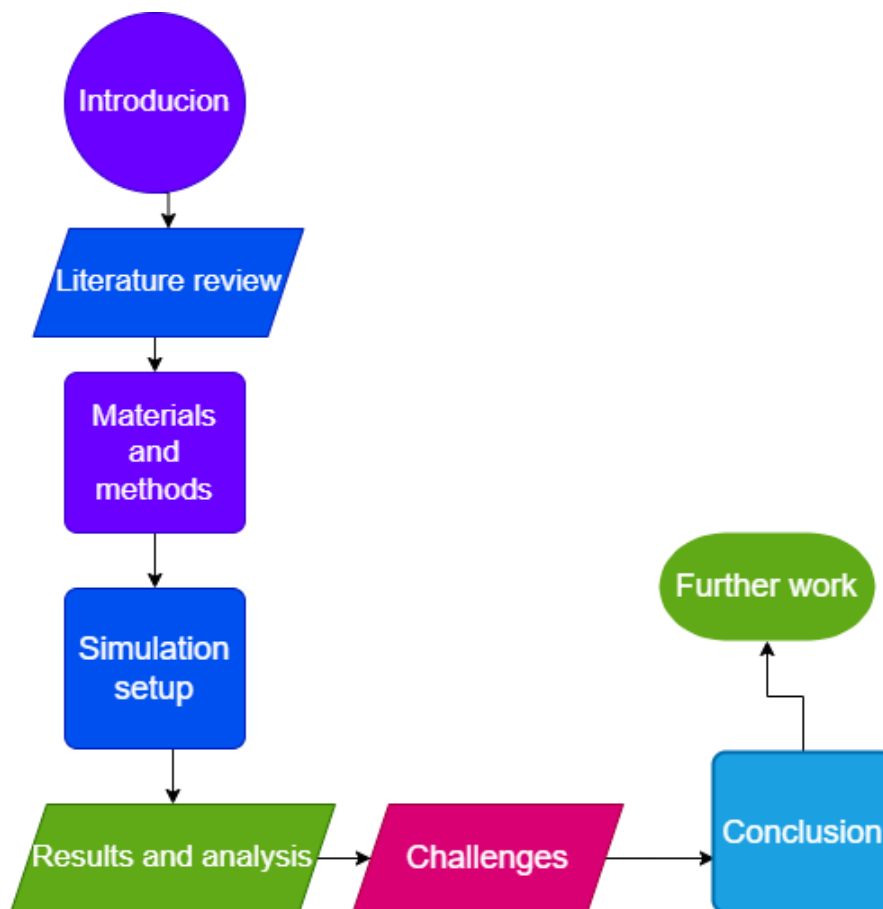


Figure 1.5: Report structure.

2 Literature review

This chapter reviewed the conveying systems with a focus on pneumatic conveying, the principles, types, and challenges of the pneumatic transport systems. The CFD modeling schemes were also reviewed with emphasis on the MP-PIC approach using the CPFD scheme. Governing equations of the scheme and drag models were discussed and finally, a review of some previous works was carried out.

2.1 Conveying systems

A conveyor system is a setup consisting of vertical, horizontal or inclined devices with the capacity to transport bulk materials, varying objects and packages between different machines and locations. The path taken by a conveyor is peculiar to its predefined design with established loading and discharge points which could be fixed or varied depending on the nature of its design and operating conditions[17]. Conveying systems could be mechanical, pneumatic, air-assisted, or hydraulic.

2.1.1 Mechanical conveying

This is probably the oldest form of bulk solid transport in the industry, in which mechanical devices such as bucket elevators, belts, vibratory, screw conveyors, etc., are used in the transport of solid materials. These systems pose fewer complications in their design and can be adopted for a wide range of bulk materials. Disadvantages include flexibility limitations and a high risk of material contamination [18].

2.1.2 Pneumatic conveying

For many years, powder-like materials in the form of granules have been moved from one specific location to another by many industrial plants through pneumatic transport operations [19]. This system which specializes in engaging safe and efficient means in the transport of dry bulk materials was estimated to have a global market value of \$28.4 billion United States dollars in 2021 with a projected increase to US\$40.5 billion by 2027[20]. It has been greatly sought out for and adopted by many industries owing to its cost-effectiveness, especially as it relates to low maintenance requirements and operations as well as low contamination of materials during transport. It also has flexibility advantages in terms of layout and installations with embedded automation possibilities when compared to other transport systems[21]. A fluid medium is used to transport the material through a pipe and then separated from it at the delivery point, pressure gradient and gas-solid momentum transfer is the major driving force in the pipe[22], [23]. During pneumatic conveying, different flow regimes occur and can be specified by factors such as the operating conditions adopted, product properties, and geometries, leading to pneumatic transport classification into the nature of system pressure used in operation or the conveying mode of the material [24].

2.1.2.1 Basic conveying components

A pictorial display of the basic components of a pneumatic conveying system is given in figure 2.1, with figure 2.2 showing how the filter is connected to the process. A brief description of the components is given below.

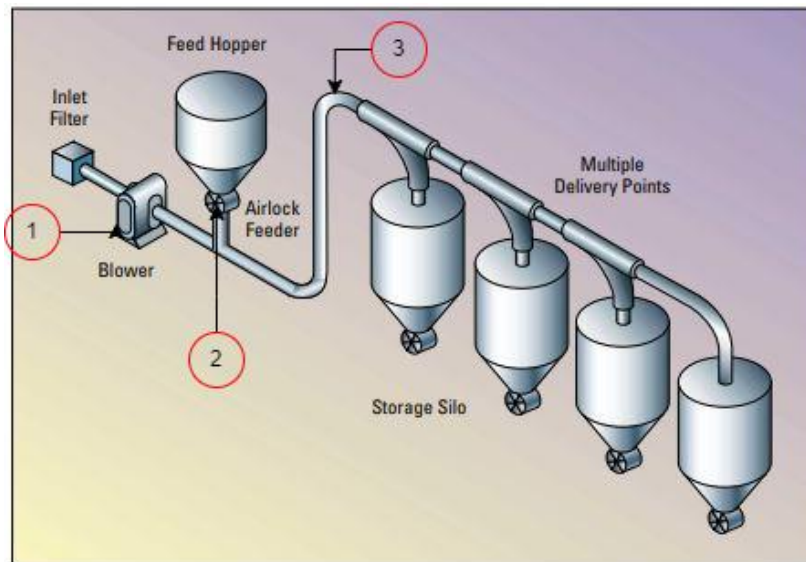


Figure 2.1: Basic components of a pneumatic conveying system[23].

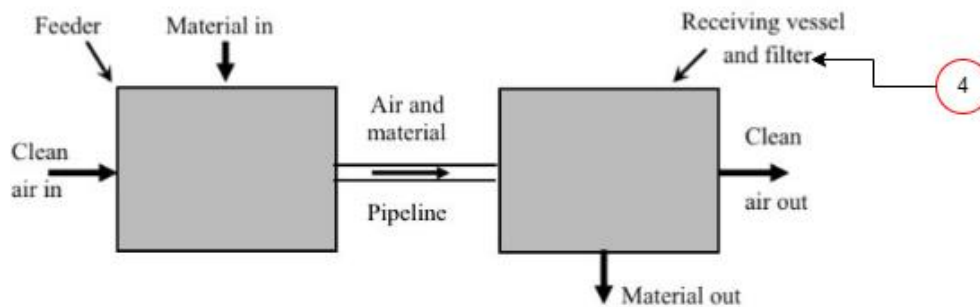


Figure 2.2: Schematic representation of the basic components of a pneumatic system[25].

1. Prime mover –

This is the energy supplier to the conveying gas by pressuring the gas through a compression system and releasing to the conveying line. Provides the driving force for the transport medium. It can be a compressor, blower, fan or vacuum pump.

2. Feeding device –

This can be in the form of a rotating valve, screw feeders, blow tanks etc. they are used to deliver the solid materials at a controlled rate into the compressed gas stream for transport through the line.

3. Pipeline -

This can be referred to as the conveying house of a pneumatic system, products are transported inside pipes of varying lengths consisting of straight sections which could

be horizontal, vertical or inclined as well as some curved sections which could come in varying shapes or form such as Tee-shape, V-shape, C-shape etc. Bends are critical during pipe layout in the industry and great attention should be paid during installation, especially with systems handling abrasive and degradable products[23].

4. Gas-solid separator –

Devices such as the cyclone, bag filters, electrostatic precipitators etc. are employed at the end of the transport line to separate the conveyed solids from the air stream.

2.1.2.2 Transport principle

The pneumatic conveying transport principle centers on gas expansion which results in a drop in density due to a decline in pressure. Density has inverse relations with volume flow rate while volume flow has direct proportionality with transport area and velocity, therefore it is no surprise that gas velocity increases with pressure drop along the pipeline during transport[26]–[28]. Equation 2.1 shows the relationship between gas density and pressure, equation 2.2 defines the mean gas velocity while equation 2.3 explains how pressure relates with the gas velocity.

$$\rho = \frac{MP}{RT} \quad (2.1)$$

$$v = \frac{Q}{\rho A} \quad (2.2)$$

$$v = \frac{QRT}{MPA} \quad (2.3)$$

Where;

v = Mean gas velocity m/s

Q = Mass flow rate kg/s

ρ = Density of gas kg/m³

P = Absolute pressure N/m²

R = Universal gas constant J/K.mol

M = Molecular weight kg/mol

2.1.2.3 Transport based on conveying mode

It was initially highlighted that material transport could be dependent on the conveying mode adopted. This depends on the material concentration conveyed vis-à-vis the conveying velocity. Two conveying modes are discussed below which include the dilute and dense phase.

1. Dilute system conveying;

Also referred to as the lean phase conveying, this mode is characterized by high velocities and low material concentration during transport. It ensures the complete suspension of bulk

materials in the transport medium and can be employed in the transport of all materials with adequate size distribution that fits the conveying pipe. It ensures good navigation ability around bends and curves along the delivery line[25]. Figure 2.3 displays a schematic representation of a dilute phase conveying system.

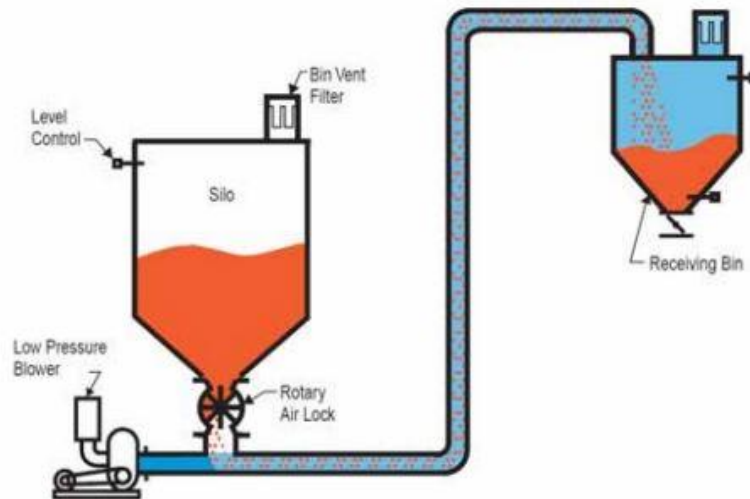


Figure 2.3: Schematic diagram of a dilute phase conveying system [29].

2. Dense phase conveying;

Figure 2.4 shows the schematic view of the dense phase conveying system. When conveying is done at velocities below the dilute phase, it can be regarded as dense transport. Characterized by high volume of material transport, dense phase transport is slow with high concentrated powder materials moving in intermittent successions of air pockets. Solid loading ratio (ratio between the mass flow rate of solids to that of the displaced gas) for dense phase systems are high and with values above 15[24], [30].

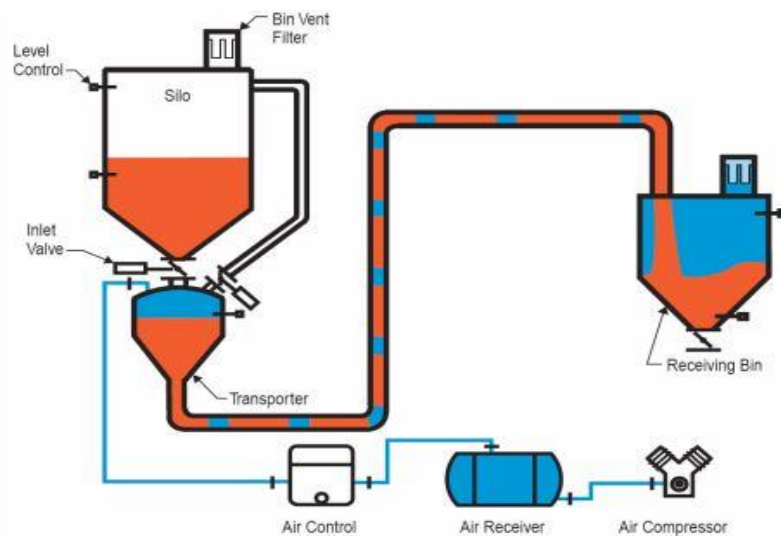


Figure 2.4: Schematic diagram of a dense phase conveying system [29].

2.1.2.4 Transport based on system pressure

1. Positive pressure systems –

Figure 2.5 depicts a pneumatic conveying configuration for positive pressure transport. In this case, the material is pushed through the line by the compressed air. The delivery point of such systems is usually at atmospheric pressure, indicating that absolute pressure through the line must be greater than that of the atmosphere. It is commonly adopted in many industrial setup as it has an advantage of possible delivery to multiple delivery locations[31].

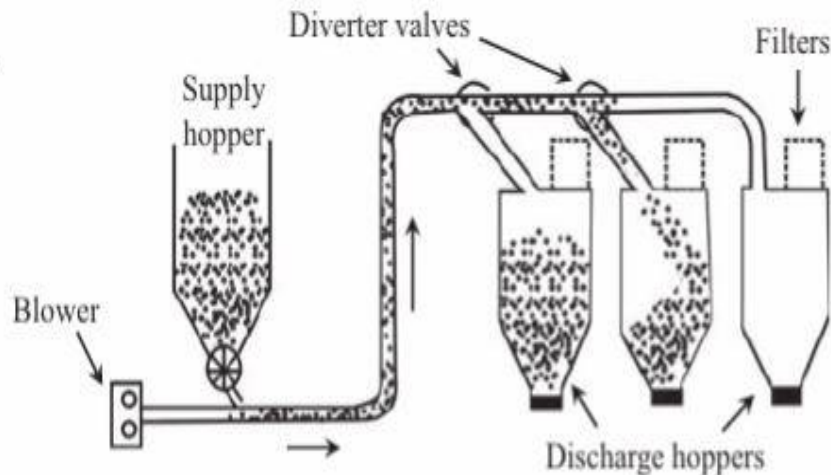


Figure 2.5: Positive pressure configuration for pneumatic transport[31]

2. Negative pressure systems-

A negative pressure gradient is established through an exhaust or vacuum system in the discharge point, causing the solids to be pulled through the pipe and into the discharge tanks. This is popularly referred to as the vacuum/suction system in which pressure within the transport line is less than the atmospheric pressure at the delivery station. It finds great prominence in the multiple pickup point and single delivery station systems[24], [31].Figure 2.6 displays a negative pressure configuration showing multiple pickup points.

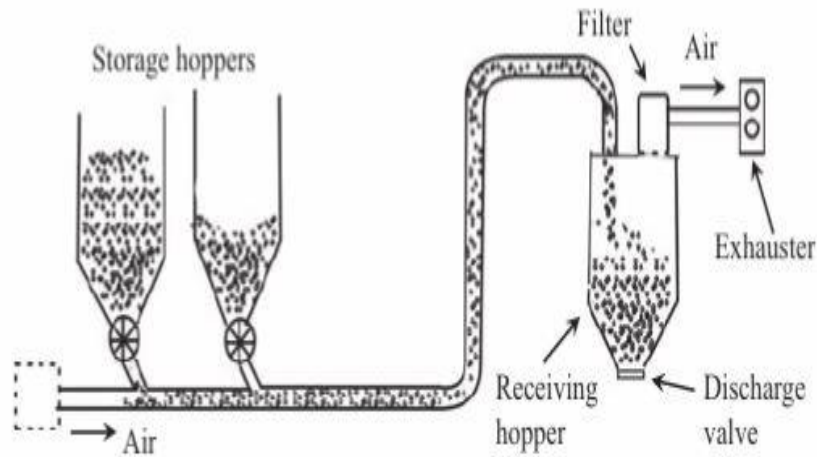


Figure 2.6: Negative pressure setup for Pneumatic conveying[31].

3. Combined negative-positive pressure system-

This system fondly called the suck-blow or push-pull system combines the inherent advantages of both the positive and negative pressure systems during pneumatic conveying. They find extreme usefulness in multiple pickup and multiple delivery of materials. An application as shown in figure 2.7, is a ship unloading system, where the negative pressure system is used to suck materials into an intermediate vessel while the positive pressure is used to push it into a reception silo onshore.

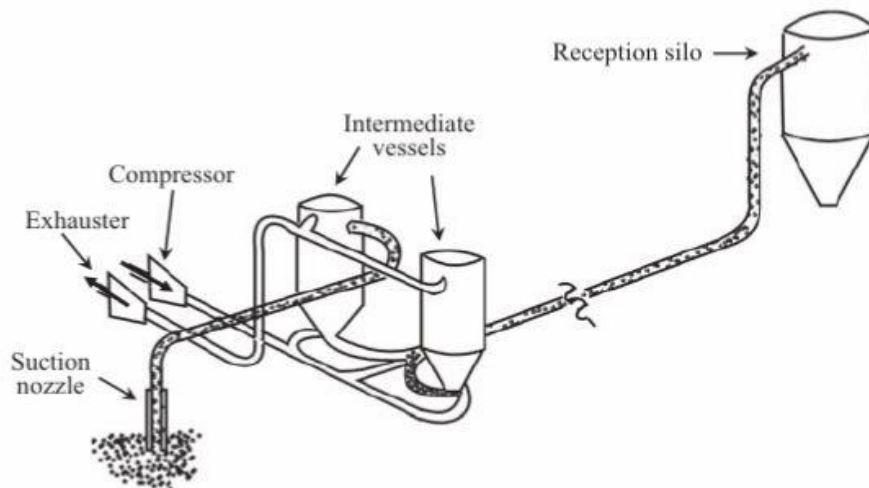


Figure 2.7: Combined negative-positive pressure pneumatic systems[31].

2.1.2.5 Phase diagram - horizontal conveying

When material transport is carried out in horizontal pipes just as is focused on in this report, there is a likelihood of varying flow patterns that could be observed. Flows such as slugs, unstable dunes, strand flows, and suspension flows can be observed as conveying fluid velocity is increased for a specified solid flow rate. The phase diagram for a horizontal system as shown in figure 2.8 informs on how much solids can be transported and is greatly dependent on three key factors which include the solid loading ratio, the superficial gas velocity and the pressure drop across the conveying line. The target for optimal transport is to convey along the region of minimum pressure drop. Since pressure loss also signifies energy loss, there is need to find the defining point at which solids can be transported at minimum velocity as well as pressure drop.

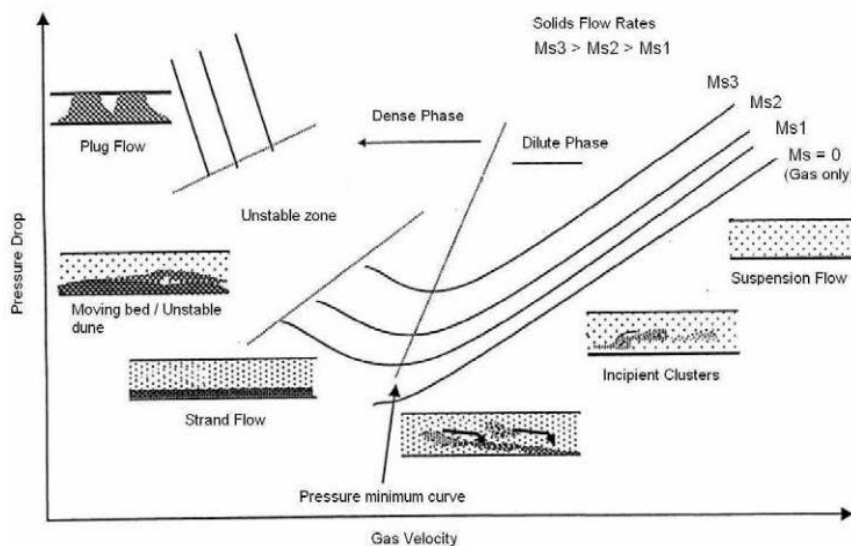


Figure 2.8 : Typical conveying characteristic curve - horizontal flow[24].

The left part of the conveying characteristic curve indicates region of low velocity applications during transport also referred to as the dense phase region with high solid loading ratio. As velocity is increased for a particle solid loading, pressure drops are observed (due to reduction in gas-solid fraction) and this will continue until gas saltation velocity (velocity at minimum pressure loss) is reached. Beyond this region, the dilute phase dominates with increased pressure losses due to frictional losses resulting from particle and fluid interaction with the walls of the conveying pipe [32], [33]. To avoid some conveying challenges and to minimize energy consumption during transport with increased efficiency, it is crucial to identify and adopt the appropriate conveying velocity during industrial operations.

2.2 Pneumatic transport challenges

The advantages attributed to the attractiveness of the pneumatic system has not left it without some critical challenges to look out for during operation. One of the key objectives of this report is to investigate the possible challenges encountered while operating pneumatic systems at high velocities and suggest possible solutions for mitigation and system optimization. The

most prominent industrial challenges faced while adopting this system include material degradation during flow, equipment wear which may come in the form of erosion or in high pressure areas, complete pipe blockage, particle roping and segregation[34]. High energy consumption during operation has also been observed while operating the pneumatic system under these challenging conditions. Two major challenges, especially as it relates to this report has been discussed in subsequent sections.

2.2.1 Erosion

The gradual eating or wearing away of the pipe surface along the pipe and especially in bends is called pipe erosion. Typically during gas-solid flows, the conveyed material makes contact with the surface of the pipe and depending on the nature of the material, different wear impacts can be observed in the pipe. For abrasive materials, which tend to constitute a large percentage of materials pneumatically conveyed, the erosion impact tends to be higher. It is also a known knowledge that bends associated with pipes tend to experience greater wear than other areas of the pipe as a result of the change in gas-solid flow direction which they create during transport. Key factors that are critical in pipe wear include, the material hardness, the angle of impact or impingement and the flow velocity. Research has proven that velocity has the greatest impact on pipe wear. High velocity adoption during pneumatic operations results in more wear impact. This is why dilute phase transport tend to have greater erosion impact. When transporting abrasive materials, it is always recommended to adopt a low velocity dense phase system[35]–[37]. Figure 2.9 is a CFPD simulation of a flow along a pipe bend, showing areas of high erosion impact.

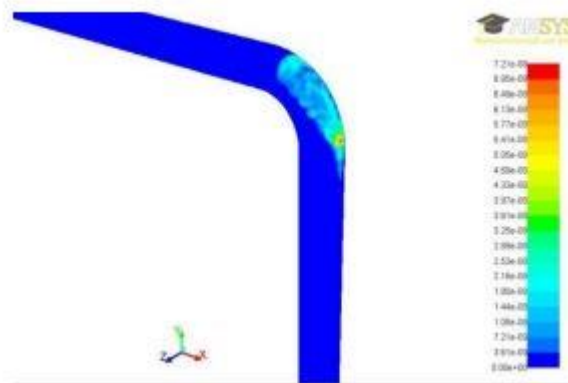


Figure 2.9: CFPD simulation of erosion impact[38].

2.2.2 Attrition

Particles are capable of experiencing two kinds of interactions during transport, they may rub against or collide with the pipe wall or with each other. These collisions are capable of engineering the crushing or breakage of these particles as a result of forces generated within them[39]. This phenomenon is common when conveying materials that are frail in nature, very predominant with high transport velocity like in dilute phase pneumatic transport[40], [41] and prevalent in areas where particles change flow direction like in bends and valves[42], [43].

Quite important to note is the fact that smaller radius bends results in higher particle breakage during transport as seen in figure 2.10. An associated challenge with attrition is the change in particle size and size distribution which results in finer particles usually undesirable in most cases. As discussed in chapter 1 where the fish becomes picky in pellet consumption due to size change, resulting in a huge loss of quite expensive pellet materials and local sea pollution[44]. Also, gas-solid filters could perform at low efficiencies if not designed to handle size changes occurring due to breakage[45]. Another disadvantage is that attrition can change flow characteristics as was experienced during the laboratory experiments in the pilot rig in which a free flowing bulk could become difficult to transport as particle breakage sets in[23], [46], [47].

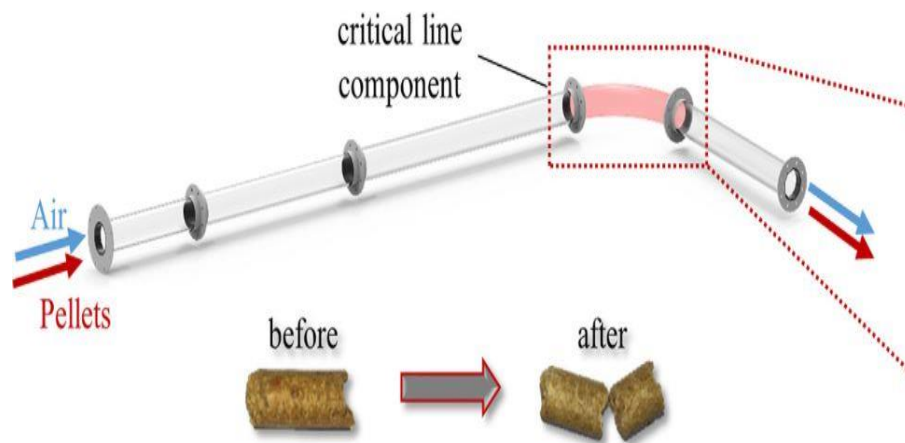


Figure 2.10: A schematic view of an experimental setup for monitoring pellet attrition in a small bend [46].

2.3 Modelling of pneumatic conveying systems

In response to conveying issues as highlighted above and a bid to increase operations, control and optimization, a few studies have been carried out and put forward on the use of numerical tools to better understand the conveying system. The entire concept has been focused on understanding flow characteristics as well as the particle behavior and interaction as it flows through the conveying medium at different operational conditions [19].

2.3.1 CFD modelling

Computational fluid dynamics (CFD) has been adopted in recent times for the modeling of gas-solid behaviors through the use of various numerical algorithms in analyzing fluid and particle interactions[48]. This modeling approach which has come quite close to simulating real-time physical processes has experienced massive development over the years as a result of advancements in the area of computer technology, outputting more precise results in gas-solids simulation[49]. According to Parker *et al.*[50], the choice of the numerical method adopted in simulating multiphase flows involving one or more particulate phases is extremely crucial due

to the complexity of such flows. The right choice is to be made in a bid to reflect not just the particle-fluid interactions but also to capture in a three-dimensional manner, the interactions between the particles and the wall as well as between particles themselves irrespective of the size classification.

In view of the above, the CFD multiphase modeling of gas-solids can be classified using two basic prevalent approaches, the Eulerian-Eulerian and the Eulerian-Lagrangian methods[51]. Figure 2.11 shows a concise summary of the different approaches and associated models as captured by Ariyaratne *et al.*[52]. The granular flow model is approached in an Eulerian-Eulerian way while under the Eulerian-Lagrangian approach, models like the Discrete Phase Model (DPM), Dense Discrete Phase Model infused with the Kinetic Theory of Granular Flow (DDM-KTGF), MultiPhase-Particle-In-Cell (MP-PIC) and the CFD-Discrete Element Method (CFD-DEM) are adopted.

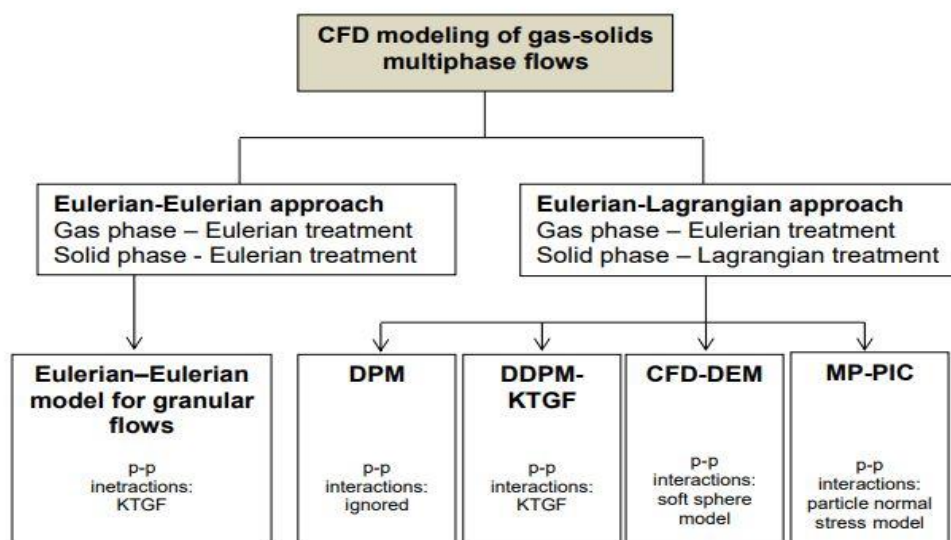


Figure 2.11: Model approach for gas-solid multiphase flow modelling[53].

In the Eulerian-Eulerian approach, the gas and solid phases are modelled as continuous phases in which the solids are modelled as pseudo-fluids completely dissolved in the primary fluid[54], [55]. This method can also model a special kind of interaction referred to as the continuous to continuous phase interaction for immiscible fluids in which interface tracking between Eulerian cells are of key interest[56]. On the other hand, the Eulerian-Lagrangian method uses a different approach in which the particles are seen as discrete or distinct entities, tracked along a specific trajectory while the fluid is modeled as a continuous phase, having fluid characteristics as functions of space and time[57], [58]. Figure 2.11 also informs that the particle-particle (p-p) interaction nature of these models can also be used to differentiate them as some exhibit no p-p interactions while others may do so via different means[53].

2.3.2 MP-PIC modelling – CPFD scheme

Significant results in the development of the Particle-In-Cell method adopted for the modelling of single flow systems led to the birth of the MultiPhase-Particle-In-Cell approach[59]. By integrating the MP-PIC approach with the CPFD scheme, resolving the gas-solid flow gives results that are close to the real behavior of the multiphase flow. The CPFD scheme adopts the

use of parcels which are fractional numbers of real particles and models the forces exerted by these particles on each other during interaction as a function of position and time. This births a normal stress function used in describing the particle collisions[60]. The MP-PIC focuses on the dynamics of the particles themselves. A distribution function containing key properties of the particles such as velocity, mass, time, position, etc., is solved by the use of a transport equation referred to as the Liouville equation[61]. The advantages of this method over other sighted models in figure 2.11 can be explained below.

The Eulerian-Lagrangian MP-PIC approach of resolving gas-solid flows can correctly model dense phase systems as well as dilute phase flows by integrating the right drag model for resolving forces on particles. Volume fractions of particles from dilute (<0.001) to dense (>0.6) can be modelled[53]. Also, by using the method of parcels, it has the capability of modelling real particles up to a count of 1×10^{15} at a reduced simulation cost[62]. It has found application in some open/commercial soft wares such as Barracuda VR[®], Arena-Flow[®], OpenFOAM[®], etc. The Barracuda VR[®] commercial software has been adopted in this report for studying the gas-pellet flow inside a HDPE conveying pipe.

2.3.3 Governing equations

The CPDF scheme as earlier stated adopts the Eulerian-Lagrangian approach. The fluid phase is resolved in the Eulerian grid using the mass and momentum conservation equations while the particle phase is treated using the lagrangian approach in which particles are tracked along a trajectory and represented using the probability distribution function (PDF)[63].

Equation 2.4 represents the continuity equation for resolving the fluid phase in which there is no mass transfer between the interphase[64].

$$\frac{\partial \theta_f}{\partial t} + \nabla \cdot (\theta_f \mathbf{u}_f) = 0 \quad (2.4)$$

Equation 2.5 describes the fluid momentum equation where ρ_f is the fluid density, F is the rate of change of momentum per volume between the particle phase and the fluid phase. Compressibility is assumed for the fluid phase while both fluid and particle phases are isothermal, g is the acceleration due to gravity, and P_f is the fluid pressure.

$$\frac{\partial (\theta_f \mathbf{u}_f)}{\partial t} + \nabla \cdot (\theta_f \mathbf{u}_f) = -\frac{1}{\rho_f} \nabla P_f - \frac{1}{\rho_f} F + g \theta_f \quad (2.5)$$

The dynamics associated with the particle phase has been expressed with the particle probability distribution function given as $\phi(x, u_p, \rho_p, \Omega_p, t)$ having x as the position of the particle, u_p is expressed as the velocity of the particle, t is time, Ω_p is the volume of particle and ρ_p is the density of the particle[59].

Solving the Liouville equation presented in equation 2.6 yields a time evolution for the particle distribution function[65]. Where A , the acceleration for the distinct particles is expressed in equation 2.7 and Δ_{up} is referred to as a divergence operator related to the particle velocity.

$$\frac{\partial \phi}{\partial t} + \nabla \cdot (\phi \mathbf{u}_p) + \nabla_{up} \cdot (\phi \mathbf{A}) = 0 \quad (2.6)$$

In equation 2.7, the first term on the right-hand side expresses the aerodynamic drag which is further detailed in section 2.3.4, the second term defines the pressure gradient, the third term tells about the inter-particle stress gradient while the fourth term is the gravity[66]

$$A = D_p(\mathbf{u}_f - \mathbf{u}_p) - \left(\frac{1}{\rho_p} \Delta P + \frac{1}{\theta_p \rho_p} \tau \right) + g \quad (2.7)$$

The particle stress function is given by equation 2.8 and accounts for the collisions between particles in the model. It is a function of the particle volume fraction which is derived from mapping the particle volume to the Eulerian grid[59].

$$\tau(\theta_p) = \frac{10P_s \theta_p^\beta}{\max[\theta_{cp} - \theta_p, \varepsilon(1 - \theta_p)]} \quad (2.8)$$

Where, τ = Stress function, θ_p = particle volume fraction, P_s is a constant having units of pressure, θ_{cp} = particle volume fraction at close pack, β is a constant having values ranging between 2 and 5, and ε a small number usually in the order of 10^{-7} .

Equation 2.9 shows the ratio between the bulk density ρ_b and the particle density ρ_p which is also referred to as the envelope density, the actual particle density, accounting for the mass of the particle per unit volume of the solid and the gas space within the solid.

$$\theta_{cp} = \frac{\rho_b}{\rho_p} \quad (2.9)$$

2.3.4 Drag models

The forces acting on particles by a fluid as they are pneumatically transported affect the hydrodynamics of the transport process and are a function of the fluid and particle properties as well as the flow condition. All the drag models in Barracuda calculate the force on the particle by using equation 2.10. This force is a function of the particle mass, the drag function, as well as the fluid and particle velocities[67]. The drag function however depends on the drag coefficient, the fluid properties and Reynolds number as shown in equations 2.10 and 2.12.

Geldarts classification of particles into different groups according to their size distribution under the influence of air as a fluidizing agent is shown in figure 2.12, illustrating the gas-solid hydrodynamics during a fluidization process. The physical properties of particles has an effect on their conveying behavior through a fluid and the choice of drag model will greatly depend on the nature of the particle to be conveyed. The group C particles are extremely fine powders and due to great cohesive forces or inter-particle van der Waals forces predominating the hydrodynamics of the system, they are quite difficult to fluidize. They have a particle mean diameter of less than 0.002cm[68]. The A particles are fine and easy to fluidize, having homogeneous and steady bubble formation quite suitable for reaction bed fluidization with a particle size ranging from 0.003cm to 0.001cm. The group B particles on the other hand falling

within a range of 0.001 cm to about 0.08 cm can also be fluidized but with unsteady bubble formation as particle sizes are coarser than those of the A group.

The C particles can be conveyed pneumatically in a dilute phase with an efficient feeding system but are not good candidates for dense phase conveying. The B particles can be conveyed in dilute phase systems also but pose difficulties when conveyed in dense phase systems at high solid loading ratios with associated pipe vibrations during transport. The group A particles according to Wypych [69], are the best candidates for dense phase system designed for high solid loading ratios. The group D particles according to Geldart cannot be easily fluidized and will most likely experience spouting and can be categorized as particles having a mean particle size above 0.1cm. In a dense phase conveying system (low-velocity slug-flow), D particles have been suggested to be good candidates, offering a rather low solid loading ratio in comparison to the A particle[69]. However, extensive focus has not been given to the group D particles especially as it has to do with dilute phase pneumatic transport, the interest in this work is to study the behavior of this group of particle in a dilute phase system at considerable high velocities.

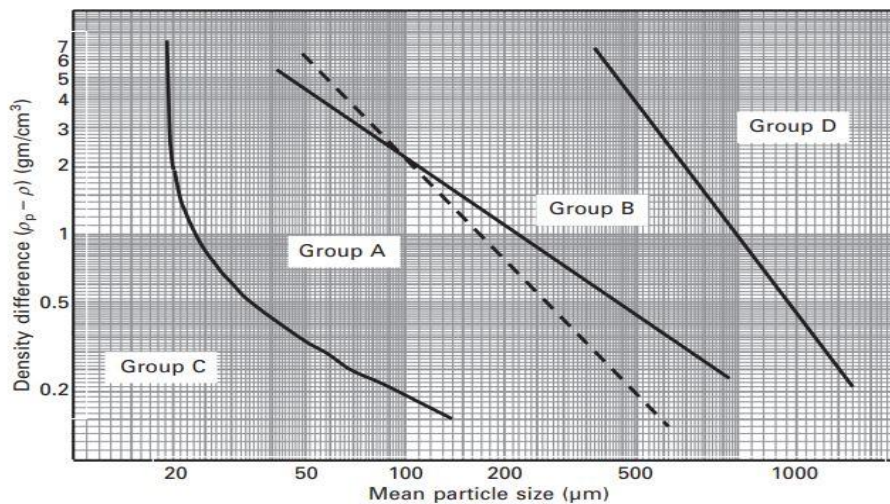


Figure 2.12: Geldart classification of particles for air at ambient conditions[68].

Therefore, the peculiarity of this work hinges on the fact that there is a need to test the feasibility of developing a model that can simulate the pneumatic transport of 1cm Geldart D fish feed pellets using Barracuda in a dilute phase system. To achieve this, it is important to define the right drag model or set of drag models capable of representing the actual hydrodynamics of the pneumatic system. In view of the above, the following Barracuda default drag models were considered.

Wen-Yu drag model

This model uses equations 2.11 and 2.10 to calculate the drag coefficient and force on the particle. Mostly adopted for homogeneous fluidized bed systems according to literature and for dilute phase systems with particles having low solid volume fractions[70].

$$F_p = m_p D(u_f - u_p)$$

$$D = C_d \frac{3\rho_g |u_f - u_p|}{8\rho_p r} \quad (2.10)$$

$$C_d = \begin{cases} \frac{24}{\text{Re}} \theta_f^{n_0} & \text{Re} < 0.5 \\ \frac{24}{\text{Re}} \theta_f^{n_0} (c_0 + c_1 \text{Re}^{n_1}) & 0.5 \leq \text{Re} \leq 1000 \\ c_2 \theta_f^{n_0} & \text{Re} > 1000 \end{cases} \quad (2.11)$$

$$\text{Re} = \frac{2\rho_f r_p |u_f - u_p|}{\mu_f} \quad (2.12)$$

Where ρ_f = fluid density, r_p = particle radius, μ_f = fluid viscosity, u_f = fluid velocity, u_p = particle velocity D = Drag function, C_d = Drag coefficient and Re = Reynolds number as shown in Eq. (2.12).

Ergun drag

The Ergun model was mostly designed from dense systems and is quite appropriate to be used at higher solid volume fractions. It adopts a different correlation for the drag function as shown in equation 2.13 and uses this in equation 2.10 to estimate the particle drag force[71].

$$D_2 = 0.5 \left(\frac{c_1 \theta_p}{\theta_f \text{Re}} + c_0 \right) \frac{\rho_f |u_f - u_p|}{r_p \rho_p} \quad (2.13)$$

Where:

$$C_0 = 2$$

$$C_1 = 180$$

Wen-Yu/Ergun blend

This model combines the advantages of both the Wen-Yun and Ergun models, by combining the drag functions of both models and includes a transition function to enable stability during simulations from dilute to dense phase as shown in equation 2.14. It uses this function in equation 2.10 to calculate the particle drag force[72].

$$D = \begin{cases} D_1 & \theta_p < 0.75\theta_{CP} \\ (D_2 - D_1) \left(\frac{\theta_p - 0.75\theta_{CP}}{0.85\theta_{CP} - 0.75\theta_{CP}} \right) + D_1 & 0.75\theta_{CP} \geq \theta_{CP} \geq 0.85\theta_{CP} \\ D_2 & \theta_{CP} > 0.85\theta_{CP} \end{cases} \quad (2.14)$$

Where:

θ_p represents the particle volume fraction

θ_{CP} represents the particle volume fraction at close pack

D_1 is the Wen and Yu interphase drag function defined in Eq. (2.10)

D_2 is the Ergun interphase drag function defined in Eq. (2.13)

D is a combination of the interphase drag models of Wen-Yu/Ergun as defined in Eq. (2.14)

Turton and Levenspiel

Equation 2.15 shows the drag coefficient as suggested by Turton and Levenspiel[73].

$$C_d = \frac{24}{\text{Re}} (c_0 + c_1 \text{Re}^{n_1}) \theta_f^{n_0} + \frac{c_2}{1 + c_3 \text{Re}^{n_2}} \theta_f^{n_0} \quad (2.15)$$

Where;

$$C_0 = 1.0, c_1 = 0.173, c_2 = 0.413, c_3 = 16300, n_0 = -2.65, n_1 = 0.657, n_2 = -1.09$$

Richardson, Davidson and Harrison

Equation 2.16 gives the drag coefficient upon which the model is built [74].

$$C_d = \begin{cases} \frac{24}{\text{Re}} & \text{Re} < 0.2 \\ \frac{24}{\text{Re}} + 24c_0 \text{Re}^{n_0-1} & 0.2 \leq \text{Re} \leq 500 \\ c_1 & \text{Re} > 1000 \end{cases} \quad (2.16)$$

Where:

$$C_0 = 0.15$$

$$C_1 = 0.44$$

$$n_0 = 0.687$$

Haider-Levenspiel

The drag model from the Haider-Levenspiel has been adopted from [73] for spherically shaped objects. Where the drag function is calculated using equations 2.17 – 2.18.

$$D = \frac{9\mu_f}{2r_p^2 \rho_p} f_h \quad (2.17)$$

$$D = 1 + c_0 \text{Re}^{n_0} + \frac{c_1 \text{Re}^2}{\text{Re} + c_2} \quad (2.18)$$

Where:

$$C_0 = 0.14017$$

$$C_1 = 0.19197$$

$$C_2 = 2682.5$$

$$n_0 = 0.6529$$

To account for the particle sphericity, the non-spherical models of Ganser and Haider-Levenspiel [73] were used as shown in Eqs. (2.19) - (2.20) and Eq. (2.21) respectively. Particle sphericity of 0.87 was used for these models.

Non-spherical Ganser

$$C_d = \theta_f^{n_0} K_2 \left[\frac{24}{\text{Re } K_1 K_2} \left[1 + c_0 (\text{Re } K_1 K_2^{(n_1)}) \right] + \frac{24c_1}{1 + \frac{c_2}{\text{Re } K_1 K_2}} \right] \quad (2.19)$$

$$K_1 = \frac{3}{1 + 2\psi^{-0.5}} \quad K_2 = 10^{n_2(-\log\psi)^{n_3}} \quad (2.20)$$

Where;

$C_0 = 0.1118$, $c_1 = 0.01794$, $c_2 = 3305$, $n_0 = -2.65$, $n_1 = 0.6567$, $n_2 = 1.8148$, $n_3 = 0.5743$, ψ =particle sphericity, K_1 and K_2 are isometric constants

Non-spherical Haider-Levenspiel

$$C_d = \theta_f^{n_0} \left[\frac{24}{\text{Re}} \left[1 + c_0 \exp(n_1\psi) \text{Re}^{(n_2+n_3\psi)} \right] + \frac{24c_1 \exp(n_4\psi) \text{Re}}{\text{Re} + c_2 \exp(n_5\psi)} \right] \quad (2.21)$$

Where

$C_0 = 8.1716$, $c_1 = 3.0704$, $c_2 = 3.0704$, $n_0 = -2.65$, $n_1 = -4.0655$, $n_2 = 0.0964$, $n_3 = 0.5565$, $n_4 = -5.0748$, $n_5 = 6.2122$, ψ =particle sphericity.

2.3.5 Erosion model

The Barracuda erosion model has been used in this work to track the accumulated impacts of particles on each wall patch in the geometry. The wear on pipe walls is predominantly a function of the particle mass, speed, and impact angle. Equation 2.22 shows the mathematical expression of the impact magnitude[75], [76].

$$I_p = w(\theta_p) m_p^a u_p^b \quad (2.22)$$

Where:

m_p = Mass of particle in kg

u_p = Particle speed in m/s

θ_p = Angle of impact

$w(\theta_p)$ = Weighting factor

a and b = User specific constants representing mass and velocity exponents respectively.

The model creates an erosion index from the particle impacts and normalizes it with the impact area on the geometry. This value is then annualized and outputted with units $kg^a (m/s)^b / m^2 / year$. The intensity of impact exerted on the pipe wall by the solid particles greatly depends on the angle at which they strike the wall. This phenomenon is referred to as angular dependence. In the Barracuda VR[®] erosion model, angular dependence is set based on available knowledge of the wall material and erosion properties. The HDPE pipe has been treated as a ductile material. The Barracuda VR[®] settings for a ductile material was adopted which was collated from the experimental work done by Tilly[77], and presented in table 2.1. 10 possible impact angles have been considered and assigned different weighting factors, the model has been normalized to have a maximum angle of erosion weighted at 1.0, as shown in the Barracuda ductile material row (table 2.1). Furthermore, Tilly and Sage have proposed the use of 2.5 as a velocity exponent suitable for ductile materials[78], while a default value of 1.5 has been adopted as the mass exponent.

Table 2.1: Angular weights for a ductile material property as taken from Tilly[77].

Impact Angle (degrees)	0.0	5.7	11.5	17.5	23.6	30.0	36.9	44.4	53.1	64.2	90.0
Barracuda ductile material	0.00	0.41	1.00	0.97	0.82	0.74	0.53	0.44	0.33	0.18	0.03

2.4 Previous studies

Of importance is the fact that most work done and published in recent years that has adopted the CPFD numerical scheme incorporated with the MP-PIC method using the Barracuda software has greatly focused on fine particles with little work done on coarser particles to the best of the author's knowledge. Fluidized bed applications in different forms (bubbling, circulating, combustion, catalytic cracking, etc.) and fluidized bed gasifiers, have been extensively modeled using this approach. Works of literature that discussed the pneumatic transport and erosion modeling of group D particles using the CPFD method and Barracuda VR[®] are extremely scant.

Amarasinghe *et al*[79] adopted the CPFD approach in modeling the minimum fluidization velocity for zirconia, bronze, and steel which are classified under Geldart A, B, and D particles respectively. Different drag models available in the Barracuda software were incorporated during this study but only two were reported to be successful in predicting results that were close to experimental data. The Wen-Yu and WenYu-Ergun models gave very close results to experimental data for group B and D particles respectively. While investigating erosion impact and pressure distribution on a circulating fluidized bed using A particles at a velocity of 7.7m/s, Dwivedi *et al* [76], discovered that pressure drop increased with bed height and erosion impact was spotted at the riser exit where flow directions changed. The Gidaspow and EMMS drag

Literature review

models were adopted in the Barracuda software and they proposed good predictions with the EMMS model for erosion simulation using the A particles. Using the Eulerian-Lagrangian approach on an OpenFOAM framework, Kut *et al*[80], investigated the influence of drag force correlations on a bubbling fluidized bed for Geldart D particles using the Gidaspow model (a combination of the Wen-Yu and Ergun model), De Felice, and EHKL models. His results showed that the Wen-Yu and Ergun blend was capable of predicting pressure values close to experimental data with much lower frequency fluctuations. Mills *et al* [36], conducted an experiment that was quite representative of the dilute phase pneumatic conveying in steel bends using silica particles of 0.023cm size and in the velocity range of 15-35 m/s. The solid loading ratios were in a range of 0.5 to 8 and the steel bend was eroded by the large batches of silica at the above velocities. Vashisth and Grace [34], Investigated the concept of particle roping and fluid rotation during pneumatic transport of pulverized coal, glass beads, and polypropylene belonging to Geldarts group A, B, and D particles respectively. Particle flow behavior in a 90⁰ bend and two circular elbows were studied using the Eulerian-Lagrangian approach. Results showed that properties such as the drag force, bend geometry, gas velocity, solid transport rate, particle density, and particle diameter will affect particle flow behavior.

In this work, an investigation has been done on the particle size of 1cm (10, 000 μ m) which falls far into the D particle region. Unlike the highlighted works of literature, a focus is placed on using the CPFD numerical scheme by adopting the MP-PIC approach to study the flow behavior of this particle size during pneumatic transport at transport velocities ranging from 14.7m/s to 32m/s, there is currently no literature with similar research focused on using Barracuda VR[®] to model such system at the stipulated velocity range. Owing to the impact of drag forces on the flow behavior of particles as well as limited literature on the most appropriate drag model to adopt, different drag models were tested with pressure drop distribution along the pipe compared with experimental data. Also, a qualitative investigation of erosion intensity at the pipe bend region has been carried out.

3 Materials and methods

Figure 3.1 explains the process adopted in the course of this research. The pressure drop and erosion test investigations have been carried out using the pilot rig setup for pneumatic conveying present at the University of Southeastern Norway (USN) which is owned and managed by SINTEF Tel-Tek, an independent organization with a focus on industrial research, academic research, project developments, etc. Pellets were filled into the feeding tank and transported along the pipe using compressed air, then collected at the pickup point inside the receiving tank and further discharged into the feeding tank with the help of pneumatic control valves. This process concluded a round of experiments and data was collated using a software package (LabVIEW[®]). The experimental data was subsequently used in the CFPD software (Barracuda VR[®]) for simulations, final results was compared and analyzed based on the experiments and simulations. A breakdown of the experimental setup and detailed procedures are reported in subsequent sections of this chapter, while other laboratory works carried out on the calculation of the bend radius, pellet diameter, and close pack density have been reported in appendix C, D, and E respectively. Mono-sized pellets of approximately 1 cm diameter were used in this study and details of the pellet properties as given by the supplier can be found in appendix A.

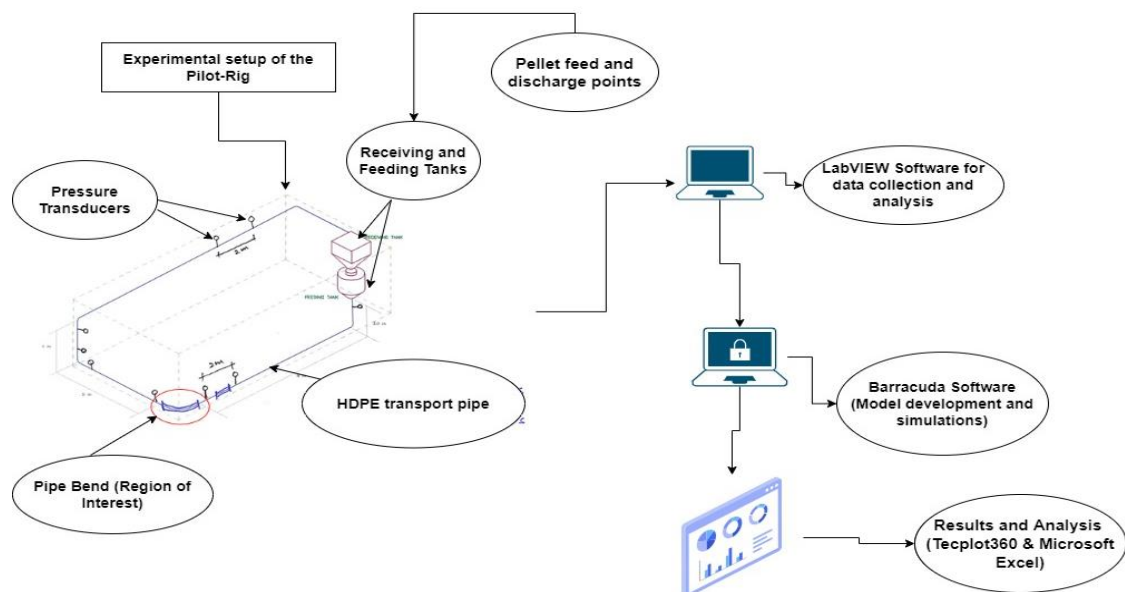


Figure 3.1: Project process flow diagram.

3.1 Experimental setup

The pilot test rig as seen in figure 3.2 has been well equipped for running pneumatic conveying experiments both for the dilute and dense phase systems. The complete conveying system and configuration is a combination of some basic industrial components such as the feeding tank, the rotary valve, different pipe sections, the discharge tank and gas-solid separator, as well as different measuring instruments, data acquisition and analysis tools. The setup has been arranged in a closed-loop circuit system, sequentially connecting each component to the other with the receiving tank placed above the feeding tank, discharging the transported pellets back

Materials and methods

to the feeder after a complete round of test. This implies that different tests can be carried out concurrently without obstructions until there is a need for a complete change of pellets.



Figure 3.2: Pictorial view of the pilot test rig.

3.2 Instrumentation

3.2.1 Feeding tank

The capacity of the feeding tank as shown in figure 3.3 is 3m^3 with the ability to cushion pressure of 10bar. The top of the feeding tank is connected to the bottom of the receiving tank in this setup while the bottom of the feeding tank is connected to a rotary feeder with a capacity of 0.75kW.



Figure 3.3: Picture of the pellet feeding tank.

3.2.2 Receiving tank

The receiving tank has a capacity of 2.5m^3 and serves the purpose of collecting the transported material going through the pipeline. Figure 3.4 shows the receiving tank, mounted on top of four load/weight cells above the feeding tank. These load cells act as transducers and aid in calculating solid transport rate through the conversion of loads acting on the cells, into analog electrical signals which are sent to the control panel [81], [82].



Figure 3.4: View of the receiving tank.

3.2.3 Conveying pipes

For this experimental setup a pipe size with an external and internal diameter of 90mm and 75mm respectively, has been adopted with a total length of 20m, manufactured by HallingPlast. The pipe layout includes vertical but mostly horizontal sections and comes with bends of different radii and configurations like 90°, blind tee, etc. The bend as shown in figure 3.1 with a radius of 170cm was of particular interest in the simulations. A sketch of how the bend radius was defined can be seen in figure 3.5 while a view of the horizontal ground layout of the conveying line is displayed in figure 3.6.

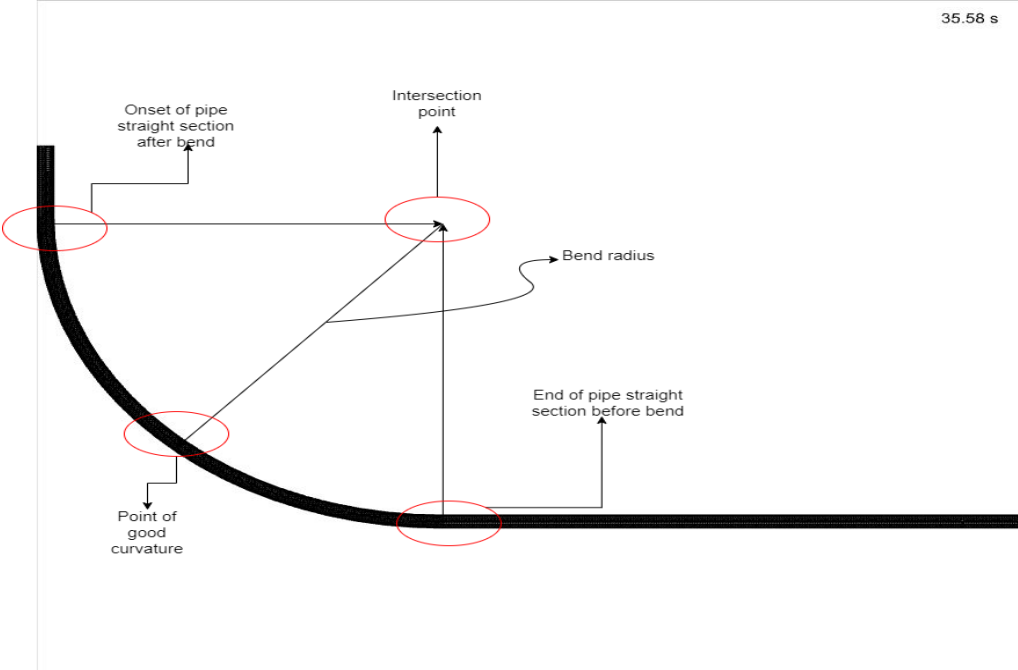


Figure 3.5: Determination of the bend radius.



Figure 3.6: Pictorial display of the horizontal pipe layout in the pilot rig.

3.2.4 Gas-solid separator

In pneumatic conveying, the solid material is usually transported in a gas medium through the pipe and is separated at the end of the transport line with the help of some separation devices which could be a cyclone, bag filter, electrostatic precipitator, etc. In this setup, a 28 filter cartridge system has been used to separate the gas from the pellets as captured in figure 3.7.



Figure 3.7: Gas-solid separator - A 28 filter cartridge system.

3.2.5 Pressure transducers

To collect pressure readings at specific locations to enable the calculation of pressure drop along the pipeline, pressure transducers have been used. Figure 3.8 shows a Druck ptx 1400 pressure transducer, with a 6 bar (gauge) pressure range, having an output of 4 to 20 mA with detailed explanation on the working principle referenced in Ref. [24].



Figure 3.8: Pressure transducer along the pipeline

3.2.6 Control Panel

The pneumatic control panel as shown in figure 3.9 was used in the setup for two basic purposes. First was to convert all electrical analog signals coming from devices like the pressure transducers, the flow meters and load cells into digital signals which can be understood and captured by the PC. The second function was to control the compressed airflow supply valve as well as the top and bottom valves used to redirect the pellets from the receiving tank to the feeding tank.



Figure 3.9: Pneumatic control panel.

3.2.7 Data visualization and storage.

As was previously discussed, the digital signals are fed to a PC as seen in figure 3.10 with the below specifications-

- Rating: 5.6 Windows Experience Index
- Processor: Intel® Core™ i5-6200U CPU @2.30GHz 2.30 GHz

Materials and methods

- Installed memory (RAM): 8.00 GB (7.87 GB usable)
- System type: 64-bit Operating System

The digital signals are visualized and monitored throughout the experiment with the aid of a user-friendly software called the LabVIEW® which has been pre-installed into the device. After each complete test, by clicking the stop icon, LabVIEW® automatically creates and saves the data into a predefined location for further analysis. The choice of which signals to pay greater attention to through monitoring in the course of the experiment can be made under the configuration settings.

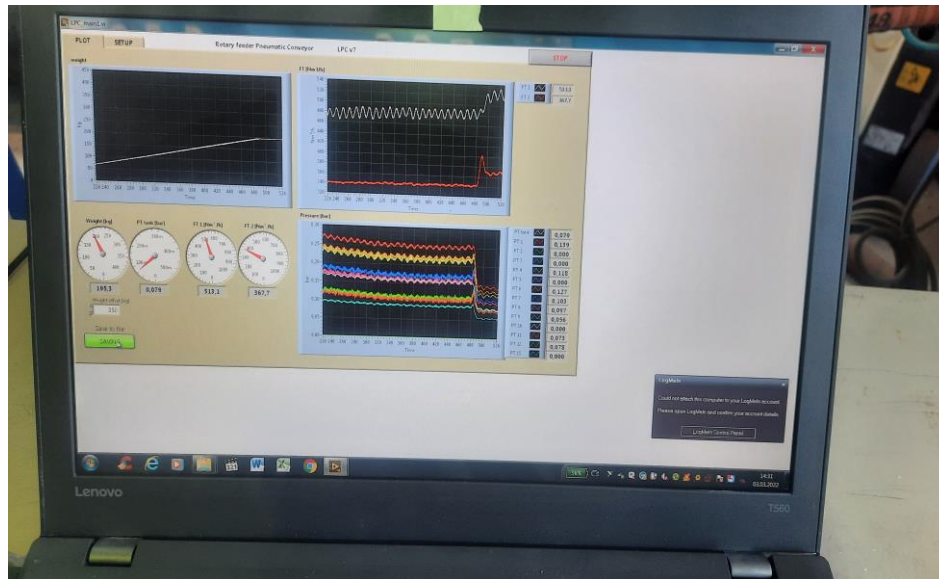


Figure 3.10: LabVIEW signal monitoring mode

3.2.8 The weighing scale

Figure 3.11 displays the weighing scale in the test rig that was used during the experiment.



Figure 3.11: The measuring scale

Materials and methods

The scale was manufactured by Ohaus with a capacity of 100kg. The weight of the pipe bend was initially measured by centrally placing the piece on the scale and marking the measurement positions on the body of the pipe as shown in figure 3.12. This exact position was used to measure the pipe weight after the erosion tests.

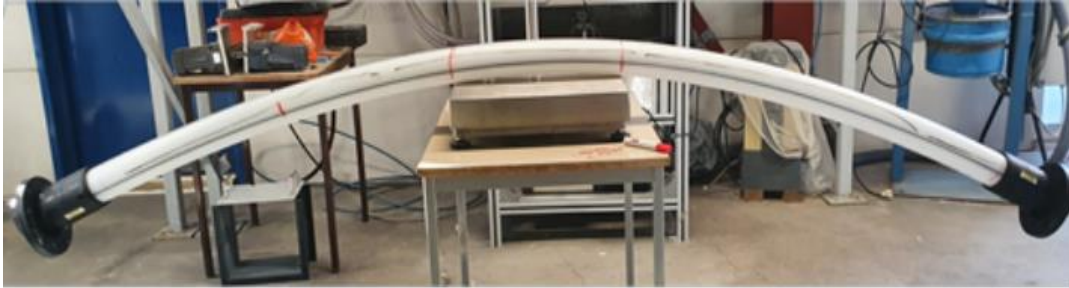


Figure 3.12: A pictorial view of the pipe bend during measurement using the Ohaus scale.

3.2.9 The thickness gauge

A picture of the 45 MG model Olympus thickness gauge is shown in figure 3.13. This instrument has a resolution of ± 0.1 with units in mm and was used for all pipe thickness measurements in this work. It works on the principle of sound energy generated by an ultrasonic transducer[83].



Figure 3.13: Thickness gauge [83].

3.3 Operations

This can be subdivided into two main activities which are the pre-test operations and the post-test operations.

3.3.1 Pre-test operations

This involves all the activities carried out as a means of preparation before the start of the test. The test rig setup is the key pre-test operation carried out in this stage. The provision of the required transport media is done through the working mechanism of an air compressor which feeds the entire rig. Before the compressor was switched on, the dryer/cooler was set to a dryer operating outlet temperature of 4 degrees centigrade to guarantee the supply of treated dry compressed air to the test rig. The compressor, upstream of the dryer was then switched on and allowed to pressurize the entrapped air to about 7 bar before the air supply valve to the pneumatic conveying unit was turned on. The control panel of the pneumatic system was then connected to an electric source and linked to the data analyzing device through a USB cable. The power supply nub in the panel was switched on while the LabVIEW[®] software was powered and ready for data capture and subsequent analysis. The rotary valve feeder was set through the rotary meter shown in figure 3.14 to a frequency of 90 Hz. This frequency value guarantees a solid transport rate between 1.5 to 2 tons per hour, a typical range of what is obtainable in the fish farming industry during pellet transport.



Figure 3.14: Rotary feeder meter as captured in the pilot rig

3.3.2 Post-test operations

This is centered basically around data analysis, averaging, and comparison. The captured and stored data by the software was analyzed sequentially according to the test order, averaging was done for fluctuating data output, and the results obtained was compared with that from simulations. The weight results obtained from the weighing scale was compared with initial values recorded before the tests.

3.4 Test procedure

The procedure for this experiment was sequentially laid out and monitored by SINTEF Tel-Tek. The bend section was weighed and data properly documented, 200kg of pellets was initially transported from the feeding tank to the receiving tank. LabVIEW[®] software was used

Materials and methods

to confirm the exact quantity for transport while the air flow valves were used to control the compressed air supply into the pipeline. Before the rotary feeder was switched on, the cartridge filter was kept as clean as possible. LabVIEW[®] was used to check for initial steady conditions and switched to save mode to capture pressure, flow rate and weight data during transport. A test round was termed to be complete after all the pellets was transported to the receiving tank as captured by the software. To start a fresh round, the pellets in the receiving tank was discharged into the feeding tank using the discharge values on the pneumatic control panel.

To further estimate erosion at the bend section, higher flow rates were adopted while using same procedure as explained above. The test was done consequently for 7 rounds after which a substantial amount of pellets was observed to have crushed and a new batch of 200kg of pellet used for another 7 rounds. This was followed by the removal, cleaning and subsequent weighing of the bend section for further analysis.

4 Simulation setup

The entire simulations carried out in this research was done using Barracuda VR[®] 21.0.1. This software provided by CPF D simulates a three-dimensional multiphase flow by adopting the EulerLagrangian model described in chapter 2. Setting up experimental rigs to test different system behaviors and operations can be extremely expensive and this software eliminates that need by streamlining operational possibilities and improving on varying design concepts. This can hence be used in the physical design of such systems. Furthermore, causes of system underperformance can be identified through simulations and optimization possibilities can therefore be applied. This chapter focuses on the model development procedure for the pneumatic transport of fish pellets.

4.1 Geometry

Figure 4.1 is a plan view of the geometry under investigation, showing measurement details, pressure monitors which are points along the pipe that have been used to track pressure values at different positions, and wall erosion monitors used to capture particle impact effect on the walls of the pipe along the bend. The flow direction is also indicated to aid easy understanding.

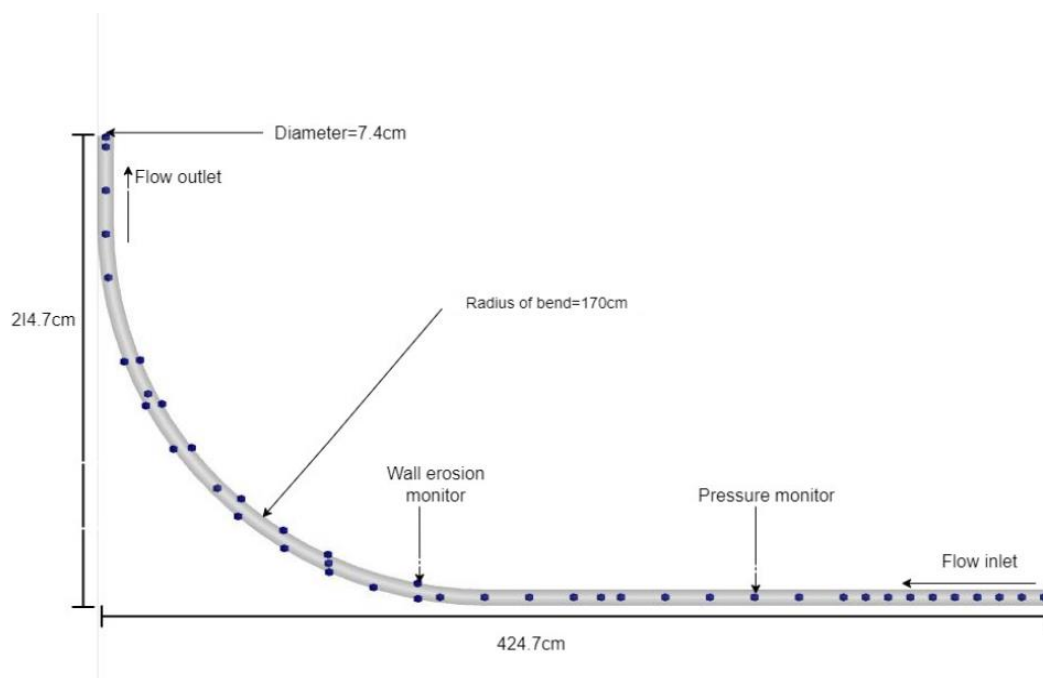


Figure 4.1: Geometry Plan view

4.2 Model setup flow chart

Figure 4.2 shows the stages of setting up the model and this is briefly described in the subsequent subsections.

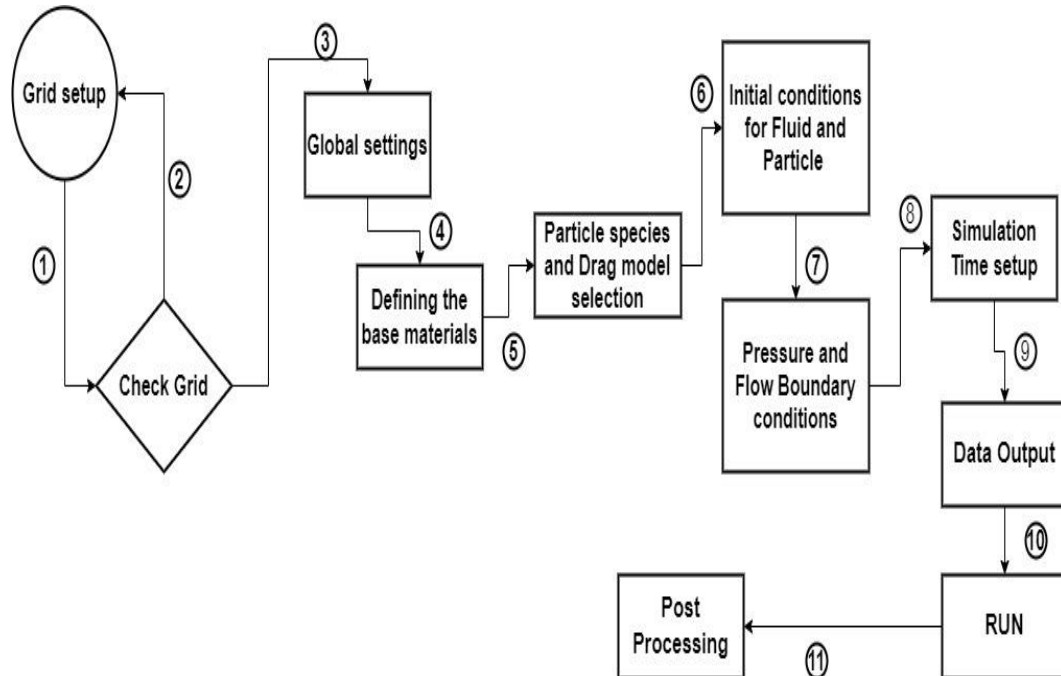


Figure 4.2: Simulation setup flow chart.

4.2.1 Grid setup and grid check

Figure 4.3 shows a screenshot of how the grid was set up while figure 4.4 displays a side view of the gridded geometry. The geometry which is a computer-aided design (CAD) file was imported as an STL file into Barracuda. A uniform grid of 500000 was adopted with 39554 real cells around the geometry to perfectly capture the bend area. Cells having volume fractions lower than 0.04 as well as having an aspect ratio higher than 15:1 were eliminated. This gridding style catered for the even spacing between cells to ensure numerical stability during computation.

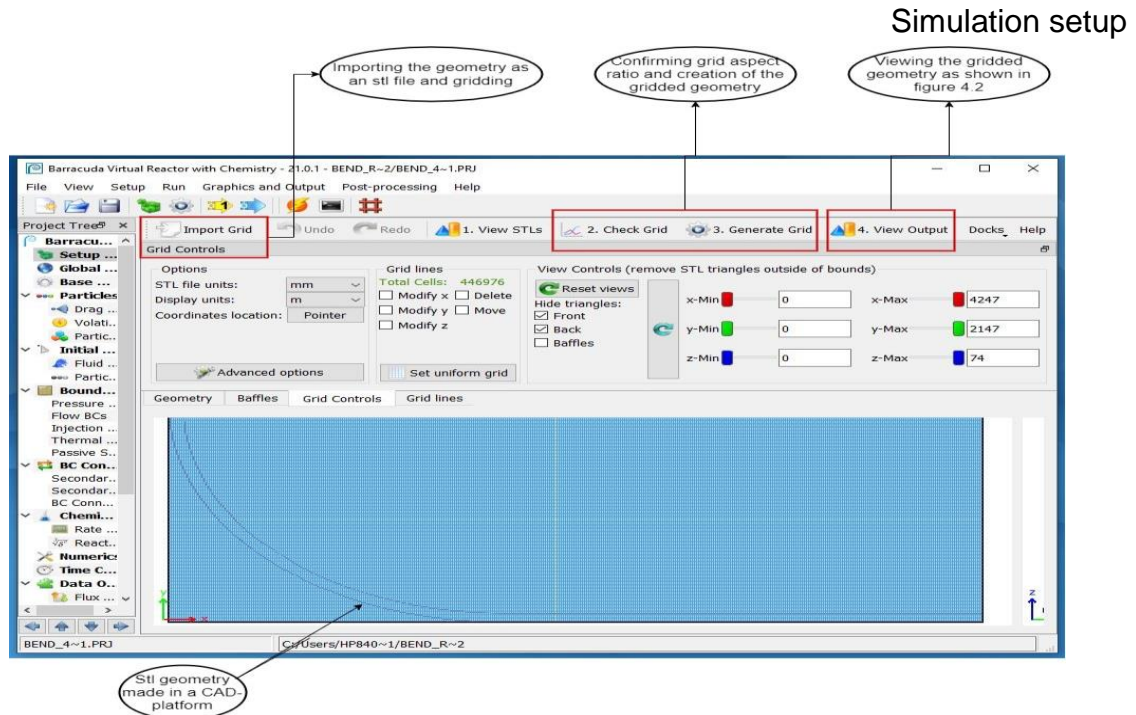


Figure 4.3: Setting and checking the grid.

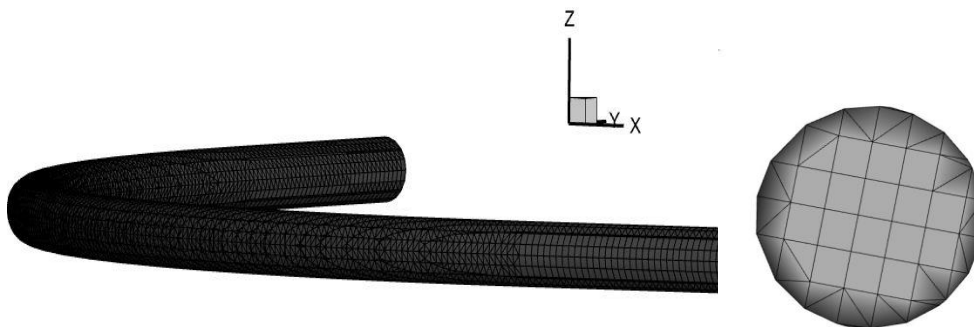


Figure 4.4: 3D side view of the gridded geometry (computational domain) along the x-axis (left) and pipe cross section (right).

4.2.2 Global settings

Figure 4.5 shows the system was simulated under a constant temperature condition (300K), this was decided by considering ambient temperature condition of 25°C under which experiments were carried out. The acceleration due to gravity was kept at -9.8m/s in the z-direction, a resultant effect of the pipe position and flow direction in the pilot rig.

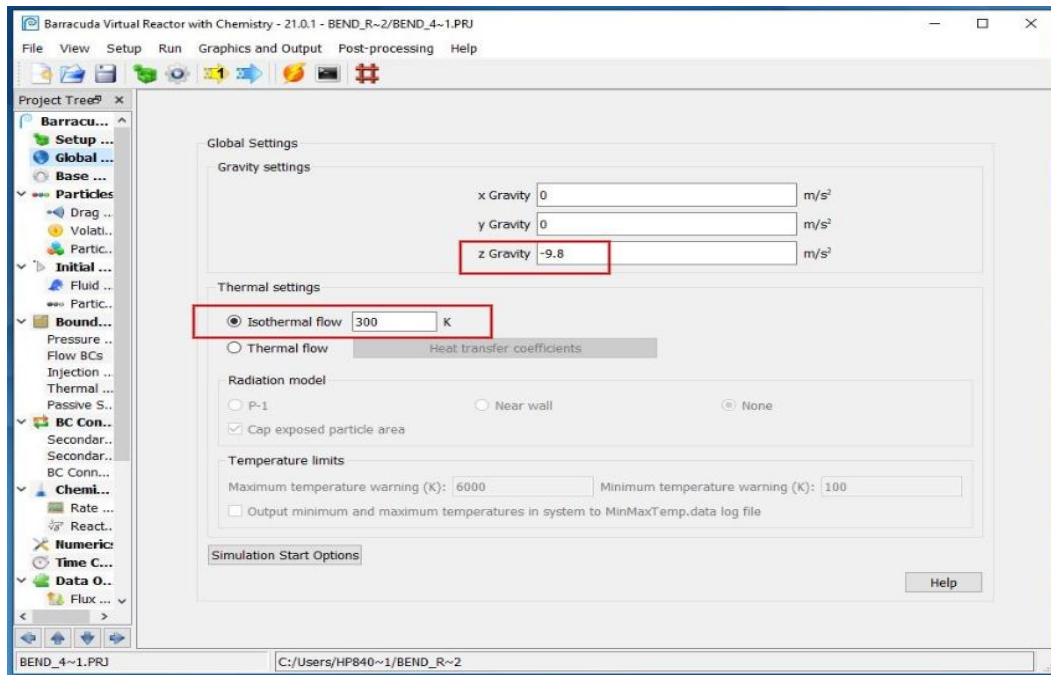


Figure 4.5: Global conditions

4.2.3 Base material definition

Compressed Air was used as the conveying medium and selected from the material library as seen in figure 4.6 while the pellet properties have been defined and added to the list of base materials.

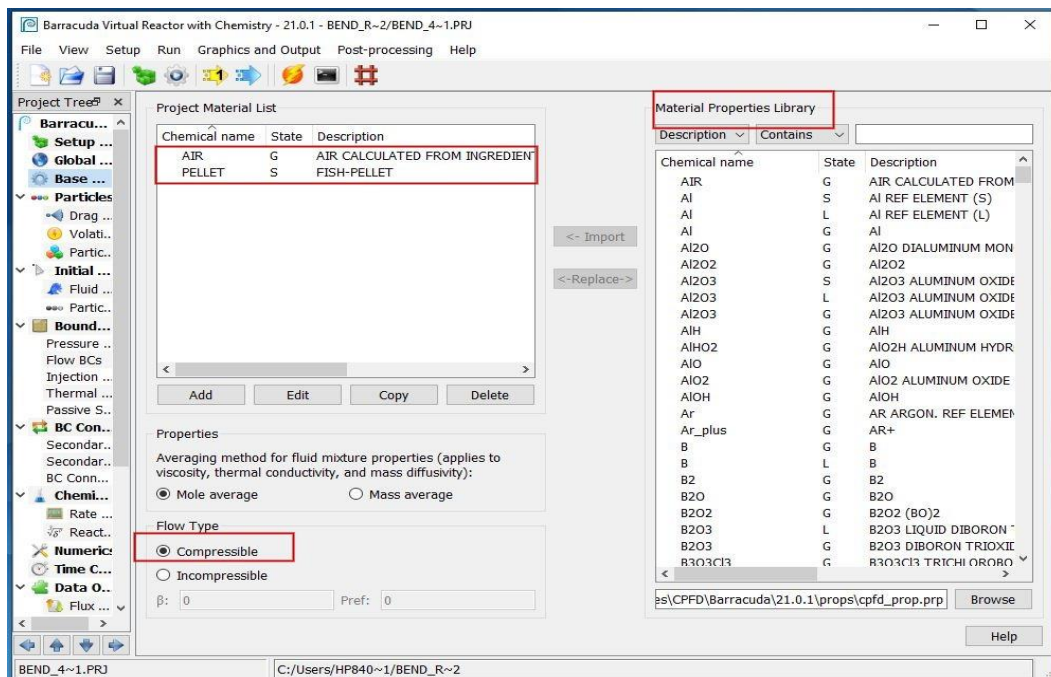


Figure 4.6: Screenshot of base material definition

4.2.4 Particle species and drag model

Figure 4.7 shows a section of the project tree that was used to define the envelope density, drag models, pellet diameter, and sphericity.

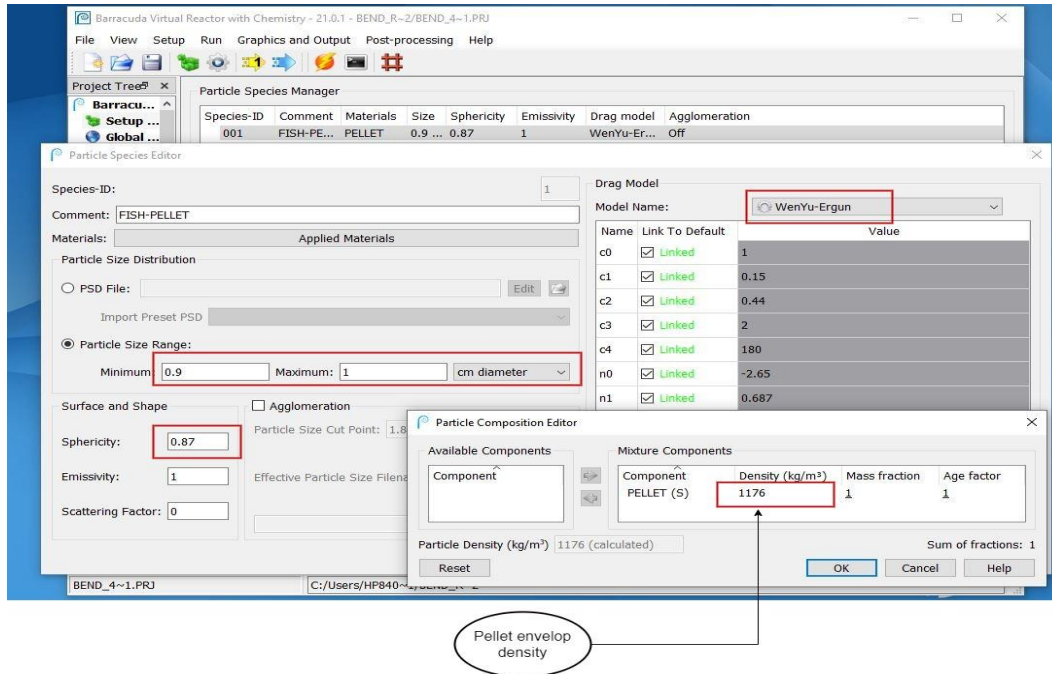


Figure 4.7: Defining pellet properties and drag model

4.2.5 Initial conditions

There was no pellet in the pipe at the initial state, the pipe was completely occupied by air. Figure 4.8 shows how this was represented during the model development phase.

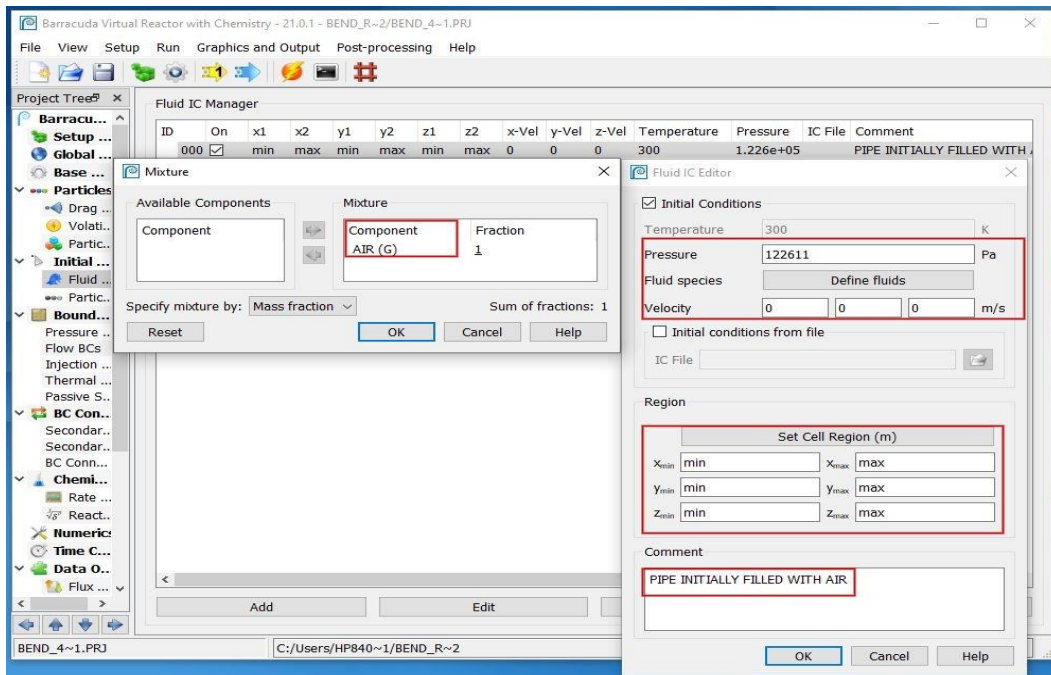


Figure 4.8: Initial condition

4.2.6 Pressure and flow boundary conditions

The flow and pressure boundaries have defined the inlet and outlet boundary conditions, respectively, as shown in figure 4.9. For this work, different inlet and outlet conditions have been tested based on the different experiments that was performed in the rig.

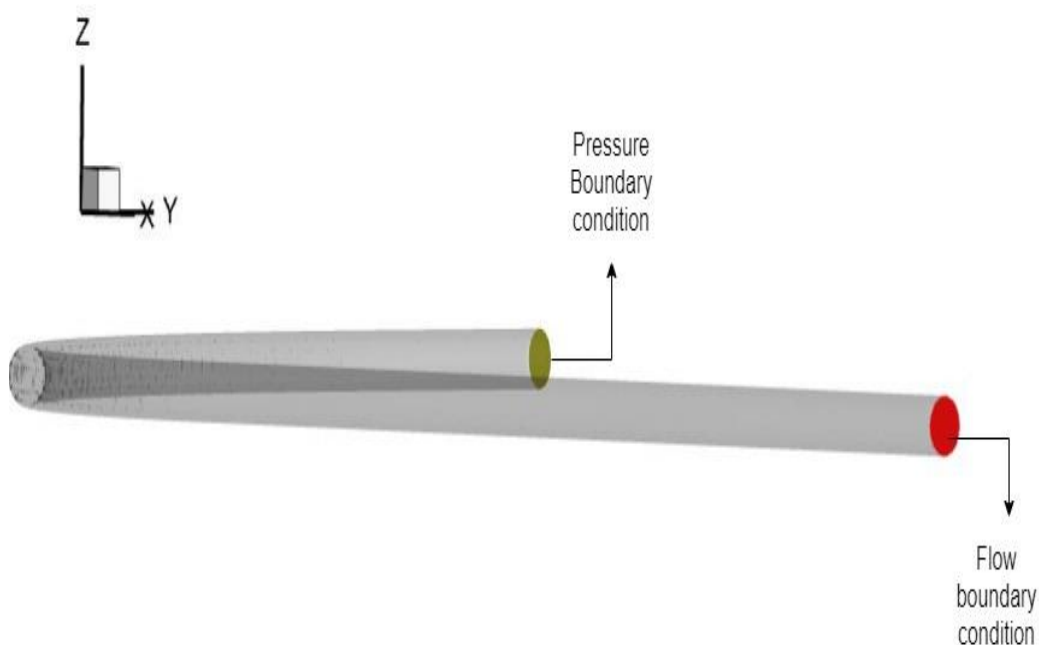


Figure 4.9: A view of the boundary conditions while looking at the geometry from the side along the x-axis

4.2.7 Simulation time, data output, and post-processing

For the production of high frequency and real-time animations, a visualization data output plot interval of 0.05 seconds was selected. Simulation time of 50 seconds at a 0.001-time step was adopted for all simulations to enable a complete capture of the hydrodynamics of the flow and for steady-state conditions to be achieved. Tecplot 360 and Microsoft Excel software was used in the post-processing of data.

4.3 Model parameters

A summary of the model parameters used in the simulation is listed in table 4.1. The close pack volume fraction was gotten from laboratory work as captured in Appendix D, the diffuse bounce was selected based on the particle shape and nature of the wall surface, Barracuda default setting was used for the maximum momentum redirection and tangent-to-wall retention while the normal-to-wall momentum retention was decided based on literature[84], [85].

Table 4.1: Model parameters

The close pack volume fraction	0.56
Maximum momentum redirection (Default)	40%
Normal-to-wall momentum retention	0.85
Tangent-to-wall momentum retention	0.85
Diffuse bounce	5

4.4 Model validation using drag models

To establish base cases that will be deployed in further simulations, eight different drag models were tested, Wen-Yu, WenYu-Ergun, Ergun, Turton-Levenspiel, Richardson-Davidson, Haider-Levenspiel, Nonspherical Ganser, and the Nonspherical-Haider-Levenspiel models at a transport velocity of 23m/s with a solid loading ratio of 4.3. The pressure at transducer 2 for the different models was computed and compared to that obtained from experiments. Figure 4.11 shows a bar chart of the simulated pressure values at transducer 2, positioned at the exact point as in the experiments, with their respective variations from collected experimental values. It is important to note that pressure values from experiments at transducer 1(inlet) and 3(outlet) as shown in figure 4.10 was adopted as boundary conditions during the simulations. Results from the Wen-Yun-Ergun model gave very close predictions to experimental values with the least deviation when compared to the other models.

Observations during further simulations at different velocities showed that for the lower velocity cases, the Ergun model gave more accurate results. The WenYu-Ergun model had the least variation with 8.8% from the experimental value followed by the Ganser and Richardson-

Simulation setup

Davidson models with 9.7% variation. The Turton-Levenspiel, Ergun, Wen-Yun, Haider-Levenspiel, and Nonspherical-Haider-Levenspiel over predicted the pressure at transducer 2 by 10%, 10.7%, 17.4%, 11.9%, and 20.6% respectively. These variations could be attributed to the nature of the pellet size under consideration as was discussed in chapter 2. Based on the above observation, the WenYun-Ergun model and the Ergun model have been adopted for simulating the high and low-velocity cases respectively.

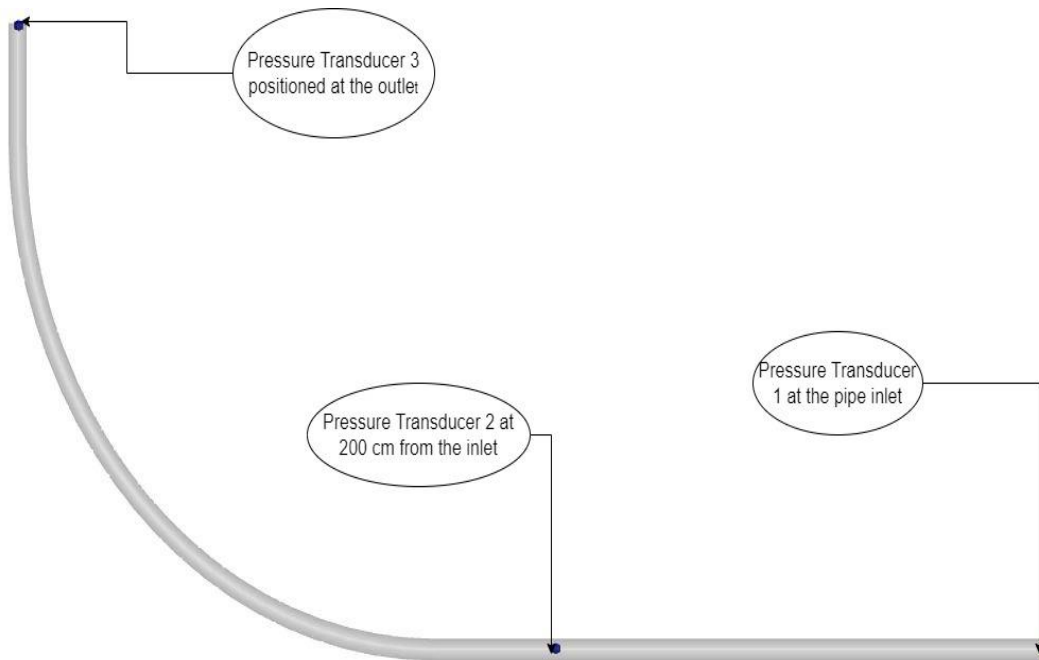


Figure 4.10: Pictorial view of the transducer locations along the pipe.

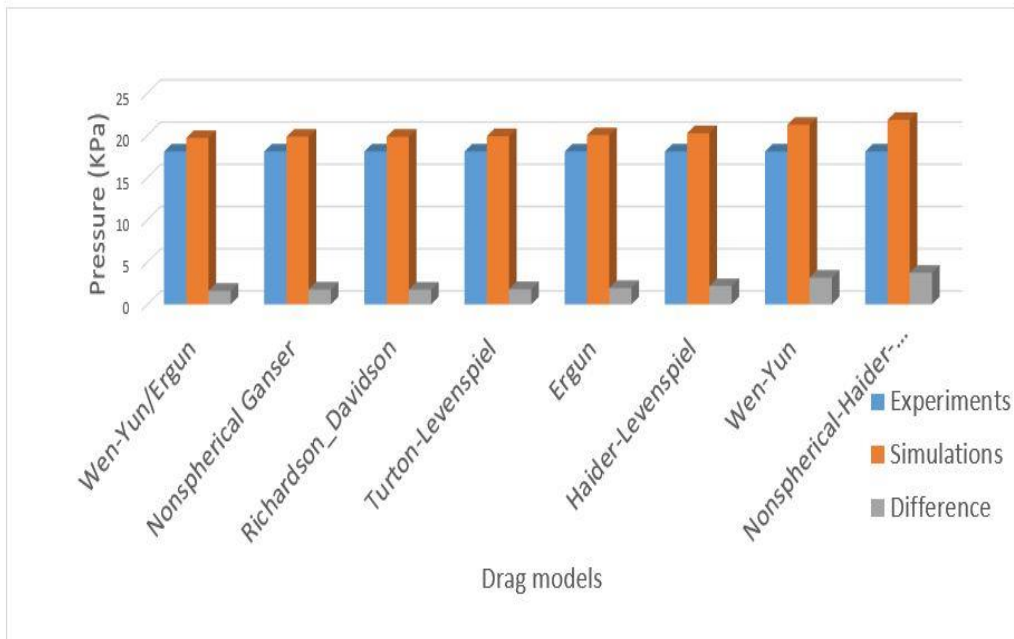


Figure 4.11 Pressure comparison using different drag models at pressure transducer 2 at 23m/s.

5 Results and discussions

5.1 Experimental results

Table 5.1 shows the test results for the experiments carried out in the pilot rig with averaged pressure values, velocity, and solid loading ratio. The batch 1 tests will be referred to as the pressure tests which was carried out to correlate pressure drop to pellets' transport rate under more stable conditions. The batch 2 tests are the erosion tests which were conducted aiming to estimate erosive wear in the conveying pipeline. The batch 2 tests show fluctuating conditions with only tests 1 and 2 showing consistent steady conditions during the transport process. Table 5.2 shows the results that have been used for analysis in the course of this report, where PT1, PT2, and PT3 represent the pressure transducers at 1, 2, and 3 respectively as shown in figure 4.11. These 8 experiments capture the varying velocity range under which various analysis has been drawn. Furthermore, the velocities have been defined as high or low based on applicability in the industry with velocities below 20m/s representing low-velocity transport cases. As this is a feasibility study, the analysis made in subsequent sections is to show quantitatively (through pressure analysis) and qualitatively (through erosion analysis) the potentials of the model to be used in simulating the pneumatic transport of 1cm fish feed pellets through the HDPE pipe.

Table 5.1: Experimental results for the different tests done in the pilot rig.

	Test	PT1		PT2		PT3		Velocity m/s	Solid Loading Ratio —
		Barg	Absolute(Pa)	Barg	Absolute(Pa)	Barg	Absolute(Pa)		
BATCH 1 TEST RESULTS	1	0.134173	114742.32	0.125843	113909.32	0.116782	113003.20	21.58	3.68
	2	0.118501	113175.11	0.111572	112482.17	0.104057	111730.73	18.01	3.85
	3	0.118055	113130.54	0.111041	112429.09	0.103986	111723.63	16.64	4.04
	4	0.140577	115382.75	0.130746	114399.58	0.122491	113574.07	15.78	4.81
	5	0.159913	117316.31	0.146100	115935.00	0.137302	115055.21	14.74	5.42
	6	0.194345	120759.50	0.181032	119428.17	0.168345	118159.49	23.02	4.30
	7	0.194916	120816.62	0.181388	119463.80	0.168865	118211.53	22.80	4.56
	8	0.200955	121420.54	0.186423	119967.26	0.173579	118682.87	22.22	4.85
	9	0.206944	122019.43	0.191771	120502.14	0.178540	119179.02	21.91	5.15
BATCH 2 EROSION TEST RESULTS	1	0.212859	122610.90	0.220276	123352.60	0.088184	110143.40	25.68	3.75
	2	0.520991	153424.21	0.525567	153881.70	0.207640	122089.00	32.11	3.24
	3	0.327441	134069.11	0.333950	134720.82	0.132320	114557.14	28.51	3.60
	4	0.576250	158950.40	0.583120	159637.01	0.230500	124375.27	22.83	4.27
	5	0.561662	157491.20	0.567945	158119.50	0.228589	124183.90	29.63	3.08
	6	0.820347	183359.72	0.819529	183277.93	0.312871	132612.12	15.27	7.74
	7	0.919780	193303.26	0.887655	190090.51	0.340752	135400.20	17.50	6.74
	8	0.924516	193776.61	0.889190	190244.32	0.335320	134857.03	13.84	7.85
	9	0.782817	179606.70	0.758907	177215.75	0.285107	129835.73	17.74	5.44
	10	0.855715	186896.51	0.827733	184098.34	0.316252	132950.16	18.18	5.57
	11	0.841033	185428.35	0.845459	185870.89	0.311334	132458.42	18.30	5.15
	12	0.906890	192013.98	0.863566	187681.57	0.317995	133124.48	18.58	4.47
	13	1.054954	206820.43	1.022972	203622.22	0.390794	140404.41	18.88	3.08

Table 5.2: Experimental results used for analysis.

		Test	PT1	PT2	PT3	Velocity	Solid loading Ratio
			Barg	Barg	Barg	(m/s)	
EROSION TEST	High velocity	1	0.5210	0.5256	0.2076	32	3.24
		2	0.2129	0.2203	0.0882	25.7	3.75
PRESSURE TEST	High velocity	1	0.1943	0.1810	0.1683	23	4.31
		2	0.5763	0.5831	0.2305	22.8	4.27
		3	0.1342	0.1258	0.1168	21.6	3.68
	Low velocity	1	0.1185	0.1116	0.1040	18	3.85
		2	0.1406	0.1307	0.1225	15.8	4.81
		3	0.1599	0.1461	0.1373	14.7	5.42

5.2 Pressure drop analysis

5.2.1 Erosion test - experiment

As earlier mentioned in section 5.1, most of the erosion tests were carried out under unsteady conditions. In the first two tests (table 5.1), it was possible to get steady-state conditions after about 60 seconds of transport but this wasn't the case for the other conducted tests. An increase in pressure value was observed, with the pressure transducer 2 downstream of transducer 1 showing slightly higher values. The air volume flow rate along the pipeline was observed to continuously decline during the transport process. This behavior has been attributed to the use of high velocities which resulted in excessive pellet breakage and oily deposits along the pipeline during transport. It is also possible that the transducers were affected in the process. The top-left and bottom-left of figure 5.1 show pressure and volume flow conditions during test 2 (32m/s) while the top-right and bottom-right of figure 5.1 display pressure and volume flow conditions during test 6 (15.3m/s).

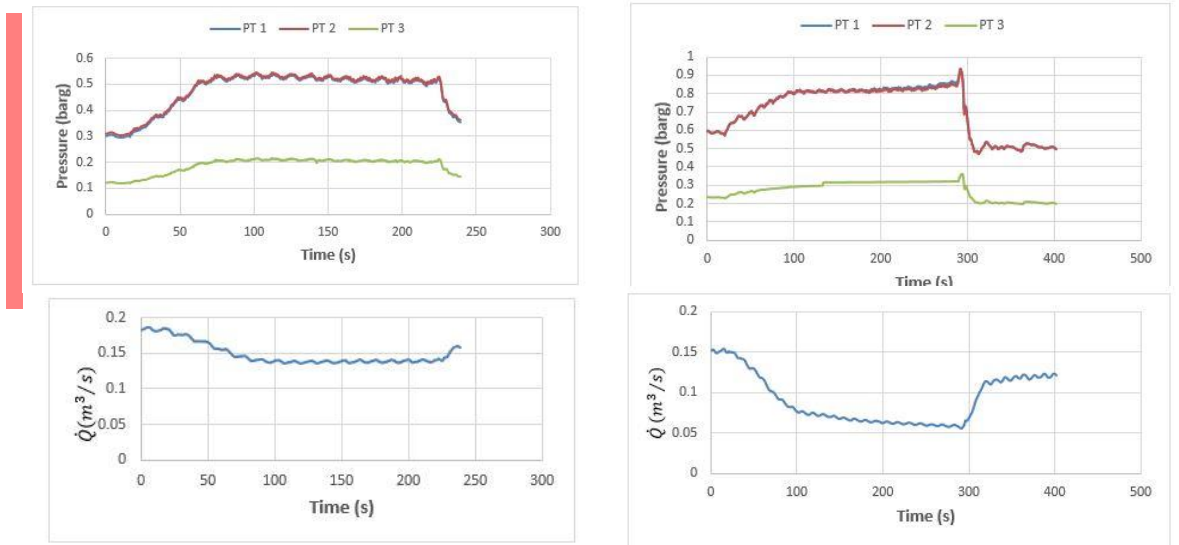


Figure 5.1: Pressure plot at 32m/s (top left), volume flow rate at 32m/s (bottom left), pressure plot at 15.3m/s (top right) and volume flow at 15.3m/s (bottom right).

5.2.2 Erosion test – simulation.

The inlet pressure was set to be higher than the pressure at the exit for the simulations in correspondence to pressure values gotten from experiments at transducers 1 and 3 respectively. Pressure distribution showed a defined decrease from the inlet to the outlet of the pipe. This has accounted for the gas-particle transport along the pipe. However, there was pressure deviations at the inlet but the exit pressures were matching perfectly. These deviations were due to the experimental conditions as earlier described. Between points 20 and 25 as shown in figure 5.2, a sharp and steep pressure drop was observed and these points correlate to the regions immediately after the bend entry and exit points respectively. 27 points were established along the pipe and used to track pressure variations from the inlet to the exit of the pipe as shown in figure 5.3. 10 points from the inlet were positioned 10cm apart to give room for possible unsteady conditions at the pipe inlet, the next 9 points before the bend were placed 20 cm apart while 4 points 50cm apart were established at the bend region. The last 3 points were positioned towards the pipe outlet, 20cm apart while the exit cell was assigned one point to accurately capture and compare outlet pressure conditions. A clearer picture of the points and directions can be seen in figure 5.3.

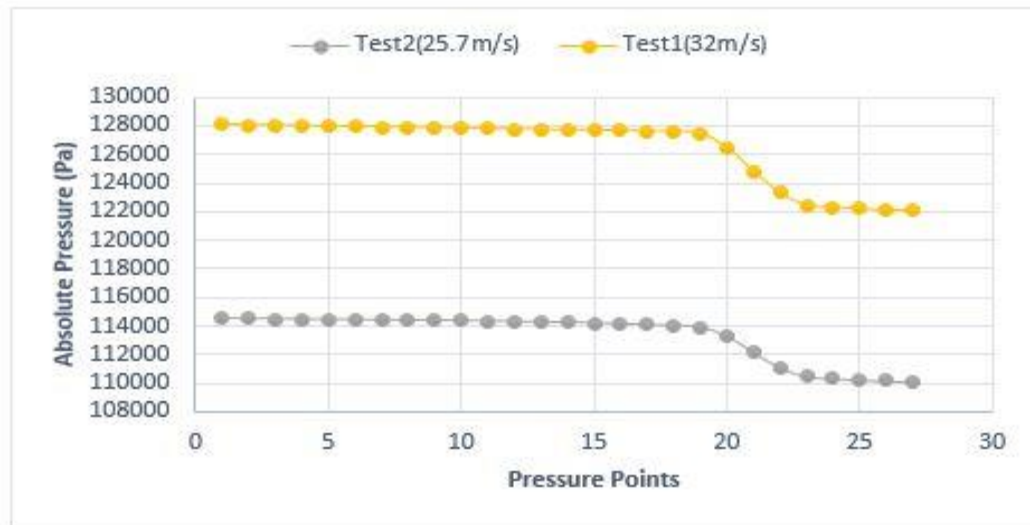


Figure 5.2: Pressure drop for high-velocity erosion tests.

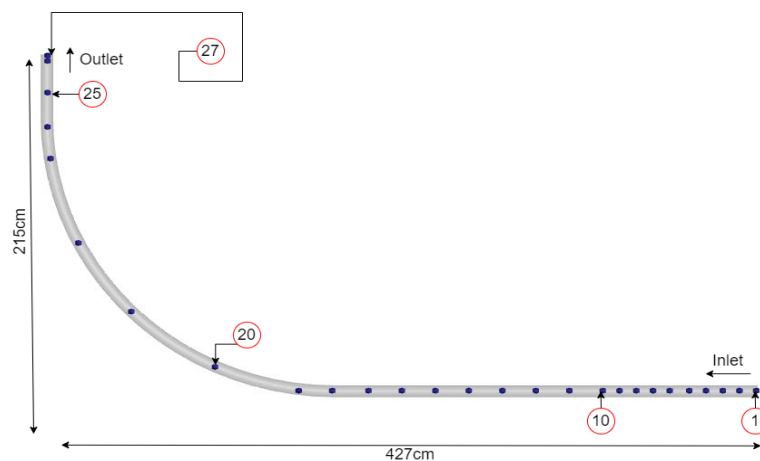


Figure 5.3: Plan view of geometry showing pressure points 20 and 25.

5.2.3 Pressure tests – High and low-velocity cases.

For the high and low-velocity cases as shown in figures 5.4 and 5.5 respectively, a sharp and steep pressure drop was also observed between points 20 and 25 as in the erosion cases. Cai *et al* [86], studied pressure drop along a pipe with different bends and proposed that total pressure drops were noticed to be higher in bend regions than other parts of the pipe, he further explained that, a larger bend radius in a horizontal to horizontal pipe layout experienced steeper pressure drop when compared to bends with smaller radius. Though his observations were similar to what was observed during the simulations, however other works of literature [87], [88] have argued differently, suggesting that as the bend radius increases, the pressure gradient in the bend should experience a decline. The fact remains that the pressure drop along a bend depends on many factors such as the solid loading ratios, the length of the bend, the shape and diameter of the transported particle, the roughness factor of the pipe wall, and local velocity around the

Results and discussions

bend region, etc. Given these, it is difficult to make any concrete assertions since most of these factors have not been comprehensively considered.

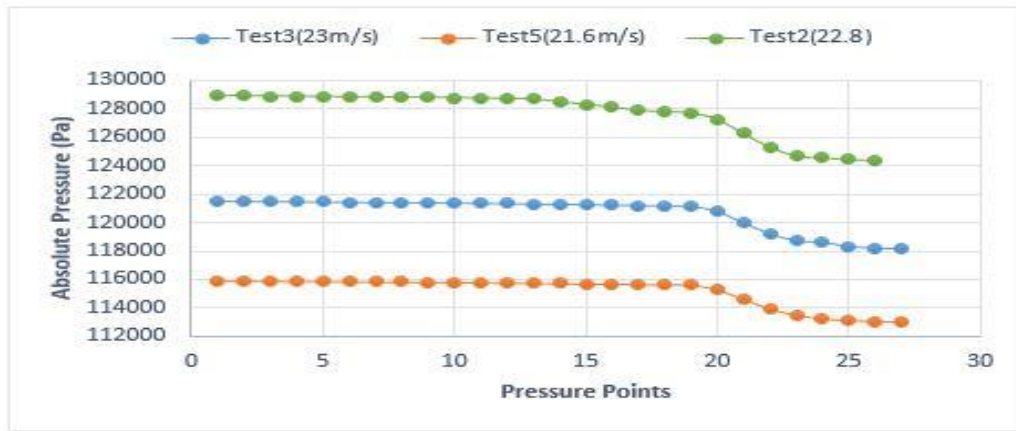


Figure 5.4: Pressure drop for high-velocity pressure test using the Wen Yun-Ergun model.

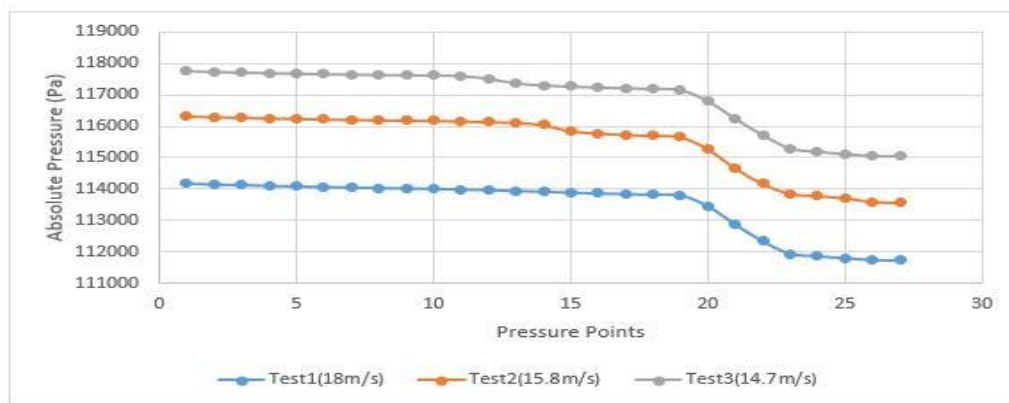


Figure 5.5: Pressure drop for low-velocity pressure tests using the Ergun model.

As was earlier highlighted in chapter 4 (section 4.4), the Wen-Yun and Ergun model could not correctly predict the pressure drop for the low-velocity cases while the Ergun model predicted the cases well, a similar occurrence was observed by Yang *et al*[89] who studied pressure drop in a horizontal pipe for large coal particles between 0.5cm to 2.5cm and results from this work showed that at higher velocities, the adopted DPM (discrete particle method) model showed great feasibility in predicting the conveying behavior but that was not the case as the flow velocity reduced, also research and industrial applications has shown that material nature and transport velocity are key determinants of defining dilute or dense phase transport. It is possible that at the lower velocities, the dense phase region begins to set in and the Ergun model in Barracuda has been developed to accurately reflect the hydrodynamics of dense cases. However, the solid loading ratios 3.85, 4.81, and 5.42 for the low velocity pressure tests 1, 2, and 3 respectively are within the range for a dilute phase transport as given in different works of literature. Nonetheless, since the solid loading ratio is a result of the hydrodynamics in the pipe, further investigations are advised to obtain better clarity. The prediction error between experiment and simulation as reflected in figure 5.6 was 9% for test 3 while for tests 2 and 1 a

value of 10.8% and 12.5% were recorded respectively. Studies and works of literature have suggested that such pressure deviations are quite acceptable for further analysis.

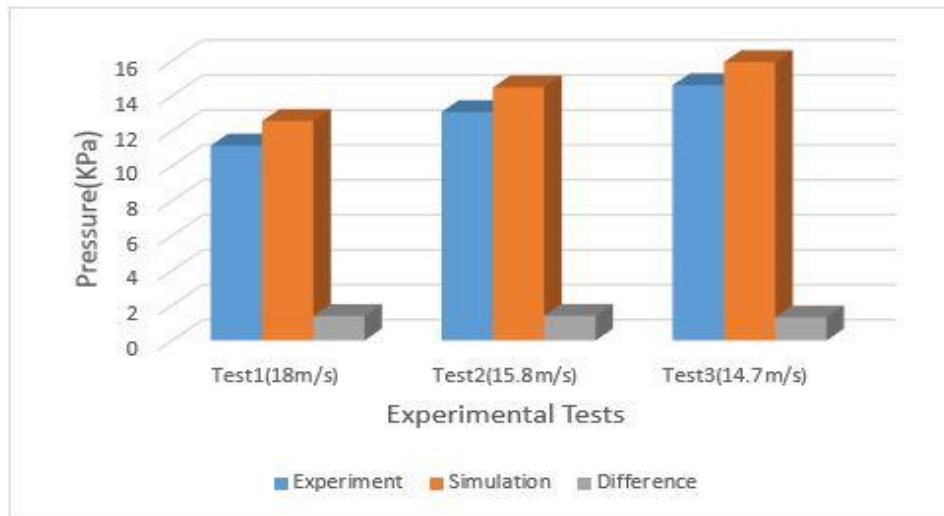


Figure 5.6: Pressure variation at Transducer 2 for low-velocity tests using the Ergun model.

5.3 Particle volume fraction

Analysis of the particle volume fraction has been done based on the erosion test at 25.7m/s and solid loading ratio of 3.75

Figure 5.7 C is a cross-sectional view of the pipe at 0.2m from the inlet showing even and uniform distribution of particles, as they tend to be suspended in the gas stream along the cross-section. Figure 5.7 B shows particle distribution in the pipe cross-section at 1.2m from the inlet with particles observed to lose uniformity and exhibiting segregation, this behavior at this section of the pipe could be attributed to the effect of gravity and loss of particle momentum, another possible explanation could arise from the fact that particles observe or see the upcoming conditions (the bend downstream of the inlet), resulting in particle flow resistance as the fluid and pellet travel through the pipe. This effect was more pronounced at a distance of 2.3m into the pipe along the x-axis as most of the particles congregate in the outer wall region of the pipe towards the bend region as shown in figure 5.8 B. The red color indicates maximum particle concentration along this region with fewer particles moving with the gas stream as indicated by the blue colors. Downstream of the bend at approximately 1.85m in the y-axis it can be observed that particle concentration at the outer walls begins to disperse gradually as seen in figure 5.9 B. Figure 5.9 C is a zoomed cross-sectional view of the pipe at 2.1m in the y-axis towards the pipe exit. It can be seen that most of the initially concentrated particles have been dispersed and uniformity of particle distribution gradually returned.

If the pipe geometry adopted in the simulation was extended in the y-direction, the pellets will be completely suspended in the fluid downstream of the pipe due to the effect of secondary flows. Particle volume analysis as presented above can be used to make informed decisions in different process plants. For instance, a process in which the bulk material is expected to be uniformly supplied to a reactor in order to maintain the reactor efficiency, it is possible to

Results and discussions

estimate the conveying pipe length needed after a given bend region to achieve uniformity in material transport before getting to the reactor.

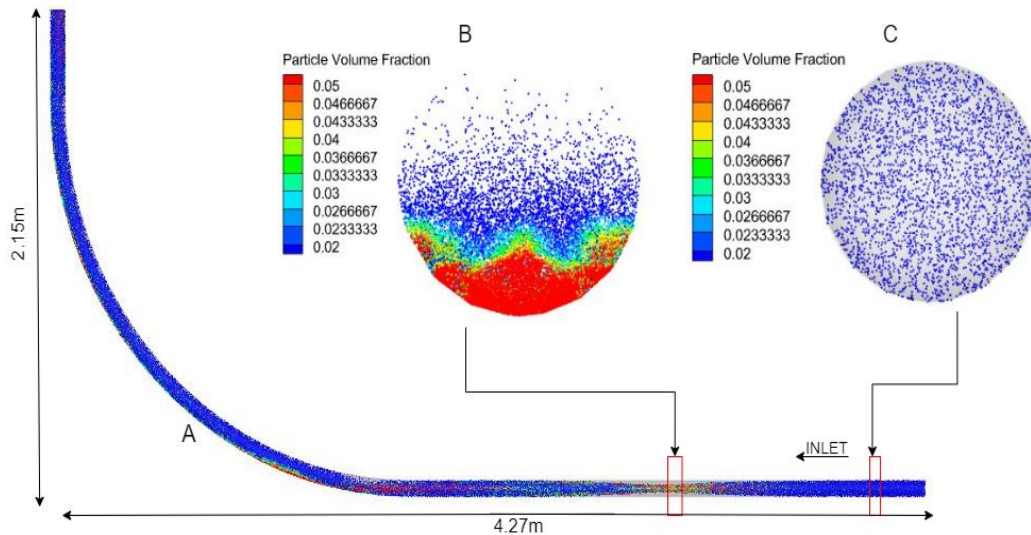


Figure 5.7: View of geometry from the top (A), cross-section at 1.2m from the inlet (B), and 0.2m (C).

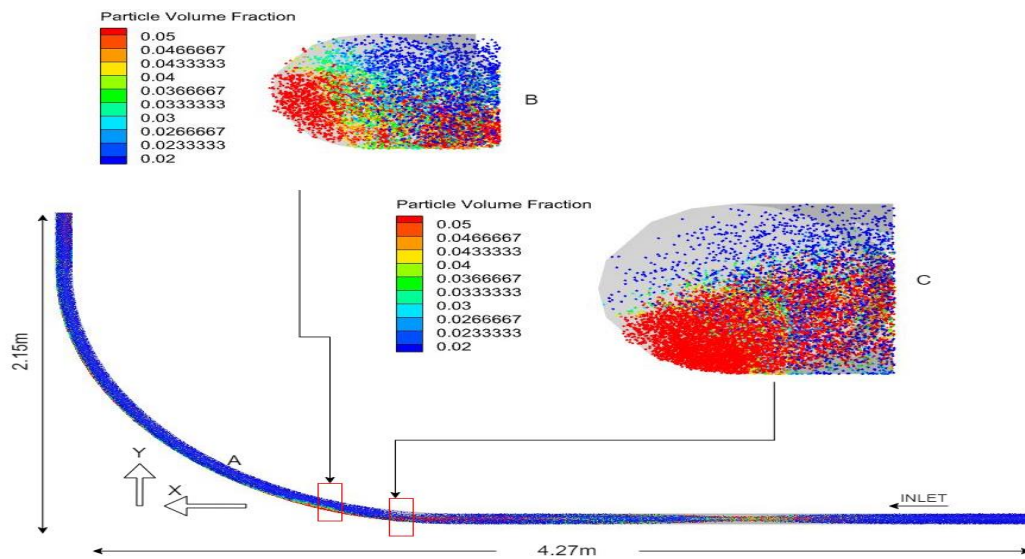


Figure 5.8: View of geometry from the top (A), cross-section around the bend at 0.22m along the y axis (B), and 2.3m from the inlet (C), and). This cross-sectional view is looking into the pipe from the inlet with particles and air going into the page.

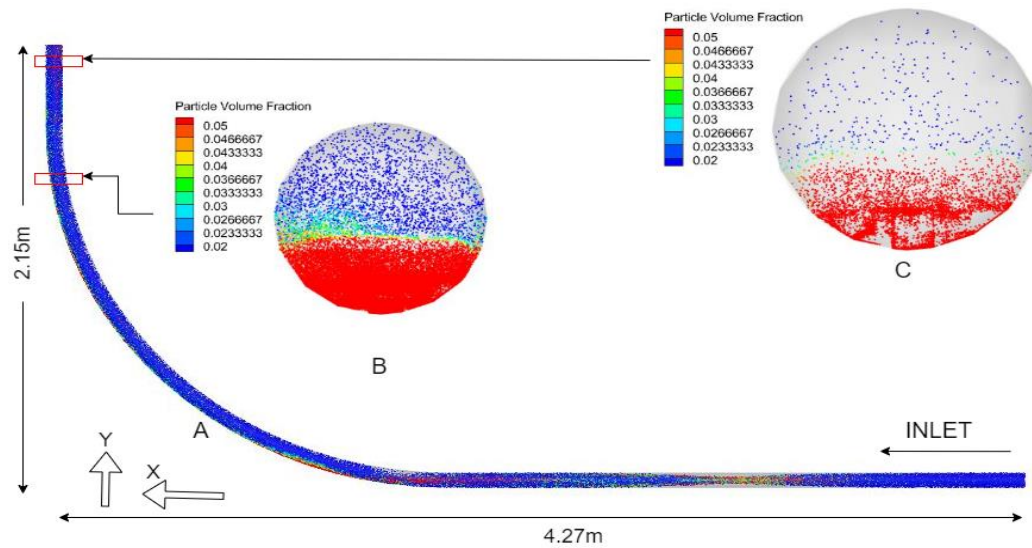


Figure 5.9: View of geometry from the top (A), cross-section at 1.85m (B), and 2.1m (C) along the y-axis.

5.4 Particle roping effect and fluid velocity distribution

Figure 5.10 shows a special phenomenon associated with the multiphase flow along a bend in a lean transport process. The roping effect as it is generally referred to can be observed. The volume fraction of particles less than 0.15 has been removed using the Barracuda blanking feature for clarity. As particles approach the bend, centrifugal forces acting in the bend cause particle stratification as they are drawn closer to the outer walls of the pipe section. The resultant effect is a higher particle concentration spreading along the outer walls in the bend. This is carried along with a distance after the bend as the particles tend to assume a narrower path leaving fewer particles to be completely suspended in the gas stream. According to Levy and Mason “A high particle concentration region in a pipe cross-section is often referred to as a rope region”[90]. Downstream of the bend, rope dispersion can be observed, a resultant effect of secondary flows causing gradual redistribution of particles around the pipe circumference and into the center.

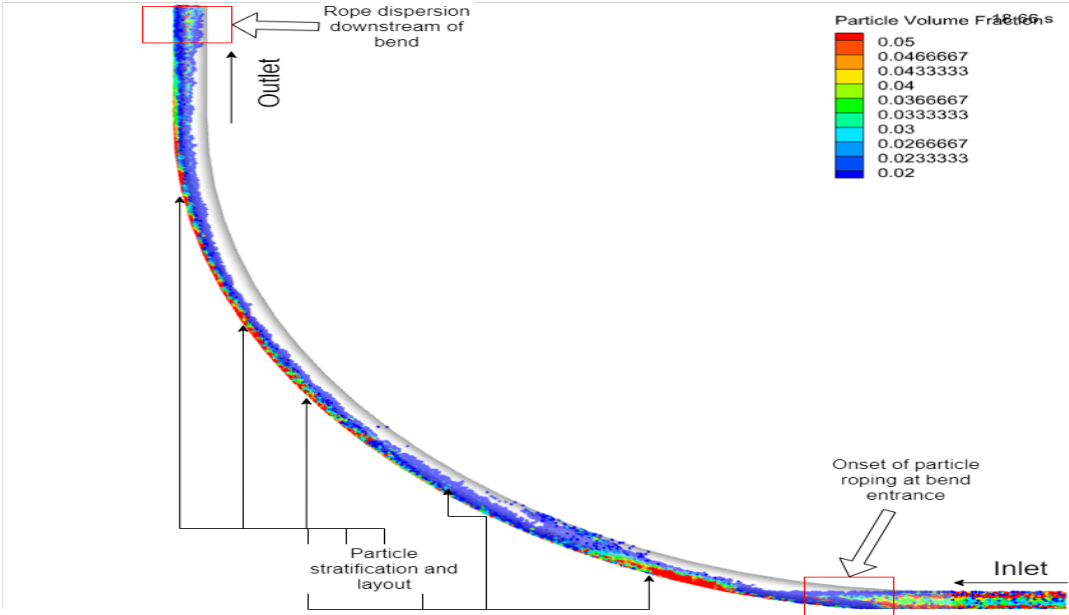


Figure 5.10: Particle roping effect due to bend at 23m/s.

In figure 5.11, the scattered and distorting nature of the velocity arrows as they approach the bend is indicative of fluid rotation, informing of the presence of vortices. Vortices that also contribute to roping are associated with the fluid phase resulting in un-uniform particle distribution and particle gathering at the outer walls of the pipe. Particle concentration below vortex regions is seen to be higher with a lower fluid velocity magnitude. Figure 5.11 B is a cross-section of the plan view at the bend entrance, looking at the fluid velocity distribution from the top of the pipe while figure 5.11 C is a zoomed view at the same location but looking at the bend area from the side along the x-axis.

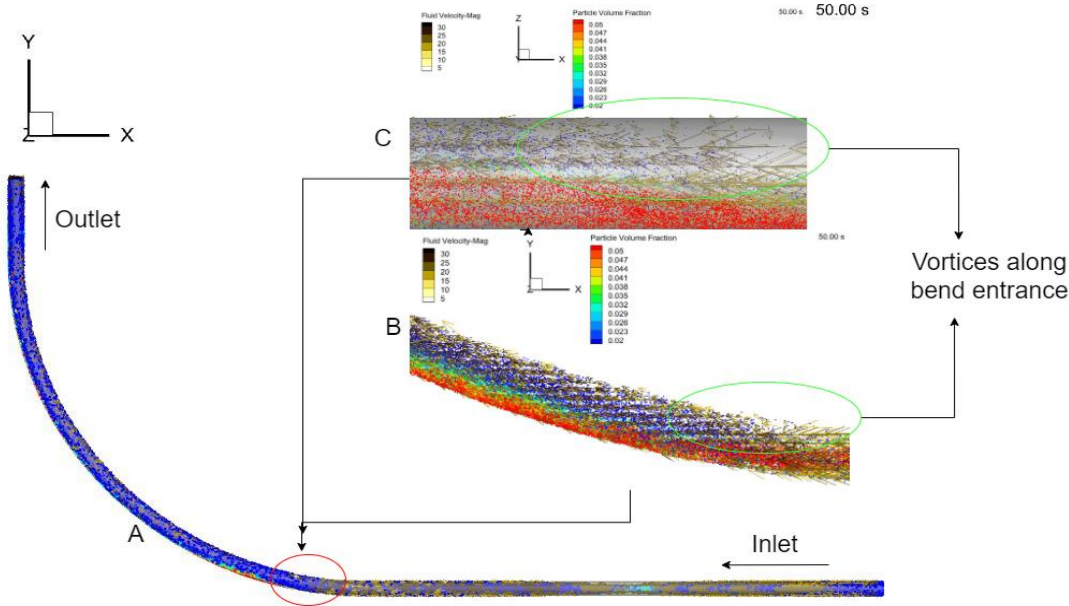


Figure 5.11: View of fluid velocity distribution and vortices formation along bend entrance. Plan view of geometry (A), vortices formation at bend entrance (B) and zoomed view of vortices region at bend entrance (C)

5.5 Wall erosion impact analysis

Particle to wall interaction is the predominant cause of wall wear during pneumatic transport and as discussed in section 2.3.4 (erosion), velocity plays a vital role in erosion intensity on pipe walls. To estimate the value of the impact intensity, data from simulations using the Barracuda software were collated by adopting the correlation given in equation 2.22, based on the experimental results taken from the pilot rig tests. As shown in figure 5.12, eight impact points were tracked along the pipe bend and impact intensity on the wall along these points at different transport velocities was plotted in figure 5.13. The velocities were in the range of 14.7m/s to 32m/s and the result shows that erosion wear on a pipe increases with an increase in velocity. For all velocity cases considered, the highest impact intensity was observed at point 2, this corresponds to a position at the bend entrance where particles tend to change flow direction. This observation was also made by Dwivedi *et al*[76] who showed in their work that erosion impact was higher at the upper walls of a C-shaped vertical CFB riser with impact intensity greatest at the exit region where particles tend to change flow direction.

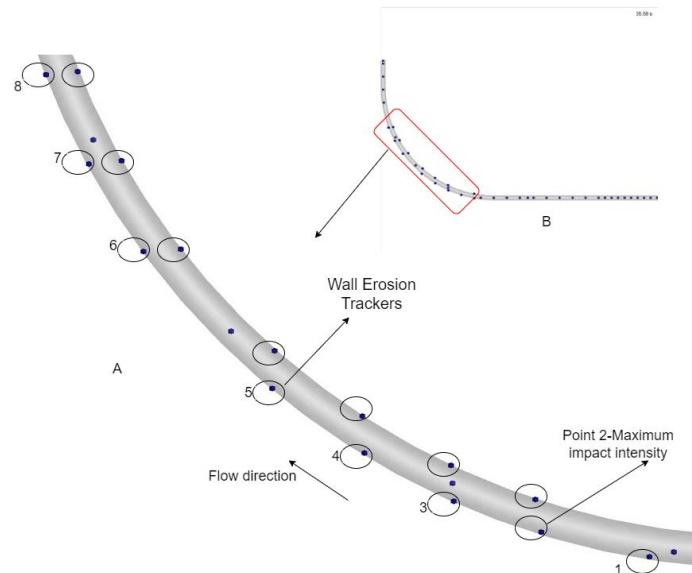


Figure 5.12: Zoomed geometry showing erosion tracking points along the pipe bend (A) and Pipe geometry showing the region of interest (B).

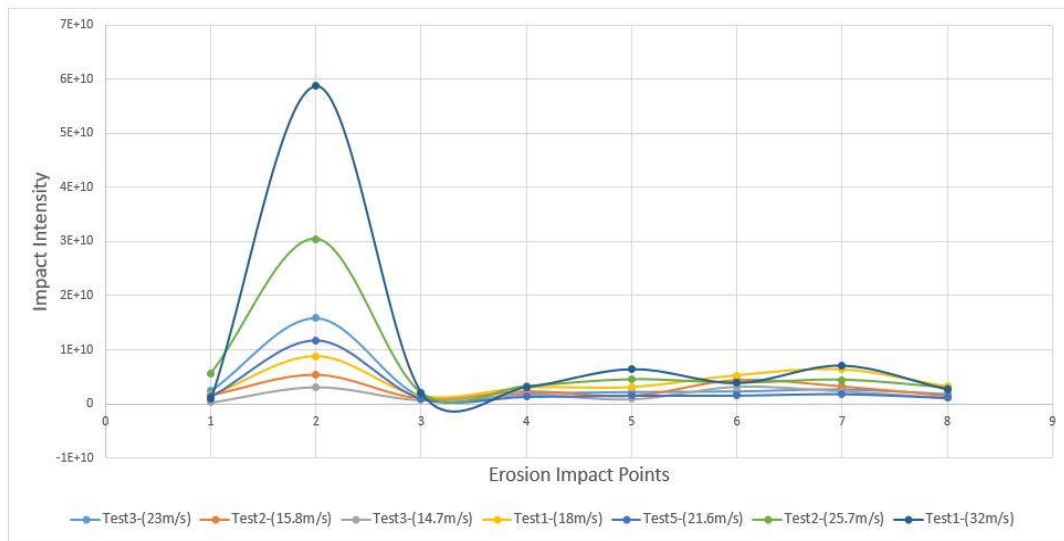


Figure 5.13: Graphical representation of impact intensity along the bend at different velocities.

Figures 5.14 and 5.15 show an isovolume view of regions of highest erosion impact during pneumatic transport of the pellets at velocities of 32m/s and 14.7m/s respectively. The impact intensity index has varying colors indicating different degrees of impact, with red, green, and blue showing areas of high, medium, and low erosion impact respectively. At 14.7m/s, low impact intensity could be observed with impact regions falling within the low and medium color ranges of blue and light green respectively. However, this was a sharp contrast from observations made at a velocity of 32m/s, high impact Index colors such as red, orange, and yellow were observed to have mostly dominated the region. One major similarity between the two velocity cases nonetheless was in predicting the fact that point 2 was the highest region prone to erosion wear. This confirms and gives credence to the initial graphical analysis made (figure 5.13).

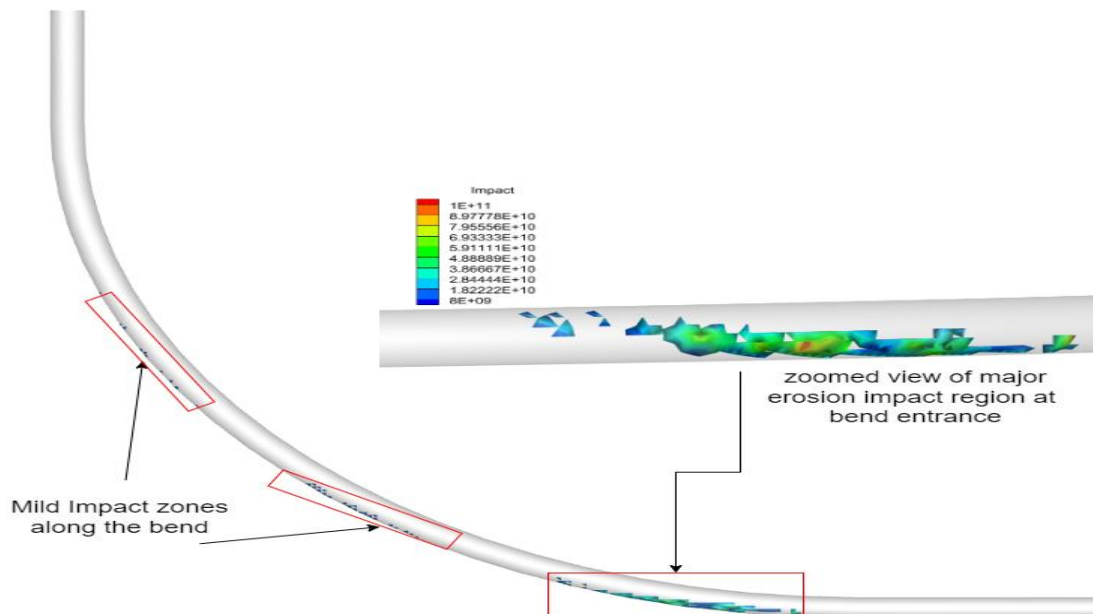


Figure 5.14: Isovolum view showing impact intensity on pipe wall along the bend at a velocity of 32m/s.

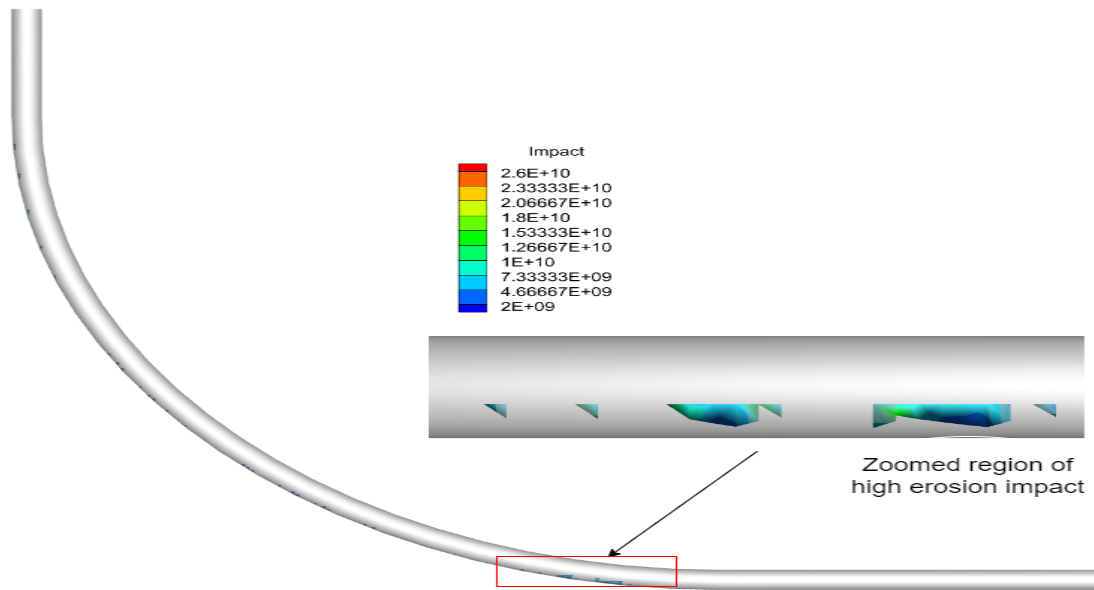


Figure 5.15: Isovolume view showing impact intensity on pipe wall along the bend at a velocity of 14.7m/s.

A graphical look into the wall wear intensity at the bend entrance is shown in figure 5.16. This graph which was taken from Tecplot360 (Barracuda post-processing software) after 50 seconds of simulations shows that at the initial time approximately within the first four seconds of simulation time, there was a continuous increase in wear intensity which was eventually followed by a decline. At the initial time, pioneer particles impacted greatly the walls of the pipe resulting in higher erosion intensity values. A good number of these particles will also experience a rebound with a change in particle direction and momentum, this bounce will impact upcoming particles leading to a reduction in effective particle velocity and hence reduced value of erosion intensity. After 20 seconds of simulation (1 day), the impact intensity assumed a relatively constant state. The erosion analysis gives an insight into the areas with the likelihood of failure along the pipe during pneumatic transport of the 1cm pellets over a period of time.

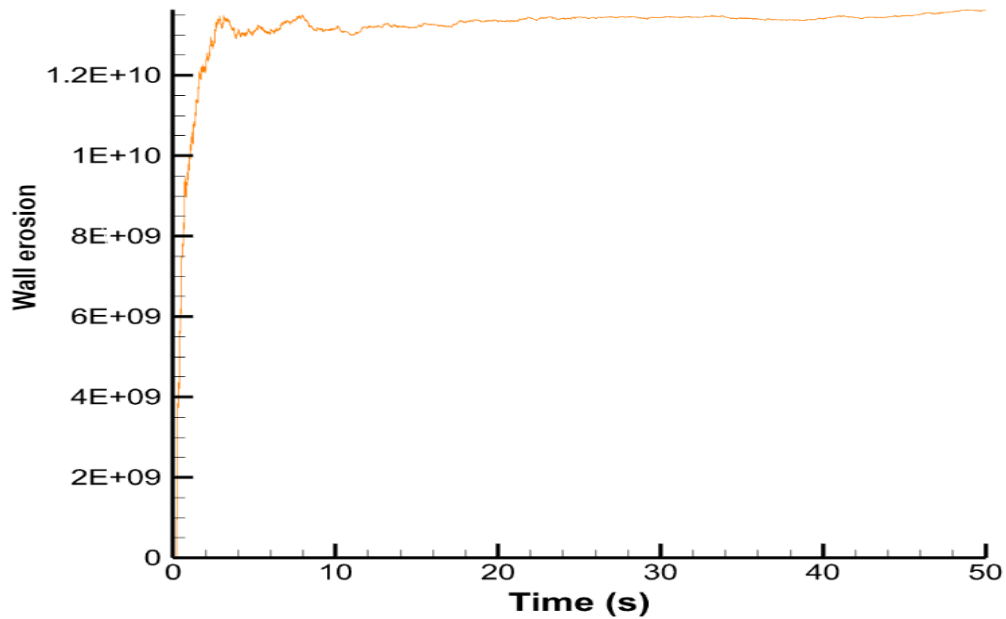


Figure 5.16: Wall erosion over time at the bend entrance at a velocity of 32m/s.

5.6 Pipe weight analysis

The weight of the pipe bend and length was initially measured, with values of 9.547kg and 2.94m respectively. 16 different erosion tests were carried out at approximately 1hr 30minutes. The bend weight after the test dropped to 9.450kg, showing a weight loss of 0.097kg (97grams) with a weight loss per pipe length of 0.033kg/m (33grams per meter). Figure 5.17 shows a bar chart of the weight variations. This loss is attributed to the scrapping effect of particles on the walls of the pipe bend during transport. Assuming close to perfect experimental conditions, with a little amount of pellet breakage and longer hours of tests, chances are high that a significant weight loss around the pipe bend could have been observed.

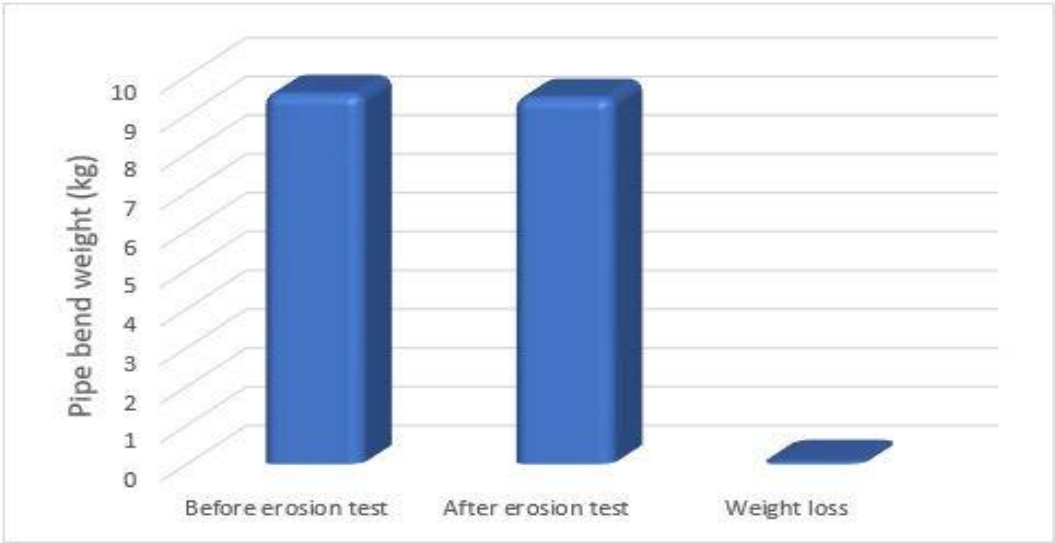


Figure 5.17: Difference in bend weight before and after the erosion tests.

5.7 Pipe thickness analysis

Figure 5.18 is a pictorial representation of the points marked on the bend and the various locations around the circumference where thickness measurements have been taken. Table 5.3 displays the measurement results obtained using the 45MG thickness gauge before the bend was coupled to the pipeline and after the tests were performed

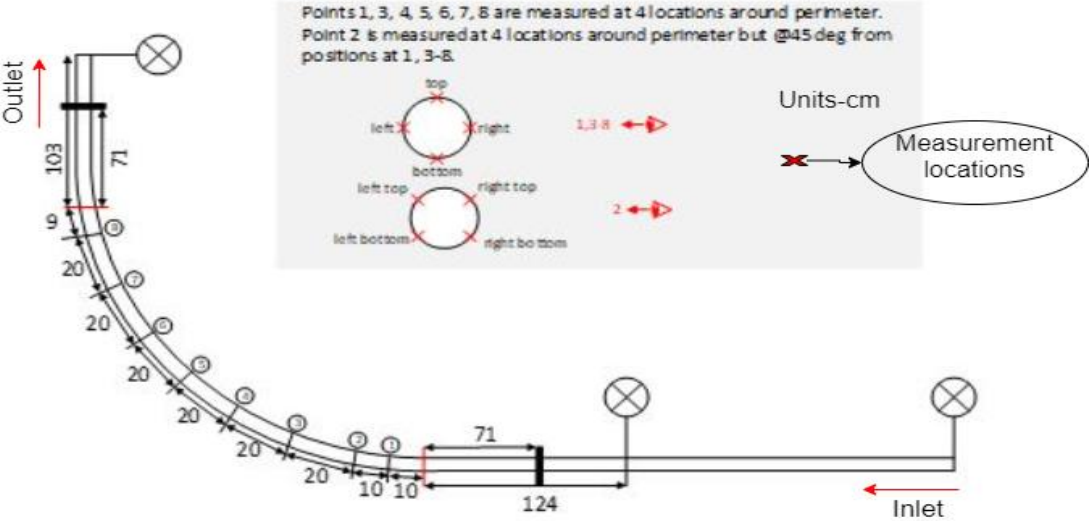


Figure 5.18: Thickness measurement points along the pipe bend.

Results and discussions

Table 5.3: Pipe thickness measurement before and after erosion tests

Unit-mm	Before Erosion Tests				After Erosion Tests			
Points	Top	Bottom	Right	Left	Top	Bottom	Right	Left
1	8.315	8.16	8.565	8.25	8.165	8.16	8.635	8.425
3	8.335	8.275	8.55	8.28	8.27	8.195	8.615	8.41
4	8.435	8.23	8.45	8.16	8.295	8.203	8.625	8.35
5	8.445	8.24	8.455	8.16	8.3	8.14	8.673	8.33
6	8.295	8.13	8.28	7.95	8.035	8.12	8.527	7.995
7	8.455	8.215	8.455	8.17	8.245	8.215	8.61	8.335
8	8.225	8.065	8.275	7.98	8.065	8.05	8.345	8.065
Unit-mm	Before Erosion Tests				After Erosion Tests			
Point	RightTop	LeftTop	RightBottom	LeftBottom	RightTop	LeftTop	RightBottom	LeftBottom
2	8.57	8.3	8.50	8.3	8.61	8.37	8.49	8.27

Figures 5.19 and 5.20 show the plot of the pipe thickness at the right and left locations along the bend respectively, before and after the erosion test. It was observed that for both cases, instead of a thickness reduction, an increase was observed, however, this wasn't significant as the variations were within the absolute accuracy of the gauge and there could have been possibilities of reduced measurement accuracy associated with the instrument due to the presence of rough surfaces around the pipe. Figures 5.21 and 5.22 show the cases for the top and bottom locations respectively. Though slight thickness reduction after the test was observed, these changes were also within the accuracy limit of the measuring gauge. It was also observed that some points, specifically 6 and 8, along the pipe showed great deviation from others and this has been attributed to non-uniformity of the pipe thickness as confirmed by the pipe manufacturers. The obtained thickness measurements did not give much insight into the erosion conditions in the pipe, however, physical observation of a cross-section of the pipe along the bend as shown in figure 5.23 shows scarring and trek lines along the internal walls suggesting particle physical impacts on the wall surface during transport.

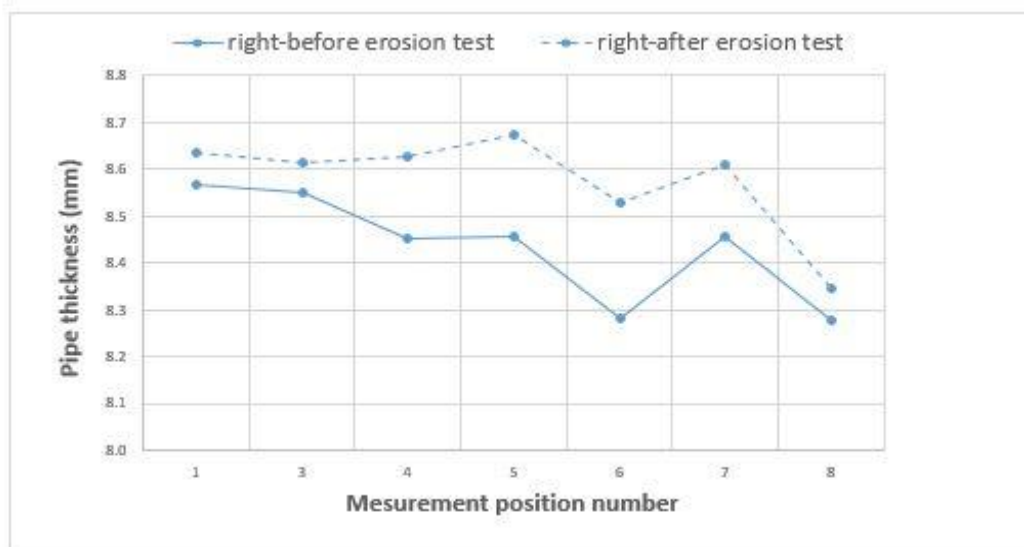


Figure 5.19: Pipe thickness comparison at the right locations along the bend.

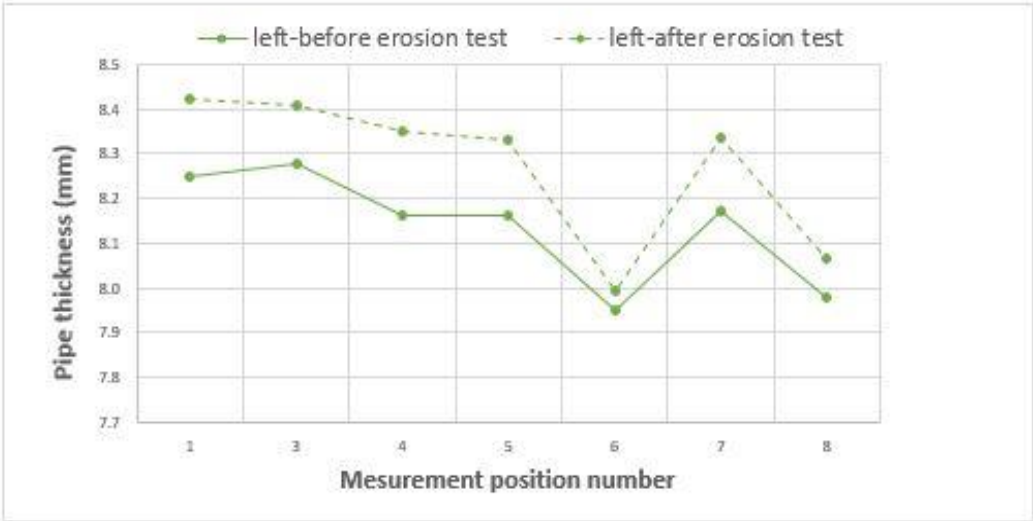


Figure 5.20: Pipe thickness comparison at the left locations along the bend.

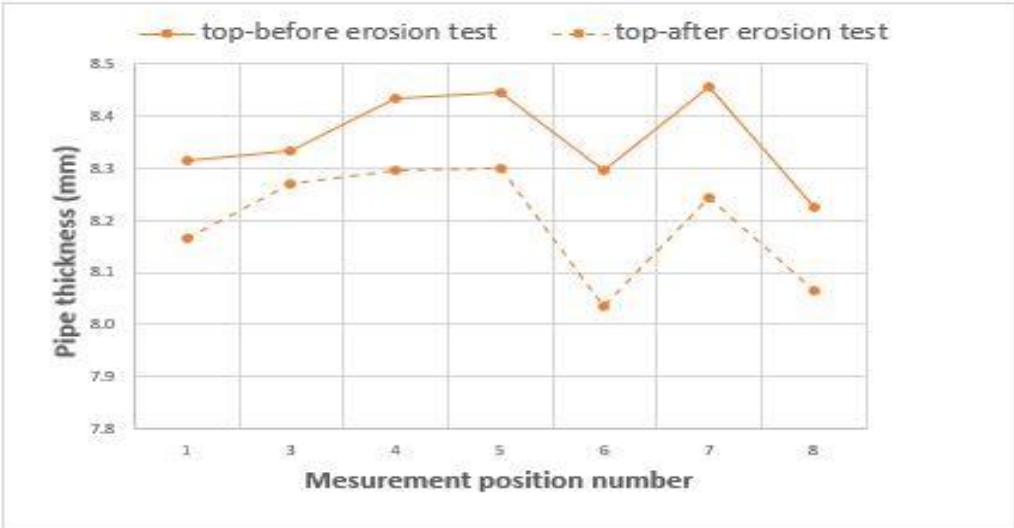


Figure 5.21: Pipe thickness comparison at the top locations along the bend.

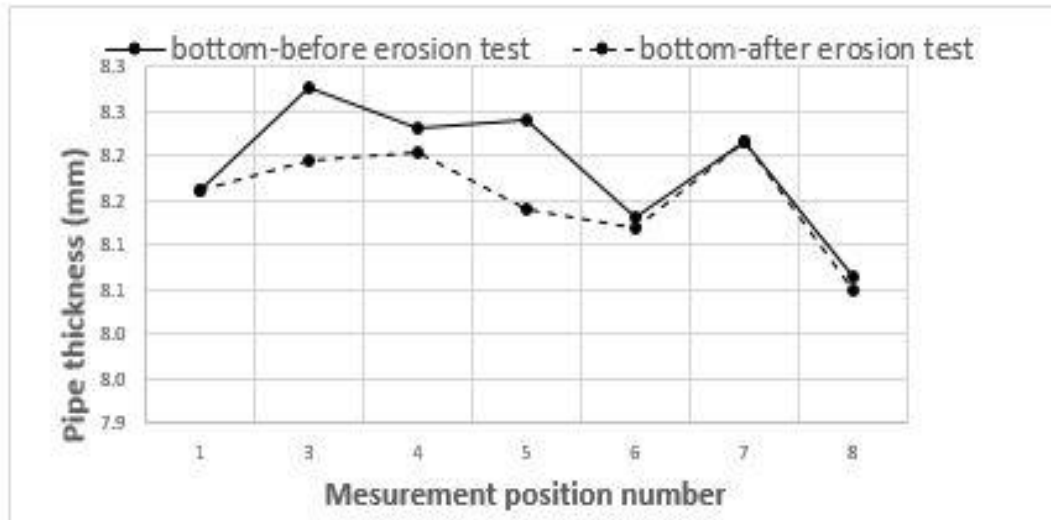


Figure 5.22: Pipe thickness comparison at the bottom locations along the bend.



Figure 5.23: Internal view of the cleaned bend cross-section after erosion test.

5.8 Optimization analysis

5.8.1 Effect of pellet size on maximum erosion intensity

Particle size can affect erosion impact intensity on pipe walls during pneumatic transport. Simulations were carried out at two different particle diameters at a velocity of 32m/s using the Wen-Yun/Ergun model with figure 5.24 displaying the results. It was observed that the maximum erosion impact remained at point 2 as earlier indicated (figure 5.14) but was reduced by approximately 27.4% for a pellet diameter of 0.5cm when compared to the 1cm diameter

Results and discussions

pellet. For high-velocity pellet transport, adopting a smaller pellet diameter was observed to reduce the erosion impact effect on the pipe walls. Also, works of literature have shown that particle shape considerations are vital during pneumatic transport as sharply shaped particles will trigger greater wall erosion scarring, unlike rounded particles which tend to exhibit lesser impact intensity on pipe walls.

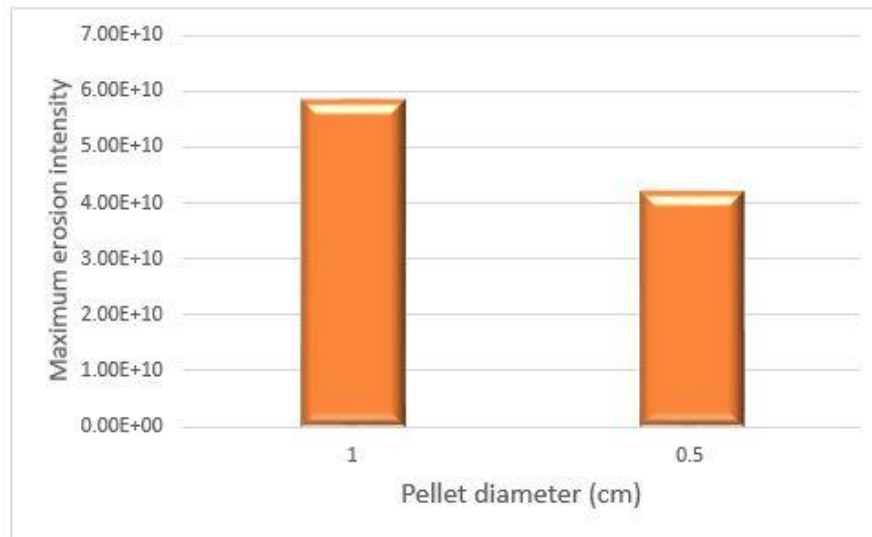


Figure 5.24: Maximum erosion intensity at different pellet diameters at a velocity of 32m/s.

5.8.2 Effect of geometry change on maximum erosion intensity

The pneumatic transport system can also be optimized by modifying the pipe geometry with a focus on reducing maximum erosion impact at the bend. Figure 5.25 is a schematic presentation of the modified geometry, while Figure 5.26 shows the maximum impact intensity on the pipe bend using two different pipe diameters. The pipe diameter was increased to twice the initial size, from 7.4cm (D1 representing the base geometry) to 14.8cm (D2 representing the modified geometry). It was observed that the maximum erosion impact along the bend was reduced by 94.6% of the initial value. This would result in a longer life span of the pipe, however, it will mean extra cost of pipe procurement and space requirements for pipe layout around the facility. Depending on the industrial setup and operating conditions, a trade-off analysis becomes necessary to ascertain which system offers the best economic advantage. The WenYun-Ergun model was adopted at a velocity of 32m/s and a solid loading ratio of 3.24 for both cases.

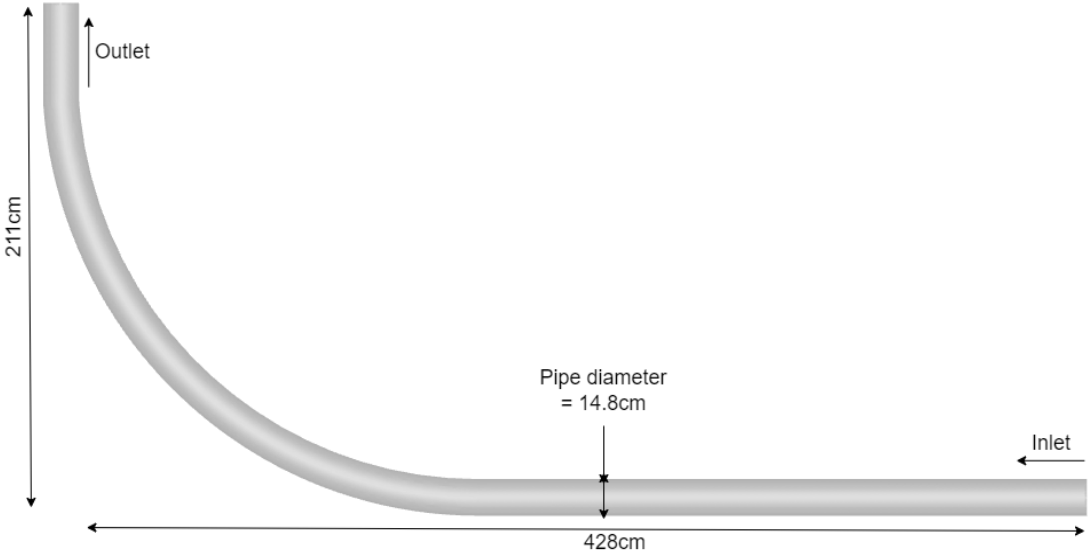


Figure 5.25: Schematic view of the modified geometry.

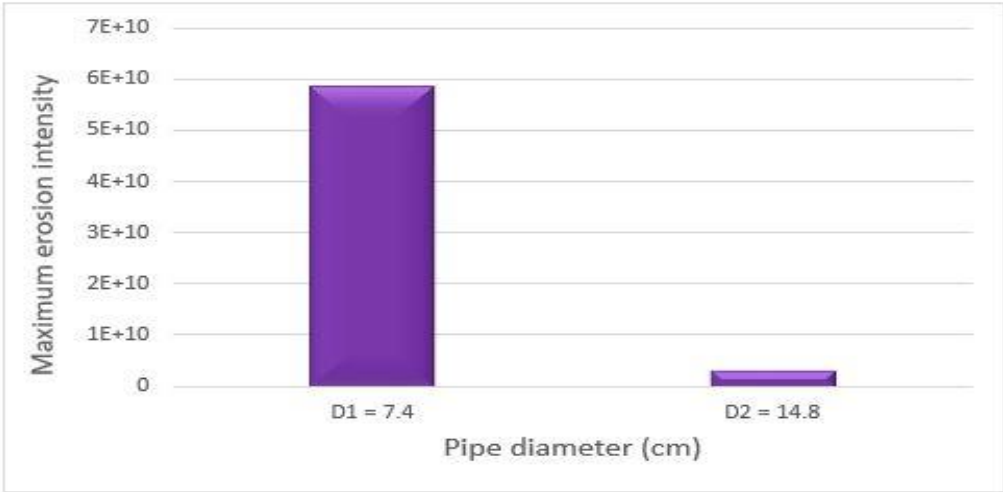


Figure 5.26: Maximum erosion intensity at different pipe diameters at a velocity of 32m/s.

6 Challenges

Simulation results presented in chapter 5 show promises for the developed model, however, an acceptable validation may be difficult at this point due to varying factors under which the experiment has been carried out. As much as there are some drawbacks in the pilot rig used for the experimental work, the pipe simulation area could have been adjusted. The simulation focus was on one bend section out of the entire bends that comprise the pipeline and there was only one pressure transducer that could be validated between the bend entry and exit points. The other 2 transducers happen to be the flow (inlet) and the pressure (outlet) boundary conditions defined during the simulations. Simulating the entire pipeline could have been a possibility, however, at this stage, the computational cost and time would have been too high for this study. Furthermore, as shown in appendix B, the pellets were observed to undergo significant change during transport. This pellet breakage and formation of oily deposits around the pipe may have led to inconsistent pellet flow behaviors during the transport as well as pressure variations at some pressure tapping points in the pipeline. As stated by the manufacturer, the pressure transducers were designed for completely dry conditions and pressure readings could have been affected by this.

7 Conclusion

In this study, a CPFDF model-based technique was adopted in the optimization of the feed pellet transfer system in fish farms. This was used to investigate pressure drop along the pipe and erosion impact on the pipe wall.

The model was tested against different drag models and the Wen-Yu and Ergun model represented velocities above 20m/s well while for lower velocity cases, the Ergun model gave satisfactory results. The velocities were in the range of 14.7m/s to 32m/s, at a solid loading ratio of 5.42 to 3.24. The model was successful in predicting the pressure values at transducer points from the experimental data and subsequently, pressure drops along the pipeline during conveying. The hydrodynamics of the transport system was predicted by the model and transport phenomenon such as particle roping and vortex formation were observed around the bend region

Results from this study show that an increase in conveying velocity has a direct impact on pipe wear and pellet breakage, simulation results predicted that the highest impact on the pipe wall was at the bend entry position where particles change flow direction, while conducted experiments showed an increase in pellet attrition (breakage) and the formation of oily deposits in the pipe walls at high transport velocities.

When the pellet size was changed from 1cm to 0.5 cm, there was a 27.4% reduction in maximum erosion impact intensity on the pipe walls around the bend when compared to the 1cm pellet at a velocity of 32 m/s and a solid loading ratio of 3.24, similarly, an increment in the pipe diameter from 7.4cm to 14.8cm for the 1cm pellet resulted in a 94.6% decrease in the maximum erosion impact at the same velocity (32m/s) and solid loading fraction (3.24).

From the results presented in this study and the challenges discussed, it can be concluded that there are high possibilities that CPFDF using Barracuda VR[®] can be used to predict the hydrodynamics of the 1cm Geldart D pellets. The developed model in this work can act as a reference upon which further work can be carried out to design and validate models that can be adopted for pneumatic process simulations and optimization of feed pellet conveying systems in the fish farming sector.

8 Further work

This study has shown that there is room for further research to be carried out under more favorable conditions and this can still be achieved. Suggested modification possibilities in the pilot rig setup would include adding more pressure transducers or tapping points between the inlet and outlet of the bend under investigation. Furthermore, a closed-circuit pneumatic transport system was used without a provision for physical observation of what was happening inside the pipe during transport, the pipe could be made transparent or modified to include an observation window to allow visual inspection of the transport process. This will lead to an early observation of any change in the physical shape of the pellets. The 45MG Olympus gauge was used to measure pipe thickness along the bend before and after the erosion tests, however, more sophisticated technology could also be adopted in future works. This will enable a more automated pipe-wall thickness measurement process with data collation and analysis carried out in real-time during pellet transport. A positive effect will be a reduction or complete elimination of possible human error in the measurement process. Also, high-speed cameras and sensors could be adopted to capture real-time pictorial views of wall impact by particles and local velocities around the bend respectively. This will result in the possibility of observing effects such as vortex formation and roping at the bend region as described in chapter 5. Finally, simulating different bend radii as a means to optimize the conveying system is highly recommended as this was not carried out due to time constraints. In all, the fact remains that, if a full industrial setup and sufficient resources are available, there is more that can be achieved.

References

- [1] “Aquaculture: Types, Benefits and Importance (Fish Farming) - Conserve Energy Future,” Feb. 18, 2018. <https://www.conserve-energy-future.com/aquaculture-types-benefits-importance.php> (accessed Feb. 22, 2022).
- [2] A. Gjuka, “Dynamic Analysis of Feed Pipes for Fish Farming in Open Sea.” University of Stavanger, Norway, 2017. Accessed: Feb. 21, 2022. [Online]. Available: <http://hdl.handle.net/11250/2460089>
- [3] C. Carter, *The Politics of Aquaculture: Sustainability Interdependence, Territory and Regulation in Fish Farming*, 1st edition. London ; New York: Routledge, 2018.
- [4] M. Føre *et al.*, “Precision fish farming: A new framework to improve production in aquaculture,” 2017, doi: <https://doi.org/10.1016/j.biosystemseng.2017.10.014>.
- [5] FAO, *The State of World Fisheries and Aquaculture 2018: Meeting the sustainable development goals*. Rome, Italy: FAO, 2018. Accessed: Feb. 22, 2022. [Online]. Available: <https://www.fao.org/documents/card/en/c/I9540EN/>
- [6] FAO, *The State of World Fisheries and Aquaculture 2020: Sustainability in action*. Rome, Italy: FAO, 2020. doi: 10.4060/ca9229en.
- [7] “Rabobank: Norway, China to lead the progress of offshore aquaculture.” <https://www.seafoodsource.com/news/aquaculture/rabobank-norway-china-to-lead-the-progress-of-offshore-aquaculture> (accessed Feb. 22, 2022).
- [8] “Record high Norwegian seafood exports in 2021.” <https://en.seafood.no/news-and-media/news-archive/record-high-norwegian-seafood-exports-in-2021/> (accessed Feb. 23, 2022).
- [9] I. El-Thalji, “Context analysis of Offshore Fish Farming,” *IOP Conf. Ser. Mater. Sci. Eng.*, vol. 700, no. 1, p. 012065, Nov. 2019, doi: 10.1088/1757-899X/700/1/012065.
- [10] A. Iversen, F. Asche, Ø. Hermansen, and R. Nystøyl, “Production cost and competitiveness in major salmon farming countries 2003–2018,” *Aquaculture*, vol. 522, p. 735089, May 2020, doi: 10.1016/j.aquaculture.2020.735089.
- [11] T. F. Sutherland, C. L. Amos, C. Ridley, I. G. Droppo, and S. A. Petersen, “The Settling Behavior and Benthic Transport of Fish Feed Pellets under Steady Flows,” *Estuaries Coasts*, vol. 29, no. 5, pp. 810–819, 2006, doi: 10.1007/BF02786532.
- [12] “A global leader in aquafeed,” *Skretting*. <https://www.skretting.com/en/> (accessed May 16, 2022).
- [13] “Image Gallery AKVA group Aquaculture.” <https://www.akvagroup.com/news/image-gallery> (accessed Feb. 22, 2022).
- [14] “Eidsvaag Pioner - IMO 9660449 - ShipSpotting.com - Ship Photos and Ship Tracker.” <http://www.shipspotting.com/gallery/photo.php?lid=2831524#> (accessed Feb. 22, 2022).
- [15] “Aquaculture Engineering by Lekang, Odd-Ivar. 9780470670859. Innbundet - 2013 | Akademika.no.” <https://www.akademika.no/aquaculture-engineering/lekang-odd-ivar/9780470670859> (accessed Feb. 22, 2022).

References

- [16] “Chapter 10 - Marine Installations,” p. 37.
- [17] A. Levy, H. Kalman, and C. J. Kalman, *Handbook of Conveying and Handling of Particulate Solids*. Oxford, NETHERLANDS, THE: Elsevier Science & Technology, 2001. Accessed: May 17, 2022. [Online]. Available: <http://ebookcentral.proquest.com/lib/ucsn-ebooks/detail.action?docID=318346>
- [18] KAHE, *Transportation of Solids | Online Lecture Series 8 | Mechanical Operations in Chemical Engineering*, (May 06, 2021). Accessed: Mar. 08, 2022. [Online Video]. Available: <https://www.youtube.com/watch?v=j5tvsTI9WFY>
- [19] S. Kuang, M. Zhou, and A. Yu, “CFD-DEM modelling and simulation of pneumatic conveying: A review,” *Powder Technol.*, vol. 365, pp. 186–207, 2020, doi: 10.1016/j.powtec.2019.02.011.
- [20] R. and Markets, “Global Pneumatic Conveying System Market (2022 to 2027) - Industry Trends, Share, Size, Growth, Opportunity and Forecasts,” *GlobeNewswire News Room*, Feb. 24, 2022. <https://www.globenewswire.com/news-release/2022/02/24/2391434/28124/en/Global-Pneumatic-Conveying-System-Market-2022-to-2027-Industry-Trends-Share-Size-Growth-Opportunity-and-Forecasts.html> (accessed Feb. 24, 2022).
- [21] C. G. Toomey, “Pneumatic Conveying System Optimization,” *IEEE Trans. Ind. Appl.*, vol. 50, no. 6, pp. 4319–4322, 2014, doi: 10.1109/TIA.2014.2346695.
- [22] M. Rhodes, *Introduction to Particle Technology*, 2. Aufl. Chichester: Wiley, 2013.
- [23] H. PURUTYAN, T. G. TROXEL, and F. CABREJOS, “Propel your pneumatic conveying system to higher efficiency,” *Chem. Eng. Prog.*, vol. 97, no. 4, pp. 42–55, 2001.
- [24] C. Ratnayake, *A comprehensive scaling up technique for pneumatic transport systems*. Fakultet for ingeniørvitenskap og teknologi, 2005. Accessed: Feb. 28, 2022. [Online]. Available: <https://ntnuopen.ntnu.no/ntnu-xmlui/handle/11250/227951>
- [25] D. Mills, “Chapter 2 - Review of pneumatic conveying systems,” in *Pneumatic Conveying Design Guide (Second Edition)*, D. Mills, Ed. Oxford: Butterworth-Heinemann, 2004, pp. 29–53. doi: 10.1016/B978-075065471-5/50002-2.
- [26] R. Pan, “Material properties and flow modes in pneumatic conveying,” *Powder Technol.*, vol. 104, no. 2, pp. 157–163, Sep. 1999, doi: 10.1016/S0032-5910(99)00044-3.
- [27] M. Ryu, D. S. Jeon, and Y. Kim, “Prediction and improvement of the solid particles transfer rate for the bulk handling system design of offshore drilling vessels,” *Int. J. Nav. Archit. Ocean Eng.*, vol. 7, no. 6, pp. 964–978, Nov. 2015, doi: 10.1515/ijnaoe-2015-0067.
- [28] G. E. Klinzing, “Pneumatic conveying: transport solutions, pitfalls, and measurements,” in *Handbook of Powder Technology*, vol. 10, Elsevier B.V, 2001, pp. 291–301. doi: 10.1016/S0167-3785(01)80031-2.
- [29] gustavegunawan, “PNEUMATIC CONVEYING SYSTEM,” *gustavegunawan*, Apr. 25, 2013. <https://gustavegunawan.wordpress.com/2013/04/25/pneumatic-conveying-system/> (accessed Feb. 28, 2022).

References

- [30] “1 - David Mills - Pneumatic Conveying Design Guide, Second Edition (2004) | PDF | Fluid Dynamics | Pipeline Transport,” *Scribd*.
<https://www.scribd.com/document/537813704/1-David-Mills-Pneumatic-Conveying-Design-Guide-Second-Edition-2004-libgen-lc> (accessed Feb. 12, 2022).
- [31] D. Mills, “Chapter 3 - A Review of Pneumatic Conveying Systems,” in *Pneumatic Conveying Design Guide (Third Edition)*, D. Mills, Ed. Butterworth-Heinemann, 2016, pp. 59–80. doi: 10.1016/B978-0-08-100649-8.00003-2.
- [32] A. T. Agarwal and S. V. Dhodapkar, “Debottleneck pneumatic conveying systems: respect your system’s operational window, and open the door to improved capacity,” *Chem. Eng.*, vol. 111, no. 4, pp. 38–45, Apr. 2004.
- [33] Multiphase Flows IITG, *Lecture 6: Pneumatic Conveying*, (Feb. 11, 2018). Accessed: Feb. 28, 2022. [Online Video]. Available:
<https://www.youtube.com/watch?v=0plj41Y2qIM>
- [34] S. Vashisth and J. R. Grace, “Simulation of Granular Transport of Geldart Type-A, -B, and -D Particles through a 90° Elbow,” *Ind. Eng. Chem. Res.*, vol. 51, no. 4, pp. 2030–2047, Feb. 2012, doi: 10.1021/ie200647e.
- [35] G. P. Tilly, “Erosion Caused by Impact of Solid Particles,” in *Treatise on Materials Science & Technology*, vol. 13, D. Scott, Ed. Elsevier, 1979, pp. 287–319. doi: 10.1016/S0161-9160(13)70071-1.
- [36] D. Mills, M. G. Jones, and V. K. Agarwal, *Handbook of Pneumatic Conveying Engineering*. Boca Raton: CRC Press, 2004. doi: 10.1201/9780203021989.
- [37] Y. I. OKA and T. YOSHIDA, “Practical estimation of erosion damage caused by solid particle impact. Part 2: Mechanical properties of materials directly associated with erosion damage,” *Wear*, vol. 259, no. 1, pp. 102–109, 2005.
- [38] M. Droubi, R. Tebowei, S. Islam, Md. F. Hossain, and E. Mitchell, “Computational Fluid Dynamic Analysis of Sand Erosion in 90 Degree Sharp Bend Geometry,” Jul. 2016.
- [39] D. Mills, “Chapter 28 - Particle Degradation,” in *Pneumatic Conveying Design Guide (Third Edition)*, D. Mills, Ed. Butterworth-Heinemann, 2016, pp. 643–663. doi: 10.1016/B978-0-08-100649-8.00028-7.
- [40] J. Werther and J. Reppenhagen, “7 - Attrition in Fluidized Beds and Pneumatic Conveying Lines,” in *Fluidization, Solids Handling, and Processing*, W.-C. Yang, Ed. Westwood, NJ: William Andrew Publishing, 1999, pp. 435–491. doi: 10.1016/B978-081551427-5.50009-0.
- [41] T. Brosh, H. Kalman, and A. Levy, “DEM simulation of particle attrition in dilute-phase pneumatic conveying,” *Granul. Matter*, vol. 13, no. 2, pp. 175–181, 2010, doi: 10.1007/s10035-010-0201-z.
- [42] K. A. Aarseth, “Attrition of Feed Pellets during Pneumatic Conveying: the Influence of Velocity and Bend Radius,” *Biosyst. Eng.*, vol. 89, no. 2, pp. 197–213, 2004, doi: 10.1016/j.biosystemseng.2004.06.008.
- [43] H. KALMAN, “Attrition of powders and granules at various bends during pneumatic conveying: Pneumatic & hydraulic conveying systems II,” *Powder Technol.*, vol. 112, no. 3, pp. 244–250, 2000.

References

- [44] Y. Zhang and C.-H. Wang, "Particle Attrition Due to Rotary Valve Feeder in a Pneumatic Conveying System: Electrostatics and Mechanical Characteristics," *Can. J. Chem. Eng.*, vol. 84, no. 6, pp. 663–679, 2006, doi: 10.1002/cjce.5450840605.
- [45] J. Wei, H. Zhang, Y. Wang, Z. Wen, B. Yao, and J. Dong, "The gas-solid flow characteristics of cyclones," *Powder Technol.*, vol. 308, pp. 178–192, 2017, doi: 10.1016/j.powtec.2016.11.044.
- [46] J. Jägers, M. Brömmmer, E. Illana, S. Wirtz, and V. Scherer, "DEM-CFD simulation of wood pellet degradation by particle-wall impact during pneumatic conveying," *Powder Technol.*, vol. 391, pp. 385–402, Oct. 2021, doi: 10.1016/j.powtec.2021.06.037.
- [47] R. Cocco, S. Karri, Y. Arrington, R. Hays, J. Findlay, and T. Knowlton, "PARTICLE ATTRITION MEASUREMENTS USING A JET CUP," Jan. 2011.
- [48] H. K. Versteeg, *An introduction to computational fluid dynamics: the finite volume method*, 2nd ed. Harlow: Pearson/Prentice Hall, 2007.
- [49] J. Bandara, *Simulation and parameter optimization of fluidized-bed and biomass gasification*. University of South-Eastern Norway, 2021. Accessed: Feb. 14, 2022. [Online]. Available: <https://openarchive.usn.no/usn-xmlui/handle/11250/2738320>
- [50] J. Parker, K. LaMarche, W. Chen, K. Williams, H. Stamato, and S. Thibault, "CFD simulations for prediction of scaling effects in pharmaceutical fluidized bed processors at three scales," *Powder Technol.*, vol. 235, pp. 115–120, Oct. 2011, doi: 10.1016/j.powtec.2012.09.021.
- [51] X. Chen and J. Wang, "A comparison of two-fluid model, dense discrete particle model and CFD-DEM method for modeling impinging gas–solid flows," *Powder Technol.*, vol. 254, pp. 94–102, Mar. 2014, doi: 10.1016/j.powtec.2013.12.056.
- [52] W. H. Ariyaratne, C. Ratnayake, and M. C. Melaaen, "Application of the MP-PIC method for predicting pneumatic conveying characteristics of dilute phase flows," *Powder Technol.*, vol. 310, pp. 318–328, 2017, doi: 10.1016/j.powtec.2017.01.048.
- [53] W. K. Ariyaratne, E. V. P. J. Manjula, C. Ratnayake, and M. Melaaen, "CFD Approaches for Modeling Gas-Solids Multiphase Flows – A Review," Sep. 2016. doi: 10.3384/ecp17142680.
- [54] Z. Zhang, L. Zhou, and R. Agarwal, "Transient Simulations of Spouted Fluidized Bed for Coal-Direct Chemical Looping Combustion," *Energy Fuels*, vol. 28, no. 2, pp. 1548–1560, 2014, doi: 10.1021/ef402521x.
- [55] A. Abbasi, P. E. Ege, and H. I. de Lasa, "CPFD simulation of a fast fluidized bed steam coal gasifier feeding section," *Chem. Eng. J.*, vol. 174, no. 1, pp. 341–350, Oct. 2011, doi: 10.1016/j.cej.2011.07.085.
- [56] Fluid Mechanics 101, [CFD] *Eulerian Multi-Phase Modelling*, (May 30, 2019). Accessed: Mar. 09, 2022. [Online Video]. Available: <https://www.youtube.com/watch?v=6BJauDTpCmo>
- [57] Fluid Mechanics 101, [CFD] *Lagrangian Particle Tracking*, (Apr. 24, 2020). Accessed: Mar. 09, 2022. [Online Video]. Available: <https://www.youtube.com/watch?v=jdq6puyvQ7E>

References

- [58] NPTEL-NOC IITM, *Lagrangian and Eulerian Descriptions - Part 1*, (Jul. 31, 2019). Accessed: Mar. 09, 2022. [Online Video]. Available: <https://www.youtube.com/watch?v=dot38AypM9I>
- [59] D. M. Snider, “An Incompressible Three-Dimensional Multiphase Particle-in-Cell Model for Dense Particle Flows,” *J. Comput. Phys.*, vol. 170, no. 2, pp. 523–549, 2001, doi: 10.1006/jcph.2001.6747.
- [60] Q. Wang *et al.*, “Application of CPFD method in the simulation of a circulating fluidized bed with a loop seal, part I—Determination of modeling parameters,” *Powder Technol.*, vol. 253, pp. 814–821, 2014, doi: 10.1016/j.powtec.2013.11.041.
- [61] S. Karimipour and T. Pugsley, “Application of the particle in cell approach for the simulation of bubbling fluidized beds of Geldart A particles,” *Powder Technol.*, vol. 220, pp. 63–69, Apr. 2012, doi: 10.1016/j.powtec.2011.09.026.
- [62] Y. Liang, Y. Zhang, T. Li, and C. Lu, “A critical validation study on CPFD model in simulating gas–solid bubbling fluidized beds,” *Powder Technol.*, vol. 263, pp. 121–134, Sep. 2014, doi: 10.1016/j.powtec.2014.05.003.
- [63] Y. Zhang, X. Lan, and J. Gao, “Modeling of gas-solid flow in a CFB riser based on computational particle fluid dynamics,” *Pet. Sci.*, vol. 9, no. 4, pp. 535–543, 2012, doi: 10.1007/s12182-012-0240-7.
- [64] V. Verma and J. T. Padding, “A novel approach to MP-PIC: Continuum particle model for dense particle flows in fluidized beds,” *Chem. Eng. Sci. X*, vol. 6, pp. 100053–, 2020, doi: 10.1016/j.cesx.2019.100053.
- [65] F. A. Williams, *Combustion Theory*, 2nd edition. Cambridge, Mass: CRC Press, 1985.
- [66] Z. Barahmand, C. Jayarathna, and C. Ratnayake, “CPFD Simulations on a Chlorination Fluidized Bed Reactor for Aluminum Production: An Optimization Study,” Sep. 2021.
- [67] W. Du, X. Bao, J. Xu, and W. Wei, “Computational fluid dynamics (CFD) modeling of spouted bed: Assessment of drag coefficient correlations,” *Chem. Eng. Sci.*, vol. 61, no. 5, pp. 1401–1420, Mar. 2006, doi: 10.1016/j.ces.2005.08.013.
- [68] D. Wang and L. Fan, “Particle Characterization and Behavior Relevant to Fluidized Bed Combustion and Gasification Systems.” pp. 42–76, 2013.
- [69] P. Wypych, “Design Considerations of Long-Distance Pneumatic Transport and Pipe Branching,” 1998, pp. 712–772. doi: 10.1016/B978-081551427-5.50013-2.
- [70] L. Mazzei and P. Lettieri, “CFD simulations of expanding/contracting homogeneous fluidized beds and their transition to bubbling,” *Chem. Eng. Sci.*, vol. 63, no. 24, pp. 5831–5847, Dec. 2008, doi: 10.1016/j.ces.2008.08.029.
- [71] R. Beetstra, M. A. van der Hoef, and J. a. M. Kuipers, “Drag force of intermediate Reynolds number flow past mono- and bidisperse arrays of spheres,” *AIChE J.*, vol. 53, no. 2, pp. 489–501, 2007, doi: 10.1002/aic.11065.
- [72] D. Gidaspow, *Multiphase flow and fluidization: continuum and kinetic theory descriptions*. Boston: Academic Press, 1994.

References

- [73] A. Haider and O. Levenspiel, “Drag coefficient and terminal velocity of spherical and nonspherical particles,” *Powder Technol.*, vol. 58, no. 1, pp. 63–70, May 1989, doi: 10.1016/0032-5910(89)80008-7.
- [74] J. F. Davidson, D. Harrison, and J. R. F. G. D. Carvalho, “On the Liquidlike Behavior of Fluidized Beds,” *Annu. Rev. Fluid Mech.*, vol. 9, no. 1, pp. 55–86, 1977, doi: 10.1146/annurev.fl.09.010177.000415.
- [75] H. Chenshu, K. Luo, S. Yang, S. Wang, and J. Fan, “A comprehensive numerical investigation on the hydrodynamics and erosion characteristics in A pressurized fluidized bed with dense immersed tube bundles,” *Chem. Eng. Sci.*, vol. 153, Jul. 2016, doi: 10.1016/j.ces.2016.07.023.
- [76] K. K. Dwivedi, S. Dutta, C. Loha, M. K. Karmakar, and P. K. Chatterjee, “A numerical study on the wall erosion impact and gas-particle hydrodynamics in circulating fluidized bed riser,” *Therm. Sci. Eng. Prog.*, vol. 22, p. 100852, May 2021, doi: 10.1016/j.tsep.2021.100852.
- [77] G. P. Tilly, “Erosion caused by airborne particles,” *Wear*, vol. 14, no. 1, pp. 63–79, Jul. 1969, doi: 10.1016/0043-1648(69)90035-0.
- [78] G. P. Tilly and W. Sage, “The interaction of particle and material behaviour in erosion processes,” *Wear*, vol. 16, no. 6, pp. 447–465, Dec. 1970, doi: 10.1016/0043-1648(70)90171-7.
- [79] W. S. Amarasinghe, C. K. Jayarathna, B. S. Ahangama, L.-A. Tokheim, and B. M. E. Moldestad, “Experimental Study and CFD Modelling of Minimum Fluidization Velocity for Geldart A, B and D Particles,” *152-156*, 2017, doi: 10.7763/IJMO.2017.V7.575.
- [80] X. Ku, T. Li, and T. Løvås, “Influence of drag force correlations on periodic fluidization behavior in Eulerian–Lagrangian simulation of a bubbling fluidized bed,” *Chem. Eng. Sci.*, vol. 95, pp. 94–106, May 2013, doi: 10.1016/j.ces.2013.03.038.
- [81] “Load Cells & Force Sensors,” <https://www.omega.com/en-us/>.
<https://www.omega.com/en-us/resources/load-cells> (accessed Mar. 04, 2022).
- [82] “The Working Principle of a Compression Load Cell,” *HBM*, Dec. 01, 2020.
<https://www.hbm.com/en/7325/the-working-principle-of-a-compression-load-cell/> (accessed Mar. 04, 2022).
- [83] Olympus Europa SE & Co. KG, “Getting the Right Tool for Every Application,” *IST Int. Surf. Technol.*, vol. 12, no. 3, pp. 42–44, Sep. 2019, doi: 10.1007/s35724-019-0060-z.
- [84] R. K. Thapa, A. Frohner, G. Tondl, C. Pfeifer, and B. M. Halvorsen, “Circulating fluidized bed combustion reactor: Computational Particle Fluid Dynamic model validation and gas feed position optimization,” *Comput. Chem. Eng.*, vol. 92, pp. 180–188, Sep. 2016, doi: 10.1016/j.compchemeng.2016.05.008.
- [85] T. L. Schroedter, “Conceptual Design of a Pilot-Scale Pressurized Coal-Feed System,” 2018.
- [86] L. Cai *et al.*, “Comparison of pressure drops through different bends in dense-phase pneumatic conveying system at high pressure,” *Exp. Therm. Fluid Sci.*, vol. 57, pp. 11–19, Sep. 2014, doi: 10.1016/j.expthermflusci.2014.03.016.
- [87] C. A. Brebbia, *Advances in Fluid Mechanics XI*. WIT Press, 2016.

References

- [88] A. C. Ma, K. C. Williams, J. M. Zhou, and M. G. Jones, “Numerical study on pressure prediction and its main influence factors in pneumatic conveyors,” *Chem. Eng. Sci.*, vol. 65, no. 23, pp. 6247–6258, 2010, doi: 10.1016/j.ces.2010.09.010.
- [89] D. Yang, Y. Wang, and Z. Hu, “Research on the Pressure Drop in Horizontal Pneumatic Conveying for Large Coal Particles,” *Processes*, vol. 8, no. 6, Art. no. 6, Jun. 2020, doi: 10.3390/pr8060650.
- [90] A. Levy and D. J. Mason, “The effect of a bend on the particle cross-section concentration and segregation in pneumatic conveying systems,” *Powder Technol.*, vol. 98, no. 2, pp. 95–103, Aug. 1998, doi: 10.1016/S0032-5910(97)03385-8.


<https://www.fhf.no/prosjekter/prosjektbasen/901658/>

Appendices

Appendix A

Pellet datasheet from the supplier

Approved 20.01.2019


 SKRETTING
 a Nutreco company

Protec 150, 300, 600, 1200 and 2500






Type of feed: Proactive health feed for salmon
 Place of production: Stavanger, Averøy, Stokmarknes
 Production method: Extruded
 Bag size: 500 and 750 kg


Description:
 Protec is a result of more than 20 years of research. The diet helps support skin, intestine and gills. Protec supports the immune system, adds building blocks for new cells and increases the level of antioxidants. Documentation shows that Protec supports fish in meeting with viruses, parasites and pathogenic bacteria. The feed can be added extra histidin to prevent cataract.

		Protec 150	Protec 300	Protec 600	Protec 1200	Protec 2500
Fish size	g	150 - 300	300 - 600	600 - 1200	1200 - 2500	2500 - 5000
Protein	%	44 - 47	42 - 45	40 - 43	35 - 38	33 - 25
Fat	%	25 - 28	27 - 30	29 - 32	31 - 34	33 - 36
NFE*	%	15 - 17	14 - 16	14 - 16	15 - 17	17 - 19
Fiber	%	0,6 - 4,5	0,6 - 4,5	0,6 - 4,5	0,6 - 4,5	0,6 - 4,5
Ash	%	5 - 6	5 - 6	5 - 6	5 - 6	5 - 6
Gross energy	MJ/kg	23,5 - 24,5	24 - 25	24,5 - 25,5	24,5 - 25,5	24,5 - 25,5
Pigment**	mg	50, 70	50, 70	50, 70	30, 50	30, 50
Pellet size	mm	4,5	4,5	7	9	9 and 12

*Nitrogen-free extracts ** Pigment source: Astaxanthin.

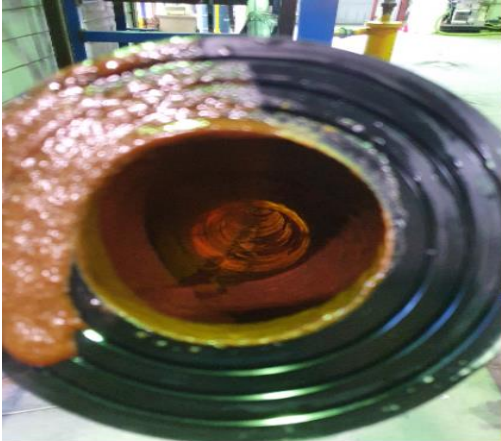
Raw materials
 Soy protein concentrate, rapeseed oil, fish oil, wheat gluten, wheat, fish meal, faba beans, camelina oil, sunflower meal.
 This document shows guiding values. The production certificate for each individual batch gives the accurate values.



Appendix B

Pictures from Erosion Tests



Internal view of the pipe after the erosion test



Internal view of the pipe straight section after the bend



Oily deposits from inside the bend section



Fresh pellets before erosion test



Broken pellets after erosion test

Appendix C

Experimental determination of bend radius

POINTS	RADIUS (cm)
1	162
2	167
3	173
4	174
5	167
6	163
Average	168

- ✓ Define Pipe external diameter and establish center points along the pipe bend
- ✓ Establish straight sections just before the bend (inlet) and immediately after the bend (outlet)
- ✓ Project this sections horizontally
- ✓ Establish reference point as intersection point between the projected lines
- ✓ Measure the distance from reference point to the initially established center points along the pipe bend.

Datasheet showing different bend radii at six locations along the pipe bend. A radius of 170cm was however used owing to measurement variations due to the nature of the pipe layout in the pilot rig.

Outlined Procedures carried out in the process of defining the bend radius in the pilot rig

Appendix D

Experimental determination of pellet diameter and height.

P/N	HEIGHT (cm)	DIAMETER (cm)	
1	1.00	0.94	1.00
2	0.97	0.90	1.00
3	0.97	0.90	1.00
4	0.93	0.99	1.10
5	0.99	0.93	1.00
6	1.00	0.99	1.00
7	1.00	0.92	1.10
8	0.92	0.94	1.00
9	0.91	0.90	1.10
10	1.00	1.00	1.00

P/N = Pellet number

- Diameter measured at two different sides of the pellet curvature.
- Measuring instrument ~ Vernier Caliper
- Average pellet diameter ~ 1cm
- Average pellet Height ~ 0.97cm

Appendix E

Determination of close-pack volume fraction

PROCEDURE

- 1) Volume of container was first found : Measured mass of water and density of water was used to get the volume.
- 2) Filling process for mass measurement in calculating loose bulk density
- 3) Taking readings
- 4) Tapping process (150 taps) and refilling for mass measurement used in calculating Tapered Bulk density.
- 5) Taking readings.
- 6) Repeating steps 1 to 5 for five different experiments.
- 7) Calculating average Bulk density.
- 8) Calculating Close pack volume fraction.

Outlined steps in defining close-pack volume fraction. Instruments used include; a measuring jug, a metal sieve, and a weighing scale.

E/N	Loose Poured (kg)	Tapped (kg)
1	0.823	0.877
2	0.824	0.877
3	0.823	0.876
4	0.822	0.877
5	0.823	0.876
Total	4.115	4.383
Average	0.823	0.877

➤ E/N = Experiment Number
 ➤ Volume of the container = 0.001253m³

A datasheet showing experimental values for loose and tapped mass of feed pellet.

Appendices

$$\theta_{CP} = \frac{\rho_{bulk}}{\rho_{particle}}$$

↓

0.56

where:

θ_{CP} is the particle close-pack volume fraction
 ρ_{bulk} is the bulk density
 $\rho_{particle}$ is the particle density

$$\text{Bulk density} = \frac{\text{Mass of the powder}}{\text{Bulk volume}}$$

↓

656.82kg/m³

$$\text{density} = \frac{\text{mass}}{\text{volume}}$$

↓

1176.5kg/m³

Envelop density/Particle density

Formulas used in calculating the close-pack volume fraction.

Appendix F

Signed copy of thesis description



Faculty of Technology, Natural Sciences and Maritime Sciences, Campus Porsgrunn

FMH606 Master's Thesis

Title: Development of a CPFDF model-based technique to optimize feed pellets transfer systems in fish farms

USN supervisor: Chandana Ratnayake

External partner: Chameera Jayarathna & Jana Chladek (SINTEF Tel-Tek)

Task background:

In aquaculture industry, the feeds, in form of granules or pellets, provide the nutrition in a stable and concentrated form, enabling the fish to feed efficiently and grow to their full potential. The fish feed pellets in the fish farms are typically transported pneumatically in HDPE pipes. To avoid blockage of the pipes, the fish farmers tend to use unnecessarily high transport air velocities. This has negative environmental and economic consequences: 1) pipe damage and more frequent repairs, 2) pipe wear causing emissions of microplastics into the sea, 3) pellet breakage leading to local pollution in seabed and loss of valuable and costly feed, and 4) high energy consumption.

SINTEF Tel-Tek has been conducting several R&D projects providing solutions for above challenges during last few years. The industrial collaboration projects show that there is a greater need for overall optimization of the pneumatic transport systems in fish farms and development of effective simulation tools. The providers of aquaculture equipment rely on physical tests which are resource demanding.

Task description:

The Master project is aimed to investigate the development of a CFD model-based technique (using Barracuda®) to optimize the pneumatic transport of fish feed in fish farms.

- a) Build a preliminary CPFDF model to describe the flow of fish feed through a HDPE pipe
- b) Compare the CPFDF model with experimental data of pilot tests
- c) Investigate possibilities of using the approach as a 'Digital Twin' of feed pellets transfer systems in the fish farms
- d) Possible publications

Student category: PT & EET students

Is the task suitable for online students (not present at the campus)? Yes/No



Practical arrangements:

The software licences are provided by USN. The experiments with pilot test rig, required training of using software and simulation methods will be assisted by SINTEF Tel-Tek.

Supervision:

As a general rule, the student is entitled to 15-20 hours of supervision. This includes necessary time for the supervisor to prepare for supervision meetings (reading material to be discussed, etc).

Signatures:

Supervisor (date and signature): 30.01.22  

Student (write clearly in all capitalized letters): OKORO IKECHUKWU JOHN

Student (date and signature): 28/01/2022 